DUCTILE FAILURE ANALYSIS DURING BACKWARD FLOW FORMING PROCESSES

A THESIS SUBMITTED TO
THE GRADUATE SCHOOL OF NATURAL AND APPLIED SCIENCES
OF
MIDDLE EAST TECHNICAL UNIVERSITY

BY

HANDE VURAL

IN PARTIAL FULFILLMENT OF THE REQUIREMENTS
FOR
THE DEGREE OF MASTER OF SCIENCE
IN
AEROSPACE ENGINEERING

AUGUST 2024

Approval of the thesis:

DUCTILE FAILURE ANALYSIS DURING BACKWARD FLOW FORMING PROCESSES

submitted by **HANDE VURAL** in partial fulfillment of the requirements for the degree of **Master of Science in Aerospace Engineering Department, Middle East Technical University** by,

Prof. Dr. Naci Emre Altun
Dean, Graduate School of **Natural and Applied Sciences** _____

Prof. Dr. Serkan Özgen
Head of Department, **Aerospace Engineering** _____

Assoc. Prof. Dr. Tuncay Yalçınkaya
Supervisor, **Aerospace Engineering, METU** _____

Examining Committee Members:

Assoc. Prof. Dr. Ercan Gürses
Aerospace Engineering, METU _____

Assoc. Prof. Dr. Tuncay Yalçınkaya
Aerospace Engineering, METU _____

Prof. Dr. Hüsnü Dal
Mechanical Engineering, METU _____

Assist. Prof. Dr. Görkem Eğemen Güloğlu
Aerospace Engineering, METU _____

Assist. Prof. Dr. Mehmet Okan Görtan
Mechanical Engineering, Hacettepe University _____

Date:05.08.2024

I hereby declare that all information in this document has been obtained and presented in accordance with academic rules and ethical conduct. I also declare that, as required by these rules and conduct, I have fully cited and referenced all material and results that are not original to this work.

Name, Surname: Hande Vural

Signature :

ABSTRACT

DUCTILE FAILURE ANALYSIS DURING BACKWARD FLOW FORMING PROCESSES

Vural, Hande
M.S., Department of Aerospace Engineering
Supervisor: Assoc. Prof. Dr. Tuncay Yalçınkaya

August 2024, 156 pages

Flow forming, also known as tube spinning, is an advanced metal forming process that produces thin-walled, high-precision cylindrical components. This process involves incrementally thinning the material using specially designed rollers and a mandrel, ensuring high dimensional accuracy and structural integrity. Due to the complex stress states and significant plastic deformation, accurate forming limit predictions are crucial to optimize the manufacturing process and avoid defects. This study aims to predict forming limits and fracture locations and assess the effects of process parameters on fracture in the flow forming process, focusing on IN718 and Al2024-O materials. The plastic behavior of these materials is modeled using von Mises and Bai-Wierzbicki yield functions with various hardening rules. The study evaluates single and multi-parameter uncoupled damage models in predicting fracture locations and formability limits, calibrated through tensile tests on specimens with different stress-state values. Tensile tests and flow forming processes are modeled with adiabatic heating and displacement-temperature coupled finite element simulations using ABAQUS/Explicit software, respectively. Subroutines such as VUHARD, VUMAT, and VUSDFLD are used to implement the models. The accuracy of each model

is assessed by comparing flow forming simulations with experimental trials at various thickness reduction ratios. Critical process parameters like feed rate, revolution speed, reduction ratio, and axial-radial offset are examined to evaluate their effects on failure. By combining experimental data with extensive numerical simulations, this research enhances the accurate prediction of ductile fracture in flow forming, potentially improving manufacturing practices in the automotive, aerospace, and defense industries.

Keywords: Ductile fracture, Flow forming process, Inconel 718, Al2024-O, Finite element method

ÖZ

GERİ YÖNLÜ AKITARAK SIVAMA SÜREÇLERİNDE SÜNEK KIRILMA ANALİZİ

Vural, Hande
Yüksek Lisans, Havacılık ve Uzay Mühendisliği Bölümü
Tez Yöneticisi: Doç. Dr. Tuncay Yalçınkaya

Ağustos 2024 , 156 sayfa

Akıtarak sıvama, aynı zamanda boru döndürme olarak da bilinen, ince duvarlı, yüksek hassasiyetli silindirik bileşenler üretmek için kullanılan gelişmiş bir metal şekillendirme işlemidir. Bu işlem, özel olarak tasarlanmış merdaneler ve bir mandrel kullanarak malzemeyi kademeli olarak inceltmeyi içerir ve yüksek boyutsal doğruluk ve yapısal bütünlük sağlar. Bu süreçte yer alan karmaşık gerilme durumları ve önemli plastik deformasyonlar nedeniyle, doğru şekillendirme sınırlarının tahmin edilmesi, üretim sürecini optimize etmek ve kusurlardan kaçınmak için kritik öneme sahiptir. Bu çalışma, IN718 ve Al2024-O malzemelerine odaklanarak, akıtarak sıvama sürecinde şekillendirme sınırlarını ve kırılma yerlerini tahmin etmeyi ve süreç parametrelerinin kırılma üzerindeki etkilerini değerlendirmeyi amaçlamaktadır. Bu malzemelerin plastik davranışı, çeşitli sertleşme kurallarıyla birlikte von Mises ve Bai-Wierzbicki akma fonksiyonları kullanılarak modellenmiştir. Çalışma, farklı stres durumu değerlerine sahip numuneler üzerinde yapılan çekme testleri ile kalibre edilen, kırılma yerlerini ve şekillendirme sınırlarını tahmin etmede tek ve çok parametreli bağımsız hasar modellerini değerlendirmektedir. Çekme testleri ve akıtarak sıvama süreçleri, sıra-

sıyla adyabatik ısıtma ve yer değiştirme-sıcaklık bağlı sonlu elemanlar simülasyonları kullanılarak ABAQUS/Explicit yazılımında modellenmiştir. Modellerin uygulanması için VUHARD, VUMAT ve VUSDFLD gibi alt programlar kullanılmıştır. Her modelin doğruluğu, çeşitli kalınlık azaltma oranlarındaki deneysel denemelerle karşılaştırılarak değerlendirilmiştir. Besleme hızı, devir hızı, azaltma oranı ve eksenel-radial offset gibi kritik süreç parametreleri, hasar üzerindeki etkilerini değerlendirmek için incelenmiştir. Yapılan deneysel verileri geniş kapsamlı sayısal simülasyonlarla birleştirerek, bu araştırma, akıtarak sıvamada sünek kırılma için daha doğru ve verimli tahmin etmede katkıda bulunmakta olup, otomotiv, havacılık ve savunma sanayilerinde üretim uygulamalarını iyileştirme potansiyeli sunmaktadır.

Anahtar Kelimeler: Sünek kırılma, Akıtarak sıvama süreci, Inconel 718, Al2024-O, Sonlu eleman yöntemi

To my family

ACKNOWLEDGMENTS

First and foremost, I extend my deepest gratitude to my supervisor, Assoc. Prof. Dr. Tuncay Yalçınkaya, for his exceptional guidance and support throughout my academic journey. His dedication to research and his motivational approach have been a constant source of inspiration. I am also grateful for the opportunities he provided during my master's program and before, in both academic and daily life.

I would like to express my sincere gratitude to Tevfik Ozan Fenercioğlu, Aptullah Karakaş, and REPKON Machine and Tool Industry and Trade Inc. for their experimental support and valuable insights. I am also grateful to Fırat Ergin for his help in the experiment of tensile tests.

I would also like to thank Can Erdoğan and the other members of Dr. Yalçınkaya's research group for their valuable contributions. Special thanks to İlkay Kölay for her enduring friendship. It has been a joy and privilege to share this journey with her from the first day of university to the completion of this thesis.

My sincere appreciation goes to my parents, Selma Vural and Cafer Vural, and my brother Hasan Vural, for their endless love and support. Their kindness is beyond measure, and words cannot adequately express my gratitude. This work is dedicated to them with my deepest thanks for everything they have done.

Lastly, I gratefully acknowledge the support of the Scientific and Technological Research Council of Turkey (TÜBİTAK) under the 2210-A program.

TABLE OF CONTENTS

LIST OF TABLES

TABLES

LIST OF FIGURES

FIGURES

CHAPTER 1

INTRODUCTION

Metal forming is a critical production process that involves shaping bulk or sheet metal parts into desired geometries through various techniques, increasing their mechanical properties and dimensional accuracy. Among these techniques, spinning stands out due to its ability to produce axisymmetric components. There are three types: conventional spinning, shear spinning and flow forming. The common feature of all of them is that one or more rollers shape the metal in one or several steps with the help of a mandrel fixing the part [1, 2].

Flow forming, or tube spinning, is an incremental metal forming technique in which axisymmetric tube-shaped parts are produced [3, 4, 5]. The tube-shaped preform is prepared using various techniques, such as deep drawing or forging, and heat treatment can be applied to the preform to relieve stress and control the microstructure before shaping. This advanced forming technique involves placing the cylindrical part on a mandrel and applying continuous, local plastic deformation through one or more rollers moving axially and radially [6]. During this process, the material flows along the mandrel with plastic deformation, causing the wall thickness to decrease and the length to increase [7].

This process is called "backward" or "forward" flow forming, depending on whether the roller movement differs from the material flow direction. In both modes, as shown in Figure 1.1, the length of the tube is increased and its thickness is reduced, but the material flow directions are different depending on the roller movement. In forward flow forming, the roller movement and material flow are in the same direction, and the workpiece remains fixed at the tailstock. However, in backward flow forming, the roller moves against the material flow, and the workpiece is fixed at the headstock.

In addition, forward flow forming offers higher dimensional accuracy as it provides continuous contact with the mandrel but requires a long mandrel and machine and poses a risk of cracks in low-ductility materials. Backward flow forming provides high reduction and speed advantages but has lower dimensional accuracy due to the material losing contact with the mandrel.

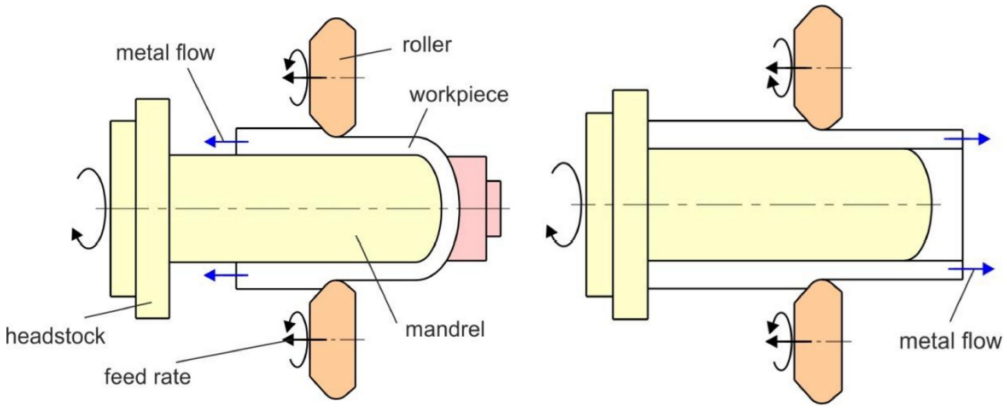

Figure 1.1: Flow forming types: (a) forward, (b) backward [8]

This advanced metal forming method produces lightweight, high-performance parts in the automotive, defense, and aerospace industries [9]. It has a high production capacity, especially in axially symmetric metal parts such as wheels, shafts, rocket bodies and launch tubes. The process can work on a wide range of materials, enabling the production of parts from aluminum, steel, nickel-based steels, titanium, and their alloys. For certain alloys, the thickness of the preform can be reduced by 70-80%, resulting in high localized deformation. Materials that are difficult to cut and shape can be formed with this technique. Moreover, formed parts possess improved mechanical properties such as yield stress and tensile strength and changes in microstructure as discussed in [10, 11, 3]. The formable dimensions of the tubes are extensive. The diameter of the tubes is from 25 mm to 3 m, and its length can reach up to 3 m [12]. The process provides precise wall thickness control with high geometric accuracy, so components with excellent surface quality can be produced without additional surface finishing [13]. Due to the incremental nature of the process and the local forces applied by the rollers, forming loads are low, reducing machine costs and energy con-

sumption [6]. These features make flow forming a cost-effective and efficient process to produce high-quality components with excellent precision and structural integrity.

During the flow-forming process, the material with reduced thickness undergoes high plastic deformations. With the local forces of the rollers, the preform is subjected to highly localized and complex stress states. These conditions lead to undesirable cracks in the workpiece being thinned to a specific thickness. These cracks in tube forming of metals can appear even at small thickness reductions and disappear at moderate thinning ratios, indicating the complexity of the forging process and that the exact formability limit of materials is unclear [14]. Various defects are commonly observed during pipe forming. These defects mainly arise from the interaction between the material and the rollers. During forming, material accumulation ahead of the roller occurs on the outer surface of the tube, increasing throughout the process. This accumulation lifts the tube from the mandrel in front of the roller, creating a wave. In backward tube forming, bell-mouth defects appear at the free end of the tube, while flaring, seen during forward tube forming, represents the final stage of material accumulation and axial swelling. Circumferential bulging, which causes the tube's diameter to increase and become oval, occurs behind the roller. Fish-scaling results from the folding of material accumulated in front of the roller and roller markings are left on the tube's outer surface by the roller. Along with these defects caused by plastic flow instability, ductile failures such as tube wall fracture, inner surface cracks, outer surface cracks, and microcracks can also be observed when forming limits are exceeded [15, 16]. Additionally, tube wall fracture occurs at high reduction rates, and inner surface cracks occur due to uneven deformation across the thickness. Outer surface cracks are typically due to defects in the tube material, and microcracks similarly arise from imperfections within the material.

Defects that can occur during the process significantly affect the final product's quality [17, 18]. For example, excessive deformation in the process can accumulate undesiring internal stresses and microcracks in the material. Ductile fracture is one of the primary defects in this process, and studies show that changes influence it in the stress state. Predicting ductile fracture in a part subjected to multiaxial and complex loading is not straightforward. In this context, understanding ductile fracture mechanisms is crucial for optimizing material selection and process parameters. However,

understanding these mechanisms through experimental testing may be quite costly. Therefore, predicting forming limits and preventing defects through computational approaches to reduce experimental costs is interesting. At this point, finite element (FE) methods come into play. As noted by Music et al. [2], the FE method is widely used to understand better forming loads and material behavior, and numerical simulations combined with ductile fracture can be employed to predict damage and fracture in metal forming.

Ductile fracture is the failure of materials under large plastic deformation. This phenomenon is a critical study area in various industries, such as automotive and aerospace. Such failures can be explained by two different mechanisms: void coalescence or plastic instability. The first mechanism involves the nucleation, growth, and coalescence of microvoids [19, 20, 21]. This mechanism has explained different failure examples at different length scales [22, 23, 24, 25, 26]. In the other mechanism, plastic instability causes the formation of one or more shear bands, leading to material fracture along the shear band (see Figure 1.2).

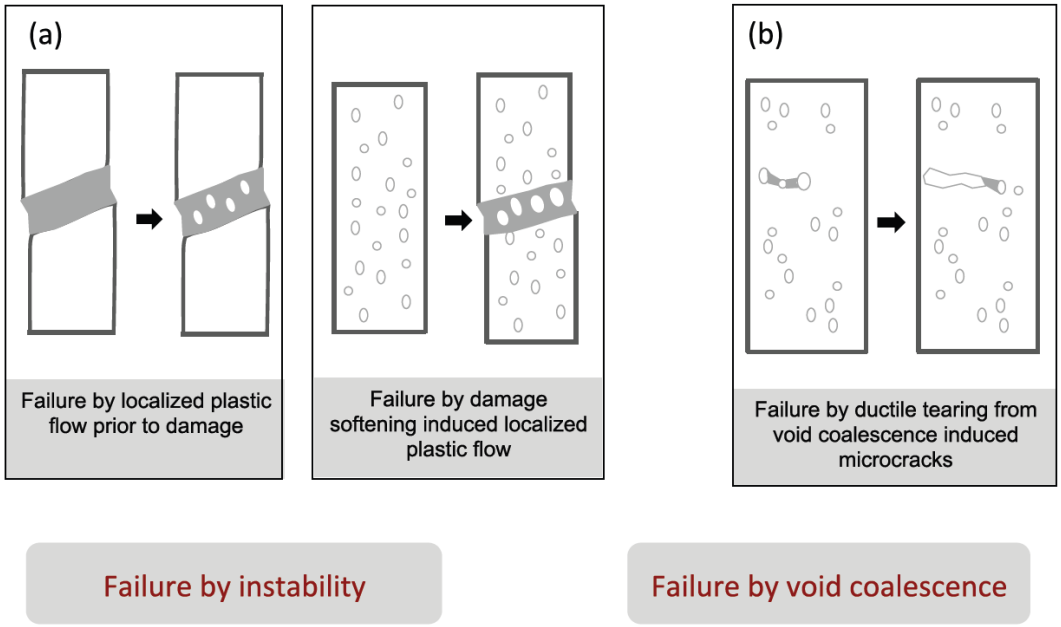

Figure 1.2: The two mechanisms of ductile fracture: plastic instability and void coalescence, respectively. [27]

Measurement and prediction of ductile fracture is quite complex and requires the for-

mulation of the state from initiation to failure. Factors such as stress-strain state and loading history affect this situation. In this context, dimensionless stress parameters such as stress triaxiality and Lode parameter are critical. Stress triaxiality, which is the ratio of mean stress to the von Mises equivalent stress, plays a crucial role in ductile fracture [28, 29, 30, 21, 31]. In the case of high triaxiality, voids tend to grow and coalesce rapidly. In contrast, low triaxiality can lead to shear band formation, which can cause fracture by different mechanisms. The fracture mechanisms associated with varying stress triaxiality are illustrated for a representative ductile fracture locus in Figure 1.3. The x-axis represents stress triaxiality in this figure, while the y-axis shows the failure strain. Using this graph, specific ductile failure models can be used to predict damage under different loading conditions. Studies have shown that the Lode parameter, which is associated with the third invariant of the deviatoric stress tensor, can make different fracture predictions even at the same stress triaxiality value [32, 33, 34].

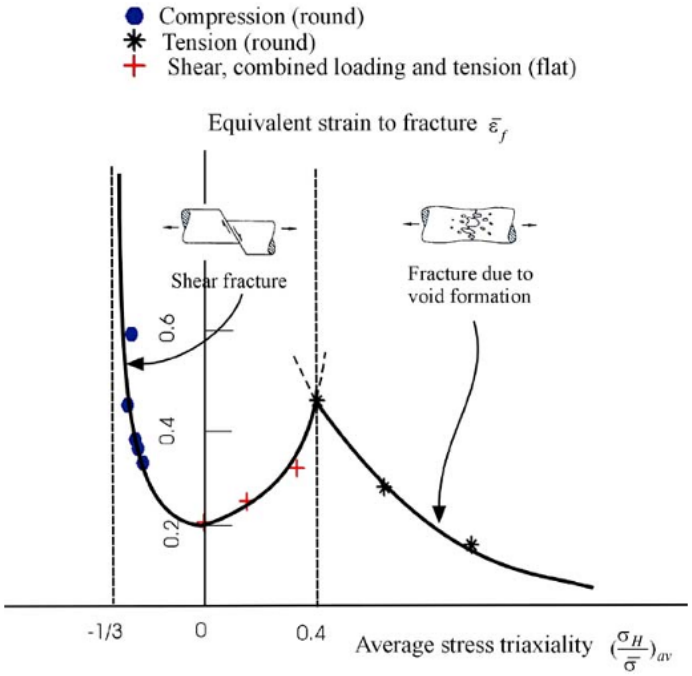

Figure 1.3: Equivalent strain to fracture versus average stress triaxiality, illustrating different fracture modes under various loading conditions: compression, tension, and shear. [35]

Various ductile fracture criteria have been developed through experimental and nu-

merical studies (e.g. [32, 31, 36, 37, 38]). These criteria can be classified under uncoupled and coupled damage models. In uncoupled models, plasticity analysis is unaffected by damage changes in the material and plasticity and damage are calculated independently. The damage is evaluated with an empirical fracture criterion, and when this criterion reaches the critical value, the failure occurs. These criteria generally depend on plastic strain, stress state, temperature, and strain rate (e.g. [39, 40]). Cockcroft-Latham (CL, [39]) and OH [41] models are widely used in industrial applications due to their simplicity and ease of calibration for fracture estimation. It has only one parameter that needs to be calibrated, but the effect of the Lode parameter is not included. Johnson-Cook (JC, [40]) criterion, like single-parameter models, includes only the stress triaxiality effect, with temperature and strain effects. Recently, the Modified Mohr-Coulomb (MMC, [32]), the Hosford-Coulomb model (HC, [42]), and the DF2012 [43], DF2014 [44], DF2015 [45] proposed by Lou et al. are examples of models that include both triaxiality and the Lode parameter. Since they have more than one damage parameter (multi-parameter), the calibration process is more complex than models with single-parameter models. Various experimental comparisons are made with empirical models to compare their fracture prediction abilities [35, 46, 47, 48]. In addition, McClintock [20] and Rice-Tracey (RT, [21]) were among the first to model these micromechanics-based approaches, taking into account void formation, growth and coalescence. This group can also include these two models, as they do not incorporate constitutive relations.

Coupled models involve the interaction of plasticity analysis with changes in material damage. In these models, damage evolution is included in the constitutive equations, causing the material to soften as damage accumulates. Compared to uncoupled models, FE implementation is more challenging. Models based on continuum damage mechanics (CDM) and micromechanics are examined within this group. CDM, or phenomenological models, describe damage evolution from a macroscopic perspective within a thermodynamic framework. These models, initially developed by Chaboche [49] and Lemaitre [50], offer a more comprehensive approach to capture the gradual degradation of mechanical properties but require calibration of multiple material parameters and simultaneous calibration of plasticity and damage, making their implementation more complex. Another class of coupled ductile failure models

is based on micromechanically motivated frameworks (e.g. [51, 52, 53]) where the damage evolution is governed through void nucleation, growth and coalescence relations. Gurson [51] systematically discussed the relationship between void growth and material behavior by formulating a damage model that associates the void volume effect (porosity) with the yield function. In addition, micro-void is represented using a representative volume element (RVE), and void and coalescence effects are included in the Gurson-Tvergaard-Needleman (GTN, [52]) model. These models provide detailed information about fracture mechanisms and predict ductile fracture under various stress states with high accuracy. However, micromechanical tests are needed for calibration. The complexity and computational cost of the models limit their widespread use in practical engineering applications.

Ductile fracture criteria (DFC) or forming limit diagram (FLD) in combination with FE are commonly used in the literature to predict formability. FLDs are derived from the plastic limit based on the onset of necking of the material under different stress states, and they have been successfully used to capture failure mostly for sheet metals subject to drawing [54, 55, 56]. However, it is not very successful in predicting flow forming and cannot reasonably predict ductile fracture [57, 58, 59]. Compared to traditional FLDs, FE analyses with DFCs can predict fractures occurring under complex strain and stress histories. DFCs have been used in various applications, from ballistic impacts [60, 61] to metal forming [62, 63, 64]. Previous studies on flow-formed tubes have generally focused on plastic flow instability as the failure mode [65, 66]. Although the use of DFCs for predicting ductile failure in this process is still limited, it is increasingly being used to predict fracture.

Various studies have widely used the rather practical uncoupled criteria to predict ductile fracture in the flow forming process. Basic models usually include one parameter to be calibrated, and several of them are studied comparatively in [67, 68, 69] in the context of tube spinnability, and CL and McClintock criteria are found to be the most accurate compared to experimental data. The advantage of these models is that the parameter calibration can be done using a single tensile or compressive failure test. In addition to these studies, the [70] study, which predicted fractures during the production of thick-walled pipes made of Inconel 718, takes into account cyclic loading and utilizes the Kolmogorov criterion [71] to estimate fracture loca-

tions. However, the study demonstrates that the former needs to be improved for accurately predicting fracture among the two deformation models used, rigid-plastic flow rule and elastic-plastic. Zhan et al. [72] used the modified Oyane model to predict fractures by incorporating the effect of temperature and strain rate into the damage model for titanium alloy, highlighting the effects of temperature on damage initiation and propagation. Mocellin et al. [73] analyze the effects of parameters such as reduction ratio and number of passes on the backward flow forming of AA6061-T6 aluminum alloy using CL, Oyane, and DF2013 criteria and say that although the models can not make a good prediction, the CL criterion is the most accurate model. Since ductile failure is affected by stress states [35, 74, 75], various damage models have also been studied, including stress triaxiality and Lode angle parameter. Damage estimation in flow forming is tried to be made for materials such as T6 temper of Al6016 aluminum alloy [62] and AISI 4340 steel in HRC 16 hardness condition [63] using the MMC damage model adapted from the literature and the effects of various process parameters are examined. Parameter identification for JC and MMC models usually requires experiments with several geometries to cover various stress triaxiality and Lode parameter values (e.g.[74, 76]). For this reason, tensile tests are carried out for IN718 in various geometries, and the fracture prediction capacities of these models and the CL damage model are compared in [77, 78].

Coupled models, which are more complex in their implementation and application, have recently been used to predict fractures in the flow forming process. Ductile fracture frameworks motivated solely by the micro-void nucleation and growth are insufficient for forming applications since the material fails due to shear fractures that cannot be captured with these models, as discussed in [68]. In the study to evaluate the applicability of the GTN model, ductile fracture is predicted under various conditions using the GTN model, and parameters such as void volume fraction, stress triaxiality, and strain rates are compared with experimental data to assess the accuracy of models [79]. In the backward spinning study of Ti-15-3 alloy, ductile fracture is predicted using the GTN model, and parameters such as maximum void damage and critical value of void coalescence are compared with experimental results. However, they are insufficient for forming applications [80]. In addition, in a three-dimensional finite element analysis study on this process of 2024 aluminum alloy, damage evo-

lution, and cracking mechanisms are analyzed using the modified GTN model, and the model's accuracy is verified by comparing it with experimental results [81]. In the flow forming study of titanium alloy, a shear-modified continuous damage model (CDM) is used to understand the effects of different roller arrangements on formability [82]. Another coupled ductile failure framework is based on the continuum damage approach proposed in [50]. It has been applied to determine forming limits and study the effect of process parameters for splitting spinning [83] and flow forming [84]. In [84], triple and single roller arrangements and the effect of feed rate on failure are investigated with FE analysis. The incremental increase in damage in these frameworks is calibrated based on the reduction of elastic modulus over a repetitive loading-unloading cycle in tensile tests. Zhan et al. ([85]) compare the CL and Lemaitre models and find that Lemaître predicted the crack fracture position more successfully.

Despite all these advances in numerical models, a comprehensive study is needed to predict the forming limits and optimize the process parameters in the flow forming process. As noted in the [69, 86] studies, ductile fracture models calibrated by tensile or compression tests cannot accurately predict forming limits in applications with complex loading histories, such as shear spinning and flow forming. Additionally, finite element analyses and fracture models in the literature generally do not consider the temperature changes that occur during the forming process. As highlighted by [4], it has been argued that although flow forming is a cold forming process, thermal softening should not be ignored.

This study aims to predict the forming limits and fracture locations in the flow forming process and to optimize the process parameters. Tensile tests and flow forming processes are numerically modeled in ABAQUS/Explicit software with displacement-temperature coupled FE simulations. Various subroutines are used in the study: VUHARD for the implementation of hardening rules; VUMAT for the application of von Mises and Bai-Wierzbicki yield functions; and VUSDFLD for integrating fracture models into the FE framework. The plasticity and damage models are calibrated using tensile test data and then applied to the flow forming process to evaluate their predictive capabilities.

In this research, the flow forming process of IN718 material is examined through experimental and numerical methods, while the analysis of Al2024-O is conducted through numerical simulations. For IN718, cylindrical tubes are tested at various thickness reduction ratios using a three-roll flow forming machine, and these results are compared with computational predictions. In contrast, due to the lack of comparable experimental results for Al2024-O, only the effects of yield function are investigated by finite element (FE) simulations of flow forming. The stress and strain distributions for Al2024-O are numerically compared through flow forming analyses conducted at different reduction ratios.

This study applies various uncoupled single and multiple-parameter damage models from the literature within the FE framework to predict forming limits and fracture locations. Tensile tests are conducted on various geometries with different stress triaxiality and Lode parameter values to calibrate the plasticity and fracture criteria of the two materials. These tests are carried out to obtain experimental force-displacement curves with the Digital Image Correlation (DIC) method using four different specimen geometries. The collected data are then used to model the plasticity of the materials. For IN718, the extended Voce rule and von Mises yield function are employed, while for Al2024-O, the Bai-Wierzbicki yield function, incorporating stress triaxiality and Lode parameters, is used due to its complex plastic behavior. The BW yield function is implemented in the VUMAT subroutine and validated with literature data.

Following the plasticity modeling, the parameter identification for single and multiple-parameter uncoupled damage models is conducted for the calibrated materials. Multiple parameter models account for the effects of stress triaxiality and Lode parameters but require several parameters to be calibrated using various geometric tests. Single-parameter models can be calibrated with a single test. Both groups of models are implemented in the VUSDLFD subroutine. These calibrated models are applied in the flow forming process. First, the damage models' fracture prediction abilities are compared using experimental flow forming trials. The effects of various process parameters, including feed rate, revolution speed, thickness reduction ratio, and roller offsets, on forming limits are examined using the compared models. The effects of these parameters have been analyzed extensively, with a particular focus on their ef-

fects on plastic strain and damage.

The results indicated that the material reached high strain values due to complex loading conditions. The strain value obtained from tensile tests is relatively low and limited compared to the strain occurring in the process. Therefore, the plastic behavior beyond the strain value obtained experimentally must be modeled using various hardening rules. Various hardening rules and combinations have been studied to model plasticity accurately at higher strain values. The effects of these rules on tensile tests and flow forming at various stress states are examined.

The organization of the thesis is as follows. In Chapter 2, the characterization of stress states, as well as the formulation and numerical implementation of plastic and damage models, will be discussed. In Chapter 3, focusing on the introduction of the materials used in the thesis, tensile tests, identification and verification of plastic and damage models, experimental data of tensile tests, and finite element modeling results will be presented. In Chapter 4, process parameters and their effects on formability are emphasized, covering flow forming experiments and finite element modeling. Section 5 discusses the results obtained by analyzing the effects of process parameters on the formability of IN718 and the plasticity effects of these two materials. Finally, Chapter 6 concludes the thesis with a summary of findings, contributions to the field, and potential future research.

CHAPTER 2

FORMULATION AND NUMERICAL IMPLEMENTATION OF PLASTICITY AND DAMAGE MODELS

This chapter presents the theoretical foundations and numerical applications of the plasticity and damage models used in the study to understand and predict the plasticity and fracture behavior of materials. The formulation of the models involves characterizing the stress state and employing invariants of stress tensor to describe material responses accurately. Familiar concepts and definitions widely used in plasticity theory are addressed within the discussion. Subsequently, the formulation of both plasticity and damage models is presented, utilizing isotropic hardening rules and employing two different yield functions: the Von Mises (VM) yield function and the Bai-Wierbicki (BW, [87]) yield function. Various phenomenological damage models are also discussed in this context. The chapter then moves on to the numerical implementation of these models, emphasizing the computational methods and algorithms employed to integrate them into finite element analysis.

2.1 Characterization of Stress State

Characterizing the stress state is fundamental to understanding and modeling material behavior under various loading conditions. Stress space is a multi-dimensional representation where each point corresponds to a unique state of stress within a material. This section explores the fundamental concepts of stress state, including the definition and significance of stress tensors, stress invariants, and principal stresses. The representation of stress invariants, in particular, allows for a simplified yet comprehensive description of the complex stress states encountered in engineering applications. This

foundational understanding is crucial for formulating and numerically implementing the models discussed in subsequent sections.

2.1.1 Stress States and Stress Tensors

The stress state at a point within a material is of two types, normal and shear stress, and is represented by the stress tensor $\boldsymbol{\sigma}$, which is a second-order symmetric tensor. This tensor is formulated as follows:

$$\boldsymbol{\sigma} = \begin{bmatrix} \sigma_{11} & \sigma_{12} & \sigma_{13} \\ \sigma_{12} & \sigma_{22} & \sigma_{23} \\ \sigma_{13} & \sigma_{23} & \sigma_{33} \end{bmatrix} \tag{2.1}$$

The stress tensor can be separated into the volumetric (hydrostatic) stress tensor and the deviatoric stress tensor. The volumetric stress tensor can be defined by the trace of stress tensor ($tr(\boldsymbol{\sigma})$), which is the sum of normal stresses or the sum of the principle stresses (σ_1, σ_2 and σ_3). The formula for σ_m, expressed as average stress, is as follows:

$$\sigma_m = \frac{1}{3} tr(\boldsymbol{\sigma}) = \frac{\sigma_1 + \sigma_2 + \sigma_3}{3} \tag{2.2}$$

The deviatoric stress tensor, $\boldsymbol{\sigma'}$, represents the distortional component of the stress tensor. In other words, it describes the change in the shape of the material. It is obtained by subtracting the volumetric stress tensor from the total stress tensor:

$$\boldsymbol{\sigma'} = \boldsymbol{\sigma} - \sigma_m \boldsymbol{I} = \boldsymbol{\sigma} - \frac{1}{3} tr(\boldsymbol{\sigma}) \boldsymbol{I} \tag{2.3}$$

where $\boldsymbol{I}$ is the identity matrix.

Essentially, while the volumetric stress tensor accounts for a material's uniform expansion or compression, the deviatoric stress tensor accounts for the distortional changes. Many yield criteria and damage theories are based on the deviatoric stress tensor, making it crucial to understand how materials flow and deform under different loading conditions. The principal stresses of the deviatoric stress tensor, often denoted as ${\sigma'}_1$, ${\sigma'}_2$, and ${\sigma'}_3$, can be found similarly to the principal stresses of the original stress tensor, by solving the characteristic equation of the deviatoric stress tensor.

2.1.2 Stress Invariants

Stress invariants are scalar quantities derived from the stress tensor that remain unchanged under coordinate transformations. They, crucial in characterizing the stress state, are represented mathematically. They are extensively used in yield criteria and failure theories. The first invariant I_1, which represents the sum of the normal stresses, is the trace of the stress tensor. It is worth noting that the first invariant of the deviatoric stress tensor, J_1, is always zero. This is because the deviatoric stress tensor is derived by subtracting the mean stress, thereby removing any volumetric component. I_1 can be expressed as:

$$I_1 = \sigma_1 + \sigma_2 + \sigma_3 \tag{2.4}$$

The second invariant, I_2, is related to the sum of the products of the principal stresses taken two at a time and provides information about the deviatoric stress. In the context of the deviatoric stress tensor, this invariant is often referred to as $J2$ and is defined as:

$$J_2 = \frac{1}{2} tr(\boldsymbol{\sigma}'^2) = \frac{1}{6}\left[(\sigma_1 - \sigma_2)^2 + (\sigma_2 - \sigma_3)^2 + (\sigma_3 - \sigma_1)^2\right] \tag{2.5}$$

The third invariant, I_3, represents the determinant of the stress tensor, representing the product of the principal stresses and indicating how the material behaves under multi-axial stress conditions. For the deviatoric stress tensor, the third invariant is denoted as J_3 and is given by:

$$J_3 = det\,(\boldsymbol{\sigma'}) = \sigma'_1\sigma'_2\sigma'_3 \tag{2.6}$$

2.1.3 Stress Triaxiality and Lode Parameter

The stress state of an isotropic material can be characterized by its principal stresses. Alternatively, it can also be described geometrically within the Haigh–Westergaard stress space, which utilizes cylindrical coordinates (μ, ρ, and θ) as depicted in Figure 2.1. These coordinates can be expressed in terms of stress invariants as follows:

$$\begin{aligned} \mu &= |OO'| = \frac{1}{\sqrt{3}} I_1 \\ \rho &= |O'P| = \sqrt{2J_2} \\ cos(3\theta) &= \frac{27}{2}\frac{J_3}{\sigma_{eq}^3} \end{aligned} \tag{2.7}$$

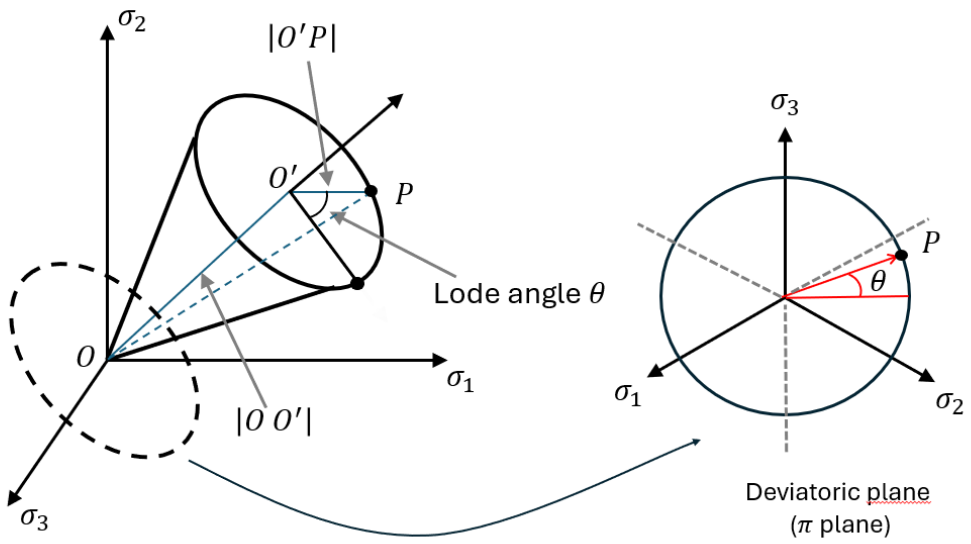

Figure 2.1: Illustration of the stress state in the deviatoric plane (π plane), showing the relationship between the principal stresses (σ_1, σ_2 and σ_3), the Lode angle (θ), and the deviatoric stress components.

In the literature, two basic parameters affect ductility: stress triaxiality [88, 89, 90, 91] and Lode parameters [92, 93, 94]. The stress state can be characterized with these two dimensionless parameters and is used to understand material behavior under complex loading conditions. The ratio of hydrostatic stress σ_m to the equivalent von Mises stress (σ_{eq}) is called stress triaxiality (η) and indicates the degree of tensile or compression loads acting on the material. Since it is associated with void formation and coalescence, it provides information about the ductile fracture behavior of materials. Stress triaxiality is expressed as:

$$\eta = \frac{\sigma_m}{\sigma_{eq}} = \frac{\sqrt{2}\mu}{3\rho} \tag{2.8}$$

The von Mises equivalent stress (σ_{eq}) in the stress triaxiality formula is expressed with stress invariant and principle stresses as follows:

$$q = \sigma_{eq} = \sqrt{3J_2} = \sqrt{\frac{1}{2}\left[(\sigma_1 - \sigma_2)^2 + (\sigma_2 - \sigma_3)^2 + (\sigma_3 - \sigma_1)^2\right]} \tag{2.9}$$

For uniaxial tension, the stress triaxiality η is 0.33, indicating a moderate level of tensile stress concentration. In equi-biaxial tension, η increases to 0.66, reflecting a higher stress concentration due to the biaxial nature of the loading. The stress triaxiality η is 0 for simple shear, signifying no volumetric change. In uniaxial compression,

η is -0.33, denoting a moderate compressive stress concentration.

The Lode angle parameter, on the other hand, characterizes the deviatoric stress state by describing the relative magnitudes of the principal stresses. This parameter is essential for distinguishing between different types of shear stress states and influences the yield and flow behavior of materials. By examining the Lode angle in conjunction with stress triaxiality, a more comprehensive understanding of material response under multiaxial loading conditions can be achieved. Various Lode dependency terms are available in the literature. These include the normalized third invariant of the deviatoric stress tensor (ξ), the Lode angle (θ), the Lode parameter (L), and the normalized Lode angle ($\bar{\theta}$).

The first of the Lode dependency terms is the normalized third invariant of the deviatoric stress tensor. This term, shown as ξ, is related to the Lode angle shown on the deviatoric plane in Figure 2.1. It is defined as:

$$\xi = \frac{27}{2}\frac{J_3}{\sigma_{eq}^3} = cos(3\theta) \tag{2.10}$$

The $\frac{27}{2}$ is included in the normalization to ensure that its range is $-1 \leq \xi \leq 1$.

The Lode angle, θ, quantifies the relative magnitudes of the principal stresses and offers insights into the stress state within the deviatoric plane. It is typically defined as $0 \leq \theta \leq \frac{\pi}{3}$. The Lode angle is beneficial for distinguishing between different types of shear stress states. The Lode angle (θ) can be calculated using the normalized third invariant of the deviatoric stress tensor (ξ) as follows:

$$\theta = \frac{1}{3}cos^{-1}\xi \tag{2.11}$$

The Lode parameter (L) is a dimensionless quantity that characterizes the deviatoric stress state, providing insight into the relative magnitudes of the principal stresses. It is particularly useful in distinguishing between shear stress states and predicting material behavior under complex loading conditions. The Lode parameter can be formulated by the normal stress in the maximum shear plane (σ_N) and the maximum shear stress (τ).

$$L = \frac{\sigma_2 - \sigma_N}{\tau} \tag{2.12}$$

where σ_N and τ are defined as:

$$\begin{aligned} \sigma_N &= \frac{\sigma_1 + \sigma_3}{2} \\ \tau &= \frac{\sigma_1 - \sigma_3}{2} \end{aligned} \tag{2.13}$$

where σ_1, σ_2 and σ_3 are the principle stresses from maximum to minimum. Combining these expressions, the Lode parameter, which ranges from -1 to 1, can also be defined as:

$$L = \frac{2\sigma_2 - \sigma_1 - \sigma_3}{\sigma_1 - \sigma_3} \tag{2.14}$$

The normalized Lode angle ($\bar{\theta}$), often known as the Lode angle parameter, is widely utilized in stress analysis. This term is particularly useful in describing the effect of the third invariant of the deviatoric stress tensor (J_3) on the stress state. Mathematically, the normalized Lode angle ($\bar{\theta}$) can be expressed by the Lode angle (θ) and the normalized third invariant of the deviatoric stress tensor(ξ). It varies between -1 and 1 and can be represented as:

$$\bar{\theta} = 1 - \frac{6\theta}{\pi} = 1 - \frac{2}{\pi} cos^{-1}\xi \tag{2.15}$$

In plasticity and damage models, the principal stresses (σ_1, σ_2 and σ_3) can also be calculated using the Lode angle or Lode angle parameter. These equations are included in the plasticity and damage models discussed in this thesis and will be used in subsequent sections. The principal stresses are obtained using the following equations, which are dependent on the Lode angle parameter:

$$\begin{aligned} \sigma_1 &= \sigma_{eq}\left[\eta + f_1\left(\bar{\theta}\right)\right] \\ \sigma_2 &= \sigma_{eq}\left[\eta + f_{II}\left(\bar{\theta}\right)\right] \\ \sigma_3 &= \sigma_{eq}\left[\eta + f_{III}\left(\bar{\theta}\right)\right] \end{aligned} \tag{2.16}$$

where $f_I\left(\bar{\theta}\right)$, $f_{II}\left(\bar{\theta}\right)$ and $f_{III}\left(\bar{\theta}\right)$ are deviator-dependent functions defined as:

$$\begin{aligned} f_I\left(\bar{\theta}\right) &= \frac{2}{3} cos\left(\frac{\pi}{6}\left(1 - \bar{\theta}\right)\right) \\ f_{II}\left(\bar{\theta}\right) &= \frac{2}{3} cos\left(\frac{\pi}{6}\left(3 - \bar{\theta}\right)\right) \\ f_{III}\left(\bar{\theta}\right) &= -\frac{2}{3} cos\left(\frac{\pi}{6}\left(1 + \bar{\theta}\right)\right) \end{aligned} \tag{2.17}$$

2.2 Formulation and Implementation of Plasticity Models

Plasticity describes the capacity of solid materials to experience permanent deformation under external forces. Materials undergo deformations in which shape and size change under the influence of these conditions. This deformation is elastic if the material returns to its original state when external loads are removed. Plastic deformation occurs when the material exceeds its elastic limit and forms irreversible shape changes when the stress is removed. Plastic deformation usually occurs due to the movement of dislocations within the crystal lattice and can occur as crystal slip [95]. It occurs when dislocations move along certain planes in the crystal structure.

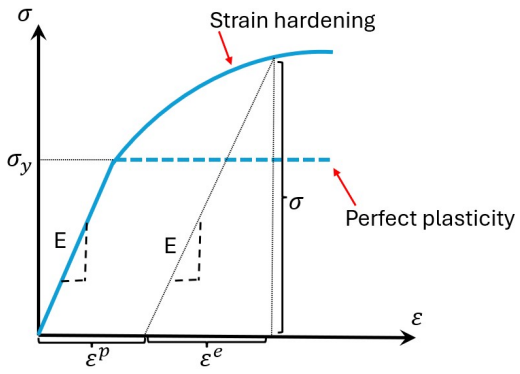

Figure 2.2: Elastic-plastic strain decomposition with strain hardening and perfect plasticity.

The strain-strain behavior under tensile loading can be represented as shown in Figure 2.2. The total strain can be divided into elastic and plastic strain, with the transition between these two regions known as yielding. The classical additive decomposition of strain is formulated as follows:

$$\varepsilon = \varepsilon^e + \varepsilon^p \tag{2.18}$$

The stress-strain relation is formulated using these strain expressions as follows:

$$\sigma = E\varepsilon^e = E(\varepsilon - \varepsilon^p) \tag{2.19}$$

where E is Young's modulus, shown in Figure 2.2.

The point that indicates the limit of elastic behavior and the onset of plastic behavior in materials is called yield stress (σ_y). In a material that has yielded, the stress remains

constant at the yield stress level as strain increases during plastic deformation. This condition is known as perfect plasticity in a material that does not undergo hardening. However, if the stress increases along with strain after the yield point, the material is considered to have undergone strain hardening.

Accurate modeling of plasticity and damage in materials is crucial for predicting their behavior under various loading conditions. Plasticity is defined by flow theory, which includes the yield criterion, flow rule and hardening law. While the yield criterion specifies the stress state at which yielding begins, the flow rule describes how plastic strain will increase following yielding. Additionally, the hardening law characterizes the variation in flow stress as plastic deformation progresses. This section focuses on the formulations of yield functions and isotropic hardening rules, as well as their FE element implementations. In this study, different hardening criteria along with Von Mises (VM) and Bai-Wierzbicki (BW) yield functions are used and integrated into the ABAQUS/Explicit.

2.2.1 Yield Criterion and Flow Rule

Various yield surface models are employed to describe the flow behavior of materials, defining the onset of plastic deformation. As shown in Figure 2.3, the material exhibits elastic properties within the yield surface, while on the surface itself, it demonstrates plasticity behavior. The yield surface is represented by a yield function (ϕ).

$$\phi(\sigma_{ij}, {\varepsilon_{ij}}^{p}, \eta, L, \kappa) = 0 \tag{2.20}$$

This yield function depends on the stress state, plastic strain state, stress triaxiality (η), Lode parameter (L) and hardening constants. It is used to determine whether the material is in the deformation region.

$$\begin{cases} \phi < 0, & elastic \\ \phi = 0, & plastic \end{cases} \tag{2.21}$$

The material undergoes elastic deformation when ϕ is less than zero. If ϕ equals zero, the material is within the plastic region. The stress state cannot exceed the yield

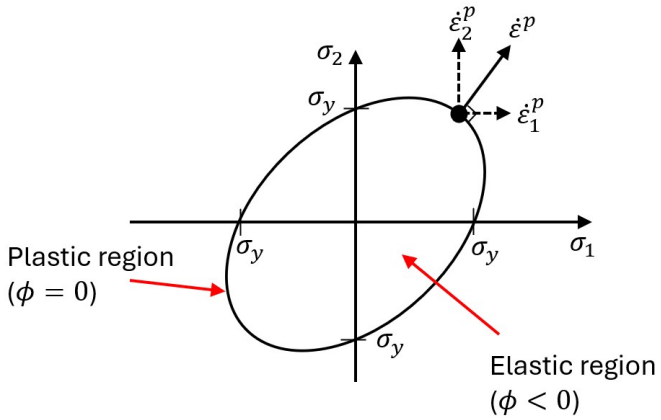

Figure 2.3: Yield surface, showing the increment in plastic strain.

surface. The radial return mapping algorithm, which will be discussed later, is utilized to ensure this.

In a material that has yielded, plastic flow occurs, and the direction of this flow must be determined. The flow rule is used to establish the flow direction, as illustrated in Figure 2.3. The associated flow rule is expressed by the following expression:

$$\dot{\boldsymbol{\varepsilon}^p} = \dot{\lambda}\frac{\partial \phi}{\partial \boldsymbol{\sigma}} \tag{2.22}$$

The direction of the plastic strain increment (or equivalently, the plastic strain rate) is given by $\frac{\partial \phi}{\partial \boldsymbol{\sigma}}$. In contrast, the magnitude of the plastic strain rate is determined by $\dot{\lambda}$. This quantity, known as the plastic multiplier, will be discussed in more detail later.

Yield criteria are functions used to model the plastic behavior of the material. While some functions are included in the ABAQUS interface, functions that are not included can be run in this environment by writing to the subroutine. This section examines two different yield functions used in this study: the Von Mises (VM) yield function and the Bai-Wierzbicki (BW, [87]) yield function. The VM yield function is known as the J2 flow theory and controls plastic flow via the second invariant of the deviatoric stress tensor. It neglects the effects of stress triaxiality and the Lode parameter and is often used to describe the plastic response of metals. Nonetheless, in some materials, these two parameters play an important role. The BW model is a flow function in which the effects of stress triaxiality and the Lode parameter are included. In this study, both models are coded with a subroutine and used in material modeling. Both

yield functions can apply hardening rules. The subroutine of VM is validated against the existing in ABAQUS, while the BW subroutine is compared with experimental results for Al2024-T351 by [87, 96] in the literature. Comparisons have shown that the implemented codes work correctly.

2.2.1.1 Von Mises Yield Criterion

The yield function of von Mises plasticity (ϕ) is based on the second invariant of the deviatoric stress tensor. It is defined by the difference of the norm of the deviatoric stress ($\boldsymbol{\sigma'}$) and the yield stress function (σ_y):

$$\phi = \sqrt{\frac{3}{2}}\|\boldsymbol{\sigma'}\| - \sigma_y = q - \sigma_y \tag{2.23}$$

where σ_y is the yield stress function used to model the hardening behavior of the material. This function typically depends on the equivalent plastic strain, but it can also incorporate the effects of temperature or equivalent plastic strain rate. q represents the von Mises equivalent stress and is defined by Equation 2.9. This criterion states that if the von Mises equivalent stress equals the value of the yield stress function, the material yields.

The associated flow rule for the Von Mises yield criterion states that the plastic strain rate tensor, $\dot{\boldsymbol{\varepsilon}^p}$, is normal to the yield surface in stress space and can be expressed using Equation 2.22:

$$\dot{\boldsymbol{\varepsilon}^p} = \dot{\lambda}\sqrt{\frac{3}{2}}\frac{\boldsymbol{\sigma'}}{\|\boldsymbol{\sigma'}\|} = \dot{\lambda}\frac{3\boldsymbol{\sigma'}}{2q} \tag{2.24}$$

where $\boldsymbol{\sigma'}$ is the deviatoric stress and $\dot{\lambda}$ is the plastic multiplier.

2.2.1.2 Bai-Wierbicki Yield Criterion

The Bai-Wierzbicki (BW) yield function is a more complex model than von Mises, including the effects of hydrostatic stress and the third invariant of the deviatoric stress tensor. This flow function, which includes the stress triaxiality and Lode parameter effects, is handy for materials that cannot be modeled with von Mises. The BW yield

function can be expressed as:

$$\phi = q - \sigma_y \left(1 - c_\eta(\eta - \eta_0)\right) \left[c_s + (c_{ax} - c_s)\left(\gamma - \frac{\gamma^{m+1}}{m+1}\right)\frac{m+1}{m}\right] \tag{2.25}$$

where q is the von Mises equivalent stress, σ_y is yield stress function, c_η is material constant to be calibrated, η_0 is the reference value of stress triaxiality, and η is stress triaxiality. The parameters γ and c_{ax} in the Lode dependent part are defined as follows:

$$\gamma = \frac{cos(\pi/6)}{1 - cos(\pi/6)}\left[\frac{1}{cos(\theta - \pi/6)} - 1\right] = 6.4641[sec(\theta - \pi/6) - 1] \tag{2.26}$$

$$c_{ax} = \begin{cases} c_t & for \bar{\theta} \geq 0 \\ c_c & for \bar{\theta} < 0 \end{cases} \tag{2.27}$$

c_t, c_s, c_c and m are material constants to be calibrated. The triaxiality and Lode parameter-dependent functions are added as a multiplier. The triaxiality-dependent function is linear, and the Lode-dependent function has a quadratic formula. The distributions of triaxiality and Lode parameter functions are shown in Figure 2.4.

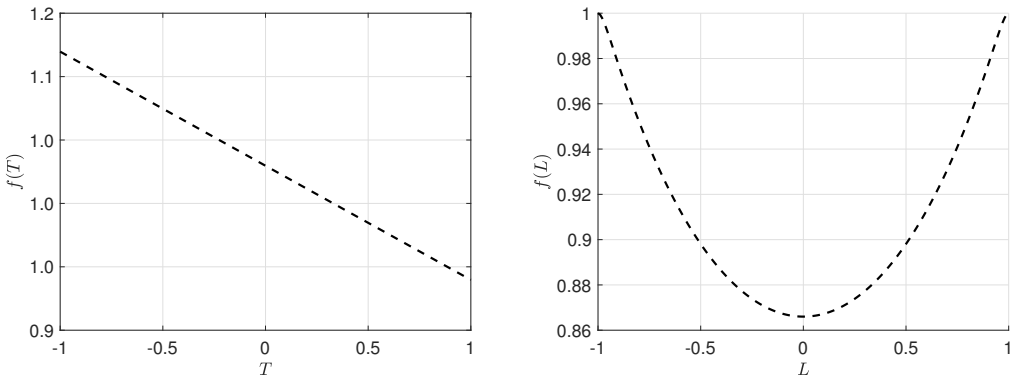

(a) (b)

Figure 2.4: Distribution of (a) triaxiality dependent function depending on T (b) Lode parameter dependent function depending on L

The associated flow rule for the Bai-Wierzbicki is similar to that of the Von Mises but incorporates additional terms to consider hydrostatic stress and the Lode parameter. The plastic strain rate tensor in Equation 2.22 is used, but the stress derivative of the

yield function is different from von Mises. The derivative $\frac{\partial \phi}{\partial \boldsymbol{\sigma}}$ is as follow:

$$\begin{aligned}\frac{\partial \phi}{\partial \boldsymbol{\sigma}} = \frac{\partial q}{\partial \boldsymbol{\sigma}} + \sigma_y c_\eta \left[c_s + (c_{ax} - c_s)\left(\gamma - \frac{\gamma^{m+1}}{m+1}\right)\frac{m+1}{m}\right]\frac{\partial \eta}{\partial \boldsymbol{\sigma}} \\ -\sigma_y \left(1 - c_\eta(\eta - \eta_0)\right)(c_{ax} - c_s)(1 - \gamma^m)\frac{m+1}{m}\frac{\partial \gamma}{\partial \boldsymbol{\sigma}}\end{aligned} \tag{2.28}$$

where $\frac{\partial q}{\partial \boldsymbol{\sigma}}$, $\frac{\partial \eta}{\partial \boldsymbol{\sigma}}$ and $\frac{\partial \gamma}{\partial \boldsymbol{\sigma}}$ are expressed as follow:

$$\frac{\partial q}{\partial \boldsymbol{\sigma}} = \frac{3\boldsymbol{\sigma'}}{2q} \tag{2.29}$$

$$\frac{\partial \eta}{\partial \boldsymbol{\sigma}} = \frac{1}{3q}\boldsymbol{I} - \frac{3\eta}{2q^2}\boldsymbol{\sigma'} \tag{2.30}$$

$$\frac{\partial \gamma}{\partial \boldsymbol{\sigma}} = \left(\frac{3\sqrt{3}}{2-\sqrt{3}}\right)\left(\frac{tan(\theta - \pi/6)}{cos(\theta - \pi/6)}\right)\frac{1}{qsin3\theta}\frac{m+1}{m}\left(\frac{\boldsymbol{I}}{3} + \frac{cos3\theta}{2q}\boldsymbol{\sigma'} - \frac{3}{2q^2}\boldsymbol{\sigma'^2}\right) \tag{2.31}$$

The first term in Equation 2.30 should be neglected. Doing so satisfies the assumption of plastic incompressibility, and the flow rule is applied with deviatoric associativity in plasticity. Additionally, in the original Bai-Wierzbicki model [87], as illustrated in Figure 2.5, the Lode parameter influences the yield function when its values are 1 and -1. However, the yield function should remain unaffected by Lode dependency. For this reason, the term "(m+1)/m", which is more user-friendly and suggested by Algarni et al. [97], has been added as a multiplier in the Lode dependency part. As can be seen in Figure 2.5, this function used by Algarni gives the value 1 when the lode parameter is 1 and -1 and does not affect the yield function.

Another important aspect is ensuring stability and uniqueness in numerical simulations. In this study, since the convexity of the BW yield function depends on the parameters c_t, c_s, c_c and m, it is sufficient to prove the convexity of the Lode-dependent part. The condition for the BW yield function to be convex is as follows:

$$\rho^2 + 2\rho'^2 - \rho\rho'' \geq 0 \tag{2.32}$$

where $\rho = \rho(L)$ is the Lode parameter part of yield function, and its equation is :

$$\rho(L) = \left[c_s + (c_{ax} - c_s)\left(\gamma - \frac{\gamma^{m+1}}{m+1}\right)\frac{m+1}{m}\right] \tag{2.33}$$

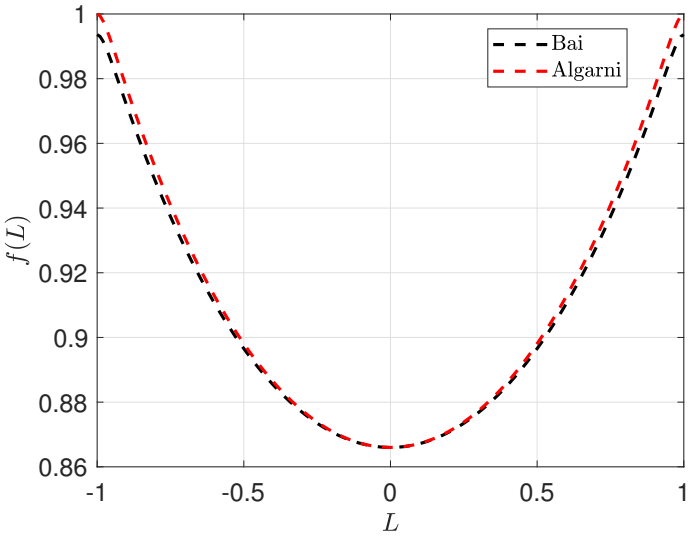

Figure 2.5: Comparison of Lode dependent functions of Bai and Algarni.

Then, Equation 2.32 becomes

$$\begin{aligned}&\left[c_s+(c_{ax}-c_s)\left(\gamma-\frac{\gamma^{m+1}}{m+1}\right)\frac{m+1}{m}\right]^2 \quad +2\left(c_{ax}-c_s\right)^2\left(1-\gamma^m\right)^2\left(\frac{m+1}{m}\right)^2\left(\frac{\partial\gamma}{\partial\theta}\right)^2\\&-\left[c_s+(c_{ax}-c_s)\left(\gamma-\frac{\gamma^{m+1}}{m+1}\right)\frac{m+1}{m}\right]\left(c_{ax}-c_s\right)\frac{m+1}{m}\\&\times\left[\frac{\partial^2\gamma}{\partial\theta^2}-m\gamma^{m-1}\left(\frac{\partial\gamma}{\partial\theta}\right)^2-\gamma^m\frac{\partial^2\gamma}{\partial\theta^2}\right]\geq 0.\end{aligned} \tag{2.34}$$

where γ is :

$$\gamma=\frac{\sqrt{3}}{2-\sqrt{3}}\left[\frac{1}{\cos(\theta-\pi/6)}-1\right] \tag{2.35}$$

When this equation is solved, it is seen that the convexity is governed by c_s/c_{ax} and m [98]. Figure 2.6 shows the valid range in c_s/c_{ax} and m space for the convexity of the presented yield curve where the upper and lower limits of c_s/c_{ax} are shown for various values of m. The convexity condition can be summarized as follows:

$$\frac{\sqrt{3}}{2}\leq\frac{c_\theta^s}{c_\theta^{ax}}\leq 1\Leftrightarrow\frac{\sqrt{3}}{2}\leq\frac{c_\theta^s}{c_\theta^t}\leq 1,\quad\text{and}\quad\frac{\sqrt{3}}{2}\leq\frac{c_\theta^s}{c_\theta^c}\leq 1 \tag{23}$$

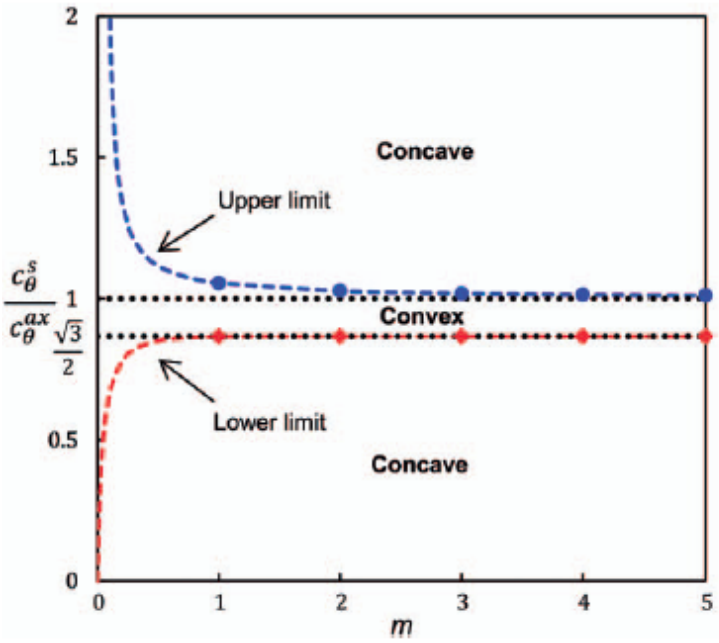

Figure 2.6: The upper and lower for the convexity of the BW yield function [98].

2.2.2 Hardening Rule

In plasticity, the stress that is required for further plastic deformation increases with deformation, which means the material becomes more difficult to deform. This is referred to as the hardening of the material. The hardening rule is utilized to model the stress-strain behavior of a material after it has yielded. Isotropic, kinematic, or combined hardening rules can characterize hardening behavior. Isotropic hardening assumes that the yield surface uniformly expands in all directions, maintaining its shape and center. In contrast, kinematic hardening involves translating the yield surface in stress space without altering its size or shape, effectively capturing the cyclic loading behavior and the Bauschinger effect. Combined hardening is a more complex model that includes isotropic and kinematic hardening behaviors. In this study, isotropic hardening is chosen due to its effectiveness in capturing the overall hardening behavior of materials under monotonic loading conditions. Kinematic hardening is often used under material cyclic loading conditions. Although not commonly used in uniaxial tensile tests, repeated stress reversals can be applied in modeling materials. For simple uniaxial tensile tests, isotropic hardening is usually sufficient. Yield stress functions ($\sigma_y(\bar{\varepsilon}_p)$), dependent on equivalent plastic strain ($\bar{\varepsilon}_p$), are used for modeling

the hardening in the isotropic hardening rule. These functions can also account for temperature and equivalent plastic strain rate effects.

$$\sigma_y(\bar{\varepsilon}_p) = \sigma_0 + R(\bar{\varepsilon}_p) \tag{2.36}$$

where σ_0 is initial yield stress and $R(\bar{\varepsilon}_p)$ is the hardening rule. Isotropic hardening describes a uniform expansion of the yield surface as plastic deformation occurs, maintaining its shape and center as shown in Figure 2.7.

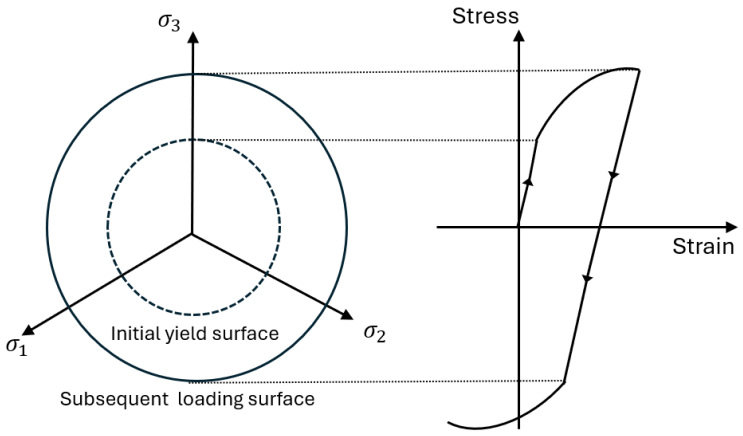

Figure 2.7: Representation of isotropic hardening: The initial yield surface and subsequent loading surface in the stress space, along with the corresponding stress-strain curve.

This section covers several isotropic hardening rules used to model this behavior, including the Voce, Swift, power law, Johnson-Cook, and modulated hardening rules. These hardening rules are essential for accurately capturing the evolution of material strength during plastic deformation and play a vital role in the formulation of plasticity models.

The power hardening rule [99] describes the hardening behavior using a simple power-law relationship. This rule is expressed mathematically with strain hardening exponent (n) and strength coefficient (K):

$$\sigma_y{}^{power} = \sigma_0 + K\bar{\varepsilon}_p^n \tag{2.37}$$

where σ_0 is the initial yield stress and $\bar{\varepsilon}_p$ is the equivalent plastic strain.

The Swift hardening rule [100] characterizes the hardening behavior with a power-law relationship, similar to the power rule, but includes an initial strain term (ε_0):

$$\sigma_y{}^{swift} = \sigma_0 + K(\varepsilon_0 + \bar{\varepsilon}_p)^n \tag{2.38}$$

Voce hardening rule [101] defines the hardening behavior by formulating the equivalent plastic strain value as exponential. The Voce hardening law is mathematically expressed as:

$$\sigma_y{}^{voce} = \sigma_0 + \left[q_1\left(1 - e^{(-b_1\bar{\varepsilon}_p)}\right) + q_2\left(1 - e^{(-b_2\bar{\varepsilon}_p)}\right)\right] \tag{2.39}$$

where q_1, q_2, b_1 and b_2 are material constants.

The extended Voce hardening rule provides a more detailed description of hardening behavior by incorporating additional parameters:

$$\sigma_y{}^{exvoce} = \sigma_0 + \left[q_1\left(1 - c_1e^{(-b_1\bar{\varepsilon}_p)}\right) + q_2\left(1 - c_2e^{(-b_2\bar{\varepsilon}_p)}\right)\right] \tag{2.40}$$

where q_1, q_2, b_1, b_2, c_1 and c_2 are material constants.

The modulated hardening rule [102] combines the effects of multiple hardening rules to offer a comprehensive characterization of hardening behavior, also known as the weighted average method because two different hardening rules are used.

$$\sigma_y{}^{modulated} = \alpha(\sigma_{swift}) + (1 - \alpha)(\sigma_{exvoce}) \tag{2.41}$$

where α is a weighting factor.

The Johnson-Cook plasticity model [40] incorporates the effects of strain rate and temperature on the hardening behavior. This rule is expressed as:

$$\sigma_y{}^{JC} = [A + B(\bar{\varepsilon}_p)^n]\left[1 + C\ln\frac{\dot{\bar{\varepsilon}}_p}{\dot{\varepsilon}_0}\right]\left[1 - \hat{\theta}^m\right] \tag{2.42}$$

where: A,B,C,m,n and $\dot{\varepsilon}_0$ are material constants, $\dot{\bar{\varepsilon}}_p$ is the plastic strain rate, $\dot{\varepsilon}_0$ is the reference strain rate, $\hat{\theta}$ is a temperature-dependent function defined as:

$$\hat{\theta} = \begin{cases} 0, & \text{if } \theta < \theta_{trans} \\ (\theta - \theta_{trans})/(\theta_{melt} - \theta_{room}), & \text{if } \theta_{room} \leq \theta \leq \theta_{melt} \\ 1, & \text{if } \theta > \theta_{melt} \end{cases} \tag{2.43}$$

where θ, θ_{room} and θ_{melt} are the current, room and melting temperature of the material, respectively. By including the strain rate and temperature factors in this plastic rule as multipliers in other models, other plasticity models can also become strain rate and temperature-dependent.

2.2.3 Implementation and Comparison of Yield Functions

Accurate simulation of material behavior under various loading conditions is crucial, and one of the commonly used methods for time integration of plasticity with isotropic hardening is the radial return mapping algorithm. This algorithm employs the Newton-Raphson method to solve for the plastic strain increment iteratively, updating the stress state during plastic loading. This algorithm is implemented within the VUMAT subroutine in Abaqus. The VUMAT subroutine in ABAQUS/Explicit is a user-defined interface that enables the implementation of custom material models not available in the standard ABAQUS. This capability is used to simulate complex material behaviors, such as advanced yield functions and damage mechanics, which standard models cannot capture. The subroutine allows for the utilization and updating of state variables during analysis.

This section explains the stress and strain relations required for implementation using current and previous states in detail. While the general framework for von Mises (VM) and Bai-Wierzbicki (BW) yield functions is similar, differences arise in the computation of stress normal, incremental plastic strain, and stress updates. These differences are crucial for accurately capturing the distinct behaviors predicted by each yield function.

Rate-independent von Mises plasticity is expressed using the Cauchy stress tensor, with fundamental stress and strain definitions applied in implementing the yield function and flow rule. The formulation of the Cauchy stress tensor is as follows:

$$\boldsymbol{\sigma} = 2\mu\, dev(\boldsymbol{\varepsilon}^e) + \kappa\, tr(\boldsymbol{\varepsilon}^e) \tag{2.44}$$

where μ is shear modulus and it is formulated with Young's modulus (E) and Poisson's ratio (ν) as follow:

$$\mu = \frac{E}{1+\nu} \tag{2.45}$$

and κ is Bulk modulus and it is formulated as follow:

$$\kappa = \frac{E}{1+\nu}\frac{\nu}{1-2\nu} \tag{2.46}$$

Moreover, $dev(\boldsymbol{\varepsilon}^e)$ is the deviatoric part of the elastic strain tensor, and $tr(\boldsymbol{\varepsilon}^e)$ is the trace of the elastic strain tensor. In von Mises plasticity, since the deviatoric part describes the flow, the trace of the plastic strain is zero. The same applies to the BW yield function, as the function has been made deviatoric by removing the volumetric term from the stress triaxiality-dependent part. Therefore, the total strain equals the elastic strain and is denoted by the trace of the strain 'e'. All in all, Cauchy's stress can be expressed as follows:

$$\boldsymbol{\sigma} = 2\mu\left(\boldsymbol{\varepsilon}' - \boldsymbol{\varepsilon}^p\right) + \kappa e\boldsymbol{I} \tag{2.47}$$

The implementation aims to find the current incremental plastic strain and update the stress tensor using the plastic strain rate tensor in Equation 2.22. For this purpose, the Euler scheme is used:

$$\boldsymbol{\varepsilon}^p_{n+1} = \boldsymbol{\varepsilon}^p_n + \gamma_{n+1}\boldsymbol{n}_{n+1} \tag{2.48}$$

Here, $\boldsymbol{n}_{n+1}$ represents the direction of plastic strain, and its formulation and implementation differ for the two yield functions. The equations for the direction of plastic strain for both yield functions are defined as follows:

$$\boldsymbol{n}_{n+1_{VM}} = \frac{3\boldsymbol{\sigma'_{n+1}}}{2q} \tag{2.49}$$

$$\begin{aligned}\boldsymbol{n}_{n+1_{BW}} = {} & \frac{3\boldsymbol{\sigma'_{n+1}}}{2q} + \sigma_y c_\eta\left[c_s + (c_{ax}-c_s)\left(\gamma\frac{\gamma^{m+1}}{m+1}\right)\frac{m+1}{m}\right]\left(-\frac{3\eta}{2q^2}\boldsymbol{\sigma'_{n+1}}\right) \\ & - \sigma_y\left(1 - c_\eta(\eta-\eta_0)\right)(c_{ax}-c_s)(1-\gamma^m)\frac{m+1}{m}\left(\frac{3\sqrt{3}}{2-\sqrt{3}}\right)\left(\frac{tan(\theta-\pi/6)}{cos(\theta-\pi/6)}\right) \\ & \frac{1}{qsin3\theta}\left(\frac{\boldsymbol{I_{n+1}}}{3} + \frac{cos3\theta}{2q}\boldsymbol{\sigma'_{n+1}} - \frac{3}{2q^2}\boldsymbol{\sigma'^2_{n+1}}\right)\end{aligned} \tag{2.50}$$

The stress values are used to calculate the stress triaxiality and Lode parameter in these formulas. These values are needed to calculate the current stress value ($\boldsymbol{\sigma_{n+1}}$). Therefore, these values are calculated with the previous stress values ($\boldsymbol{\sigma_n}$).

Plug Equation 2.48 into Equation 2.47 to get the algorithmic stress expression,

$$\boldsymbol{\sigma}_{n+1} = \kappa e_{n+1}\mathbf{1} + 2\mu\left(\boldsymbol{\varepsilon}'_{n+1} - \boldsymbol{\varepsilon}^p_n\right) - 2\mu\gamma_{n+1}\boldsymbol{n}_{n+1} \tag{2.51}$$

Since von Mises plasticity theory is driven by deviatoric stresses, the sole purpose of this algorithm is to find the deviatoric part of the final stress. Therefore, deviatoric stress and trial deviatoric stresses should be written as follows:

$$\begin{aligned} \boldsymbol{\sigma}'_{n+1} &= \underbrace{2\mu\left(\boldsymbol{\varepsilon}'_{n+1} - \boldsymbol{\varepsilon}^{p}_{n}\right)}_{\text{Elastic Predictor}} \underbrace{-2\mu\gamma_{n+1}\boldsymbol{n}_{n+1}}_{\text{Plastic Corrector}} \\ \boldsymbol{\sigma}'_{n+1} &= \boldsymbol{\sigma}'^{,\,\text{trial}}_{n+1} - 2\mu\gamma_{n+1}\boldsymbol{n}_{n+1} \end{aligned} \tag{2.52}$$

The trial stress represents the stress considering it to be completely elastic, serving as a predictor subsequently adjusted by the plastic correction component based on the state of the yield function. This is represented as follows:

$$\left\|\boldsymbol{\sigma}'_{n+1}\right\| = \left\|\boldsymbol{\sigma}'^{,trial}_{n+1}\right\| - 2\mu\gamma_{n+1}\sqrt{\frac{3}{2}} \tag{2.53}$$

Now, plug Equation 2.53 into the Equations 2.23 write in algorithmic form of VM yield function,

$$\phi_{n+1_{VM}} = \sqrt{\frac{3}{2}}\left\|\boldsymbol{\sigma}'^{,trial}_{n+1}\right\| - 3\mu\gamma_{n+1} - (\sigma_y) \tag{2.54}$$

To calculate the trial stress in the BW yield function, two additional values are required. These are the function values of the stress triaxiality and Lode parameter. Since these functions involve stress values and the stress has not yet been updated in the current step, the stress values from the previous step are used to compute these two functions. Their algorithmic forms are as follows,

$$\begin{aligned} f_n(\eta) &= (1 - c_{\eta_n}(\eta - \eta_0)) \\ g_n(L) &= \left[c_s + (c_{ax} - c_s)\left(\gamma_n - \frac{\gamma_n^{m+1}}{m+1}\right)\frac{m+1}{m}\right] \end{aligned} \tag{2.55}$$

where γ_n is :

$$\gamma_n = \frac{\sqrt{3}}{2-\sqrt{3}}\left[\frac{1}{\cos(\theta_n - \pi/6)} - 1\right] \tag{2.56}$$

Thus, by incorporating these two functions, plug Equation 2.53 into the Equations 2.25 write in algorithmic form of BW yield function,

$$\phi_{n+1_{BW}} = \sqrt{\frac{3}{2}}\left\|\boldsymbol{\sigma}'^{,trial}_{n+1}\right\| - 3\mu\gamma_{n+1} - (\sigma_y f_n(\eta) g_n(L)) \tag{2.57}$$

For an elastic step, $\phi_{n+1} < 0$ and for a plastic step $\phi_{n+1} = 0$. In the algorithm, a trial yield function is introduced and checked whether the step is elastic $\left(\phi^{\text{trial}}_{n+1} < 0\right)$ or plastic $\left(\phi^{\text{trial}}_{n+1} > 0\right)$.

$$\phi^{\text{trial}}_{n+1_{VM}} = \sqrt{\frac{3}{2}}\left\|\boldsymbol{\sigma}'^{,trial}_{n+1}\right\| - (\sigma_y) \tag{2.58}$$

$$\phi^{\text{trial}}_{n+1_{BW}} = \sqrt{\frac{3}{2}} \left\| \boldsymbol{\sigma}'^{,trial}_{n+1} \right\| - (\sigma_y f_n(\eta) g_n(L)) \tag{2.59}$$

If the step is elastic ($\gamma_{n+1} = 0$),

$$\begin{aligned} \boldsymbol{\sigma}'_{n+1} &= \boldsymbol{\sigma}'^{,\,\text{trial}}_{n+1} \\ \boldsymbol{\sigma}_{n+1} &= \kappa e_{n+1} \mathbf{1} + 2\mu \left(\boldsymbol{\varepsilon}'_{n+1} - \boldsymbol{\varepsilon}^p_n \right) \end{aligned} \tag{2.60}$$

If the step is plastic then γ_{n+1} needs to be calculated using the Newton-Raphson method since the hardening function is non-linear. This method uses the yield function ϕ_{n+1}. The algorithm continues to do the following calculations until $|\phi_{n+1}| <$ tolerance. For Newton-Raphson, a function, the first derivative of that function, and an initial value are needed. Swift hardening rule is used as an example. Formulas in this algorithm are as follows for VM:

$$\begin{aligned} f_{n+1} &= \phi_{n+1_{VM}} \\ f'_{n+1} &= \frac{\partial \phi_{n+1}}{\partial \gamma_{n+1}} = -3\mu - \sigma'_y \\ \sigma'_y &= Kn(\varepsilon_0 + \alpha_{n+1})^{n-1} \\ \gamma_{n+1} &= \gamma_{n+1} - \frac{f_{n+1}}{f'_{n+1}} \end{aligned} \tag{2.61}$$

and for BW:

$$\begin{aligned} f_{n+1} &= \phi_{n+1_{BW}} \\ f'_{n+1} &= \frac{\partial \phi_{n+1}}{\partial \gamma_{n+1}} = -3\mu - \sigma'_y \\ \sigma'_y &= Kn(\varepsilon_0 + \alpha_{n+1})^{n-1} f_n(\eta) g_n(L) \\ \gamma_{n+1} &= \gamma_{n+1} - \frac{f_{n+1}}{f'_{n+1}} \end{aligned} \tag{2.62}$$

Now γ_{n+1} is found and Equations 2.47 and 2.48 can be updated.

2.2.3.1 Validation of VUMAT Implementation

The Von Mises (VM) and Bai-Wierzbicki (BW) yield functions are implemented in the ABAQUS environment using a user-defined material subroutine (VUMAT). In this part, a VUMAT subroutine is initially developed for the VM yield function and validated by comparing the VM yield function available in ABAQUS. The Al2024-T351 material is employed for this validation, as used by Bai et al. [87] and Bao

[96]. Experimental data for standard round tensile specimens (ST) and round notched specimens with radius of 4 mm (R4) and 12 mm (R12) are sourced from the thesis in [96], while data for flat-grooved specimens (FG) are obtained from the article in [87]. Details of the specimen geometries and parameters can be found in [103]. The following hardening formula is utilized as described in [103]:

$$\sigma_y = A(\varepsilon_0 + \bar{\varepsilon}_p)^n + K + Q\left(1 - e^{(-B\bar{\varepsilon}_p)}\right) \tag{2.63}$$

All plasticity parameters are presented in Table 2.1. Only the parameters in the first row of the table are used for the VM yield function.

Table 2.1: Plasticity model parameters for Al2024-T351 [103, 87].

A[MPa]	ε_0	n	K [MPa]	Q[MPa]	B
320	0.0052	0.195	235	135	7.8
c_η	η_0	c_t	c_c	c_s	m
0.09	0.333	1	1.02	0.92	6

In this section, the results for the VM yield function are presented, using both the developed subroutine and ABAQUS in-built model. The following section will also present comparisons with experimental data for both the VM and BW yield functions. The equivalent plastic strain distribution and force-displacement curves of four specimens are illustrated in Figures 2.8 and 2.9.

Comparison between ABAQUS and VUMAT simulations for different specimen geometries shows a high degree of consistency in both equivalent plastic strain (PEEQ) distributions and force-displacement curves. For the ST, R4, R12, and FG geometries, the strain distribution predicted by the developed VUMAT subroutine closely matches the results from the in-built ABAQUS model, demonstrating the accuracy of the VUMAT subroutine across various geometries. Force-displacement curves confirm this accuracy, with nearly identical results for both simulations. These results show that the VUMAT subroutine reliably captures the material's response under tensile loading and complex stress-state conditions.

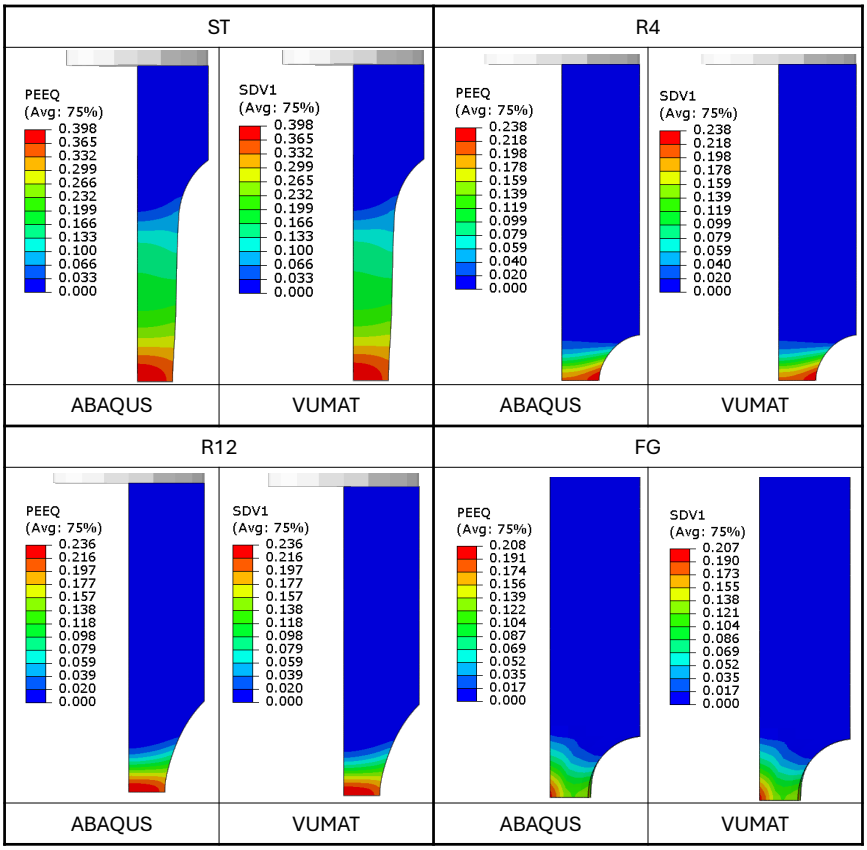

Figure 2.8: Comparison of equivalent plastic strain for different specimen geometries in ABAQUS and VUMAT simulations.

2.2.3.2 Comparison of von Mises and Bai-Wierzbicki Yield Functions

This section compares von Mises (VM) and Bai-Wierzbicki (BW) yield functions. The VUMAT subroutine running for the VM has been modified for the BW yield function. The differences between the VM and BW subroutines are as follows. In BW, the stress triaxiality and Lode parameter are calculated using the stresses mentioned in the previous step. The yield stress function depends on these two parameters, and plasticity is checked with this yield stress function. Plastic strain normal differs from VM as its formula is given in the above section. Finally, the yield function of BW and its derivative according to plastic strain are used to find the incremental plastic strain in the Newton-Raphson method of BW. The results obtained for validating BW are compared with the experimental data provided in the literature. The plasticity parameters for hardening and the Lode parameter, excluding the stress

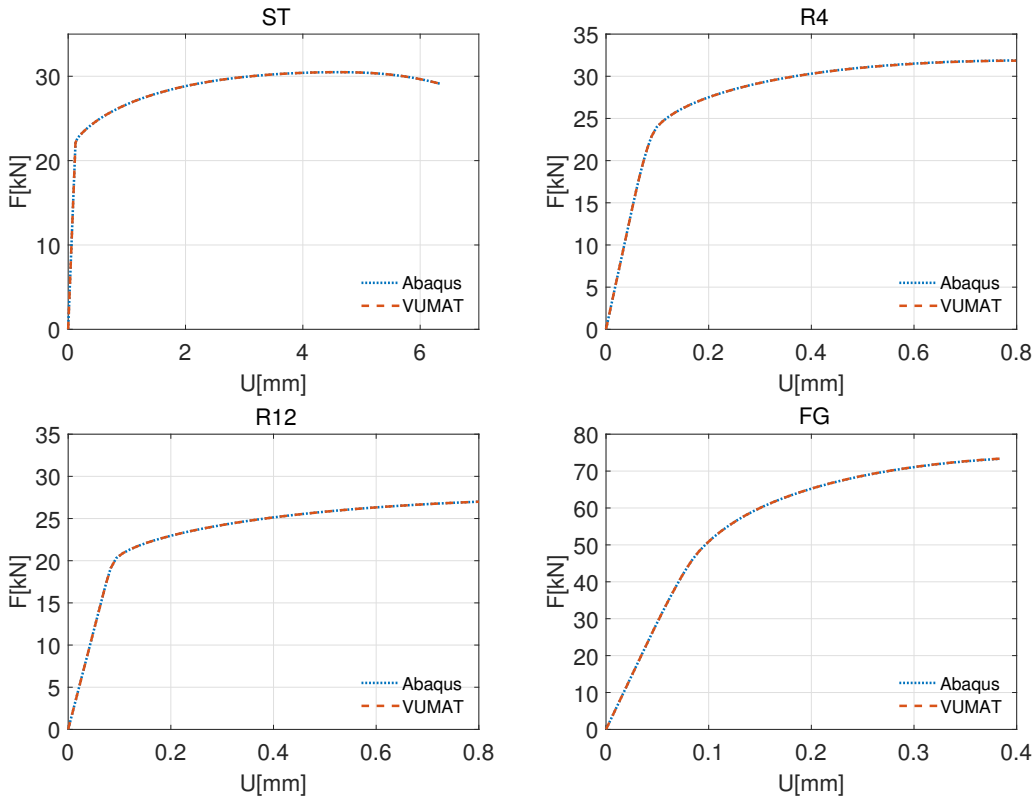

Figure 2.9: Force-displacement curves for different specimen geometries, comparing VUMAT and ABAQUS.

triaxiality parameters, are taken from [103], which works with the AL2024-T351 material used by [87] and [96]. The stress triaxiality formula used in this study differs from the original; however, when comparing the function used here with the original, similar results are obtained, leading to the decision to adhere to the original formulas. The stress triaxiality parameters are taken from [87]. The hardening rule is shown in Equation 2.63, and the yield function is presented in Equation 2.25. The accuracy of the developed code has been demonstrated using the parameters shown in Table 2.1.

The force-displacement curves obtained using the VM and BW yield functions are shown in Figure 2.10. The orange curves represent the results for VM plasticity without any corrections, while the yellow curves correspond to BW with corrections applied for stress triaxiality and the Lode parameter. For the Al2024-T351 material, the results indicate that the VM yield function aligns with the experimental data only for the ST specimen but fails to predict the plastic behavior of the other three specimens accurately. In contrast, the results obtained with the BW yield function show strong

agreement with the experimental data across all specimens, demonstrating that the applied corrections lead to a more accurate prediction of plasticity. This comparison highlights the performance and accuracy differences between the two yield functions, with the BW function proving to capture material behavior under various stress state conditions more precisely.

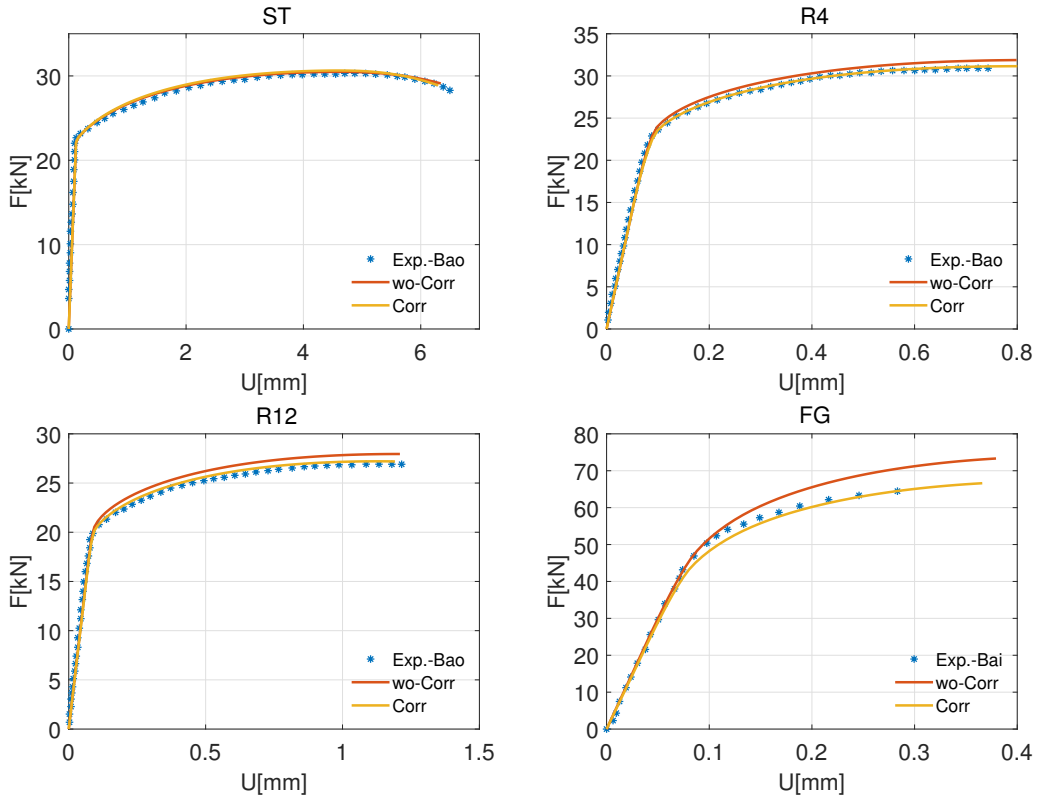

Figure 2.10: Force-displacement curves for different specimen geometries, comparing experimental results with simulations using models without correction and with correction. Exp-Bai is the experimental data in the article [87] written by Bai et al. and Exp-Bao is the experimental data in the thesis [96] written by Bao.

Additionally, to assess the individual effect of stress triaxiality and the Lode parameter on each geometry, results are obtained where only stress triaxiality or only the Lode parameter is active. Figure 2.11 illustrates the outcomes corresponding to the stress triaxiality correction (T-Corr) and the Lode parameter correction (L-Corr). While stress triaxiality and Lode parameter correction do not cause a change in the ST specimen, it is seen that stress triaxiality causes a more significant change than the Lode parameter in the R4 specimen. In the R12 specimen, the stress triaxiality and

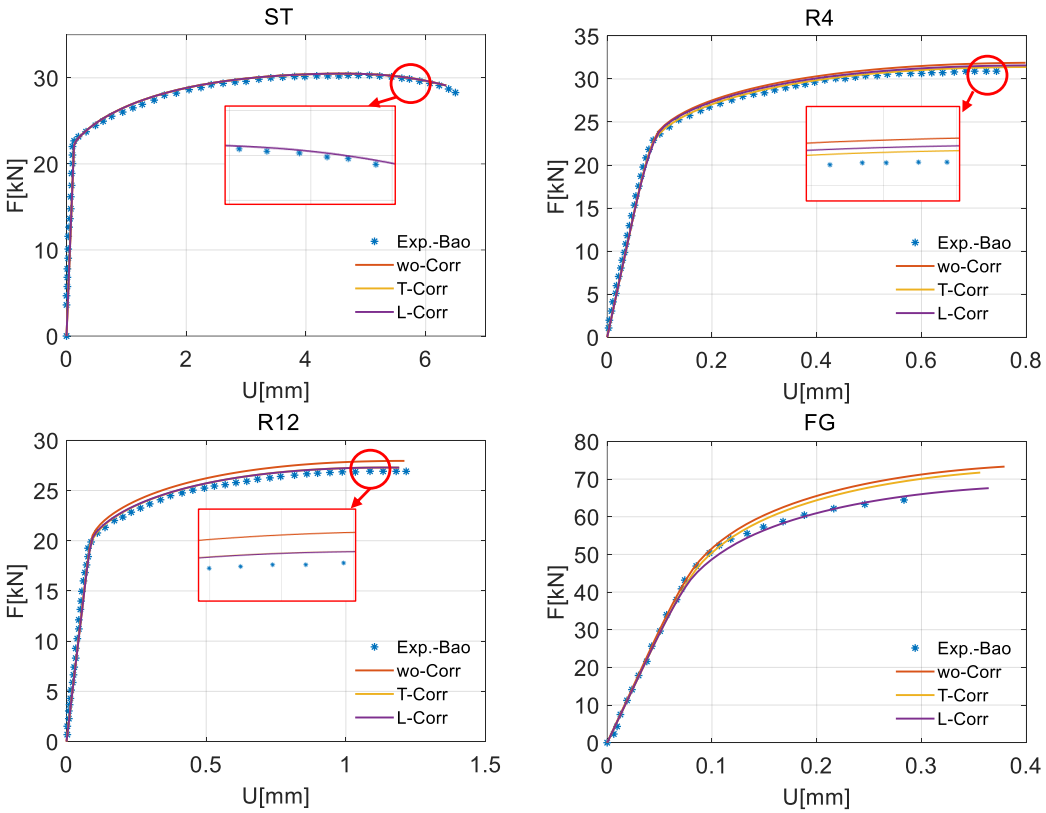

Figure 2.11: Force-displacement curves for different specimen geometries, comparing experimental results with simulations using models without correction, stress triaxiality correction, and Lode parameter correction.

Lode parameters equally change the hardening of the material. As expected, since the FG specimen has a shear stress state, the Lode parameter alone performs almost all the correction, while the effect of stress triaxiality is slight.

2.3 Formulation and Implementation of Damage Models

Accurate prediction of material damage under different loading conditions requires using various uncoupled damage models. Since these uncoupled damage models work independently of plasticity, they do not cause a change in the stress state of the material, and it is easy to calibrate the damage parameters. These models describe fracture in the material in terms of mechanical variables such as stress, deformation, temperature, and deformation rate. In all models presented in this study, the fracture

model is a function dependent on these variables, and damage accumulation (D) is calculated using this function. An integral rule calculates damage accumulation and has a linear relationship with the equivalent plastic stain. This rule can be written differently for models with single and multiple parameters. In single models, one critical damage value (D_c) normalizes the damage accumulation rule. Consequently, when the value of D reaches 1, the material fails. The integral is written as follows:

$$\begin{aligned} D_c &= \int_0^{\bar{\varepsilon}_p} g(\sigma_{ij}) d\bar{\varepsilon}_p \\ D &= \frac{1}{D_c} \int_0^{\bar{\varepsilon}_p} g(\sigma_{ij}) d\bar{\varepsilon}_p \end{aligned} \tag{2.64}$$

Models with multiple parameters are denoted by ε_f and can be defined as the integral weighted by the inverse of ε_f of the equivalent plastic deformation $\bar{\varepsilon}_p$. This integral, which shows the fracture state of the material, is shown as follows:

$$D = \int_0^{\bar{\varepsilon}_p} \frac{d\bar{\varepsilon}_p}{\varepsilon_f} \tag{2.65}$$

Similarly, in multiple-parameter models, fracture is expected to occur in the material when the D parameter reaches a critical value (D=1). In this section, we focus on formulating and implementing uncoupled damage models in the ABAQUS software environment. Emphasis is placed on the formulation of single-parameter damage models, multiple-parameter damage models, and ABAQUS subroutines used for damage modeling.

2.3.1 Single Parameter Damage Criteria

Single-parameter damage models simplify material parameter calibration by using a single experiment to represent damage, making them easier to implement and computationally efficient. Various models in the literature have a single parameter to calibrate. These models calculate fracture directly based on changes in principal or equivalent stress. In the thesis, ten different models with a single damage parameter are used. Each of these models gives a different insight into the material behavior. These models will be calibrated against experimental data to predict the onset of damage under various stress-state. Table 2.2 gives all damage criteria and relevant equations.

Table 2.2: Brief summary of single parameter uncoupled damage criteria.

Criterion	Damage Relation
Ayada [104]	$D = \frac{1}{C_1}\int_0^{\bar{\varepsilon}_p} \langle \frac{\sigma_m}{\bar{\sigma}} \rangle d\bar{\varepsilon}_p$
Ayada-m [68]	$D = \frac{1}{C_2}\int_0^{\bar{\varepsilon}_p} \langle \frac{\sigma_m}{\bar{\sigma}} + \frac{1}{3} \rangle d\bar{\varepsilon}_p$
Brozzo [105]	$D = \frac{1}{C_3}\int_0^{\bar{\varepsilon}_p} \frac{2\sigma_1}{3(\sigma_1 - \sigma_m)} d\bar{\varepsilon}_p$
Ko-Huh (KH, [106])	$D = \frac{1}{C_4}\int_0^{\bar{\varepsilon}_p} \frac{\sigma_1}{\bar{\sigma}} \langle 1 + 3\frac{\sigma_m}{\bar{\sigma}} \rangle d\bar{\varepsilon}_p$
Le-Roy (LR, [107])	$D = \frac{1}{C_5}\int_0^{\bar{\varepsilon}_p} (\sigma_1 - \sigma_m) d\bar{\varepsilon}_p$
McClintock (MC, [20])	$D = \frac{1}{C_6}\int_0^{\bar{\varepsilon}_p} \left[\frac{\sqrt{3}}{2(1-n)} sinh\left(\frac{\sqrt{3}}{2(1-n)} \frac{\sigma_1 + \sigma_2}{\bar{\sigma}} \right) + \frac{3}{4}\frac{\sigma_1 - \sigma_2}{\bar{\sigma}} \right] d\bar{\varepsilon}_p$
OH [41]	$D = \frac{1}{C_7}\int_0^{\bar{\varepsilon}_p} \frac{\langle \sigma_1 \rangle}{\bar{\sigma}} d\bar{\varepsilon}_p$
Rice-Tracey (RT, [21])	$D = \frac{1}{C_8}\int_0^{\bar{\varepsilon}_p} exp\left(\frac{3\sigma_m}{2\bar{\sigma}} \right) d\bar{\varepsilon}_p$
CL [39]	$D = \frac{1}{C_9}\int_0^{\bar{\varepsilon}_p} \langle \sigma_1 \rangle d\bar{\varepsilon}_p$
Freudenthal [108]	$D = \frac{1}{C_{10}}\int_0^{\bar{\varepsilon}_p} \bar{\sigma} d\bar{\varepsilon}_p$

σ_1 and σ_2 are the first and second principal stress, respectively. σ_m is the mean stress ($\sigma_m = (\sigma_{11} + \sigma_{22} + \sigma_{33})/3$) and $\bar{\sigma}$ is the von-Mises equivalent stress. C_i' are the critical value of damage to be calibrated from experiments and $\langle . \rangle$ is the Macaulay bracket. Although the damage criteria do not have any temperature-related term, they are indirectly related to temperature through the stress term. For all models, the material is assumed to be initially defect-free ($D = 0$), and failure occurs when D reaches 1.

The Ayada model describes void growth through a stress triaxiality parameter, while the cut-off value 1/3 is supplemented in the Ayada-m model as a modification. Both the effects of normalized maximum principal stress and stress triaxiality are combined in the KH model. In the LR model, the nucleation, shape change, and coalescence of voids are considered to incorporate the maximum principle and hydrostatic stress difference. The Oh model normalizes the first principle stress with equivalent stress. The RT model relies on an exponential function of stress triaxiality. McClintock's model considers the equivalent stress, transverse principal stresses, and an exponent for strain hardening. In this criterion, the parameter n is determined using the hardening rule, which is why this model is classified among single-parameter models. The maximum principal stress is incorporated in the CL, while the von Mises equivalent

stress is considered in the case of Freudenthal. Remarkably, all criteria include only a single parameter to be calibrated from a single experiment.

2.3.2 Multiple Parameter Damage Criteria

Multi-parameter damage models combine multiple parameters, providing a more detailed and accurate representation of material degradation. These models capture the complex interactions between different damage mechanisms, such as microcrack initiation, growth, and coalescence. Multi-parameter models are beneficial for materials and loading conditions where damage behavior is highly nonlinear and depends on various factors such as stress triaxiality and the Lode parameter. However, since there are multiple parameters to be calibrated, various experimental tests are needed, making the criteria calibration procedure difficult.

This study utilizes various fracture models dependent on stress triaxiality and the Lode parameter to calibrate damage parameters for both materials. Both stress triaxiality dependent models such as Oyane-Sato [109] and Johnson-Cook [40] models, as well as models from the Wierzbicki group, including Bai-Wierzbicki (BW, [87]) and modified Mohr-Coulomb (MMC, [32]); along with the Lou damage family, including DF2013 [110], DF2014 [44] and DF2015 [111]. The JC and MMC damage models are studied in their temperature and strain rate-dependent forms, whereas the effects of temperature and strain rate are not included in the other models. Damage parameters are denoted as D_{ij}, where i represents the model and j denotes the number of parameters associated with that model. For instance, the damage parameters for the Oyane-Sato model are D_{11} and D_{12}, while those for the JC model are D_{21}, D_{22}, D_{23}, D_{24}, and D_{25}. In the equations, η, L and $\bar{\theta}$ are the dimensionless parameters: stress triaxiality, Lode parameter and Lode angle parameter, respectively.

Oyane and Sato is similar to the Ayada model, based on two damage parameters and stress triaxiality. The formulation of the model is as follows:

$$D = \frac{1}{D_{11}} \int_0^{\bar{\varepsilon}_p} (\eta + D_{12}) d\bar{\varepsilon}_p \tag{2.66}$$

In the JC model, the term in the first bracket represents the effect of stress triaxiality. In contrast, the second and third brackets refer to the equivalent plastic strain rate and

temperature effects. In particular, even if the effect of the Lode angle is ignored, this model includes the effects of strain triaxiality and these two effects.

$$\varepsilon_f^{JC} = [D_{21} + D_{22}\exp(-D_{23}\eta)]\left[1 + D_{24}\ln\left(\frac{\dot{\bar{\varepsilon}}_p}{\dot{\varepsilon}_0}\right)\right]\left[1 + D_{25}\hat{\theta}\right] \tag{2.67}$$

$\dot{\varepsilon}_0$ is the reference strain rate, $\dot{\bar{\varepsilon}}_p$ is the rate of plastic strain and $\hat{\theta}$ is given by the following relation.

$$\hat{\theta} = \begin{cases} 0, & \text{if } \theta < \theta_{trans} \\ (\theta - \theta_{trans})/(\theta_{melt} - \theta_{trans}), & \text{if } \theta_{trans} \leq \theta \leq \theta_{melt} \\ 1, & \text{if } \theta > \theta_{melt} \end{cases} \tag{2.68}$$

where θ, θ_{trans} and θ_{melt} are the current, transition and melting temperature of the material, respectively.

Two different damage models belonging to Wierzbicki's group are used. In the BW model, the failure model is formulated with two constants in the tension, shear and compression parts, and six constants in total. In this model, where stress triaxiality and Lode angle parameters are used, only the terms used for tension and shear cases remain in the case where tension and compression are symmetrical to each other. In this study, due to the lack of testing, the first one is considered symmetric, but all six parameters are modeled with the iterative method.

$$\begin{aligned} \varepsilon_f^{BW} = &\left[\frac{1}{2}\left(D_{31}e^{-D_{32}\eta} + D_{35}e^{-D_{36}\eta}\right) - D_{33}e^{-D_{34}\eta}\right]\bar{\theta}^2 \\ &+\frac{1}{2}\left(D_{31}e^{-D_{32}\eta} - D_{35}e^{-D_{36}\eta}\right)\bar{\theta} - D_{33}e^{-D_{34}\eta} \end{aligned} \tag{2.69}$$

The MMC model is a prevalent damage model that considers both stress triaxiality and Lode parameter, commonly employed in finite element (FE) simulations to predict ductile failure in metals. This model has been further developed to incorporate the effects of strain rate and temperature. The extended form of the failure criteria is defined as follows:

$$\begin{aligned} \varepsilon_f^{MMC} = &\left[\frac{A_4}{D_{42}}\left[D_{43} + \frac{\sqrt{3}}{2-\sqrt{3}}\left(D_{44} - D_{43}\right)\left(\sec\left(\frac{\bar{\theta}\pi}{6}\right) - 1\right)\right]\right]^{-1/n_4} \\ &* \left[\sqrt{\frac{1 + {D_{41}}^2}{3}}\cos\left(\frac{\bar{\theta}\pi}{6}\right) + D_{41}\left(\eta + \frac{1}{3}\sin\left(\frac{\bar{\theta}\pi}{6}\right)\right)\right]^{-1/n_4} \\ &* \left[1 + D_{24}\ln\left(\frac{\dot{\bar{\varepsilon}}_p}{\dot{\varepsilon}_0}\right)\right]\left[1 + D_{25}\hat{\theta}\right] \end{aligned} \tag{2.70}$$

In addition to D_{ij}, the MMC model includes the material parameters A_4 and n_4. Another group that has worked on models dependent on stress triaxiality and Lode parameter is the group in which Lou is the author. The models proposed in this group include the nucleation, growth and coalescence of the void, and the shear effect is represented in the models with these two parameters. In the DF2013 model, the model is proposed by assuming a cut-off value of -1/3 stress triaxiality, but subsequent studies showed that the cut-off value may differ from this value. For this reason, the DF2014 and DF2015 models introduced the C parameter, and a variable cut-off value could be obtained. Additionally, the DF2015 model includes the D_{74} parameter to further enhance the modeling capabilities.

$$\varepsilon_f^{DF2013} = \frac{D_{53}}{\left(\frac{2}{\sqrt{L^2+3}}\right)^{D_{51}} \left(\frac{\langle 1+3\eta \rangle}{2}\right)^{D_{52}}} \tag{2.71}$$

$$\varepsilon_f^{DF2014} = \frac{D_{63}}{\left(\frac{2}{\sqrt{L^2+3}}\right)^{D_{61}} \left(\left\langle \frac{f(\eta,L,C)}{f\left(\eta=\frac{1}{3},L=-1,C\right)} \right\rangle\right)^{D_{62}}} \tag{2.72}$$

where

$$f(\eta, L, C) = \eta + \frac{3-L}{3\sqrt{L^2+3}} + C_6 \tag{2.73}$$

$$\varepsilon_f^{DF2015} = \frac{D_{73}}{\left(\frac{2}{\sqrt{L^2+3}}\right)^{D_{71}} \left(\left\langle \frac{f(\eta,L,C)}{f\left(\eta=\frac{1}{3},L=-1,C\right)} \right\rangle\right)^{D_{72}}} \tag{2.74}$$

where

$$f(\eta, L, C) = \eta + D_{74}\frac{3-L}{3\sqrt{L^2+3}} + C_7 \tag{2.75}$$

2.3.3 Implementation and Comparison of ABAQUS subroutines

ABAQUS has various plasticity and damage models. Unfortunately, most of them used in the thesis are unavailable in ABAQUS. Therefore, implementing damage models with ABAQUS can be accomplished using various user-defined subroutines. There are various types of subroutines for both implicit and explicit solvers, such as

(V)UMAT, (V)UHARD, and (V)USDFLD. Subroutines starting with 'V' are for the explicit decoder, and their coding algorithms and functions differ in some aspects.

The VUMAT subroutine is thoroughly detailed and tested in previous sections. This section focuses on the VUHARD and VUSDFLD subroutines. These are user-defined subroutines in ABAQUS/Explicit that allow for the customization of material behavior. The VUHARD subroutine is used to implement user-defined hardening models, providing the ability to define custom hardening behaviors not available in the standard library. It is suitable for isotropic plasticity or combined hardening models and is called at each material calculation point. It is commonly used to involve complex stress-strain relationships or metals undergoing plastic deformation. On the other hand, the VUSDFLD subroutine is used to define field variables that can influence material behavior. It is crucial for integrating damage models into the finite element framework during simulations. This subroutine allows for predicting damage development and fracture in materials by identifying necessary information, such as stress and strain, at the beginning of each increment. Both subroutines enhance the flexibility of ABAQUS in simulating complex material behaviors and are essential for advanced finite element analyses where standard models are insufficient.

In this thesis, the damage models used are implemented through the VUSDFLD subroutine, while the hardening model is incorporated using the VUHARD subroutine. To demonstrate that these subroutines are working correctly, the Johnson-Cook plasticity and damage models, which account for stress triaxiality, strain rate, and temperature effects, are selected, as these models are also available in ABAQUS. For comparison, the IN718 material is used. The definition of plasticity and damage parameters is detailed in Chapter 3. This section presents the plasticity and damage parameters obtained for the Johnson-Cook model and describes the geometry used during code testing. A 1 mm cubic specimen is uniaxially stretched under displacement control, with symmetry boundary conditions applied on three faces. The Johnson-Cook plasticity parameters are determined using the experimental plastic data shown in Equation 2.42 and Figure 3.18. Similarly, the Johnson-Cook damage model is modeled using the average values (see Table 3.6) of the specimens shown in Figure 3.3 and Equation 2.67. The plasticity and damage models for IN718 are presented in Table 2.3 and Table 2.4. Strain rate and temperature parameters are taken from the

literature [112, 113].

Table 2.3: Johnson-Cook plasticity model parameters for IN718.

A [MPa]	B [MPa]	n	C	$\dot{\varepsilon}_0$
789	1470	0.53	0.01	0.1/0.01/0.001
θ_{trans} (K)	θ_{melt} (K)	m	χ	C_p (J/kg K)
293	1593	1.65	0.6	435

Table 2.4: Johnson-Cook damage model parameters for IN718.

D_{21}	D_{22}	D_{23}	D_{24}	D_{25}
0.0989	1.142	2.039	0.04	0.89

The effects of strain rate and temperature on plasticity and damage are examined using different $\dot{\varepsilon}_0$ values (0.1 s^{-1}, 0.01 s^{-1}, and 0.0001 s^{-1}) and initial temperatures (25°C, 100°C, and 200°C). Figure 2.12 illustrates the force-displacement behavior under various conditions for a material tested with both ABAQUS and the VUHARD subroutine. The top graph demonstrates that the plasticity behavior is accurately captured by the VUHARD subroutine, showing good agreement with ABAQUS. The middle graph presents the force-displacement curves for different reference strain rates ($\dot{\varepsilon}_0$=0.001,0.01, 0.1), where both ABAQUS and VUHARD display consistent results, indicating the effectiveness of VUHARD in modeling strain rate dependence. The bottom graph compares the curves for different temperatures (25°C, 100°C, 200°C) and reference strain rate ($\dot{\varepsilon}_0$=0.1), with VUHARD closely matching ABAQUS across all conditions. This comprehensive comparison highlights the reliability of VUHARD in simulating material plasticity under varying strain rates and temperatures, aligning well with ABAQUS simulations. Likewise, in Figure 2.13, the effects of strain rate and temperature are compared using ABAQUS and VUSDFLD. The results showed that VUSDFLD works correctly.

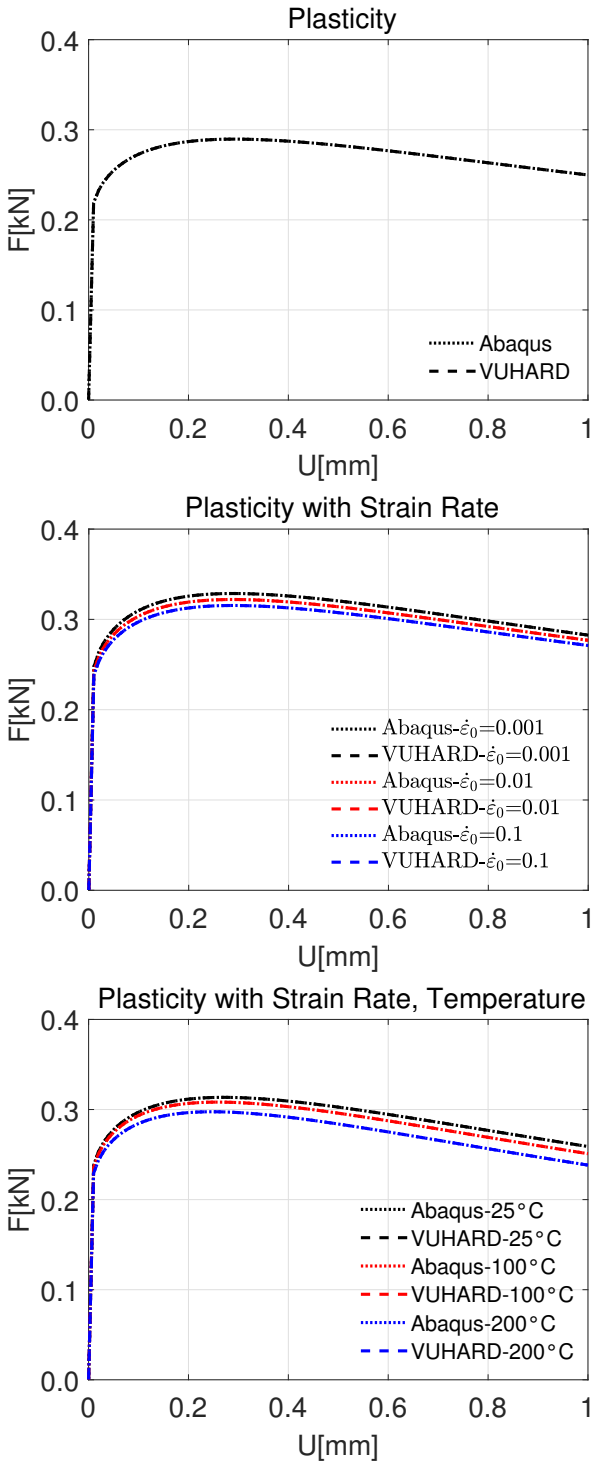

Figure 2.12: Comparison of force-displacement curves for different plasticity scenarios.

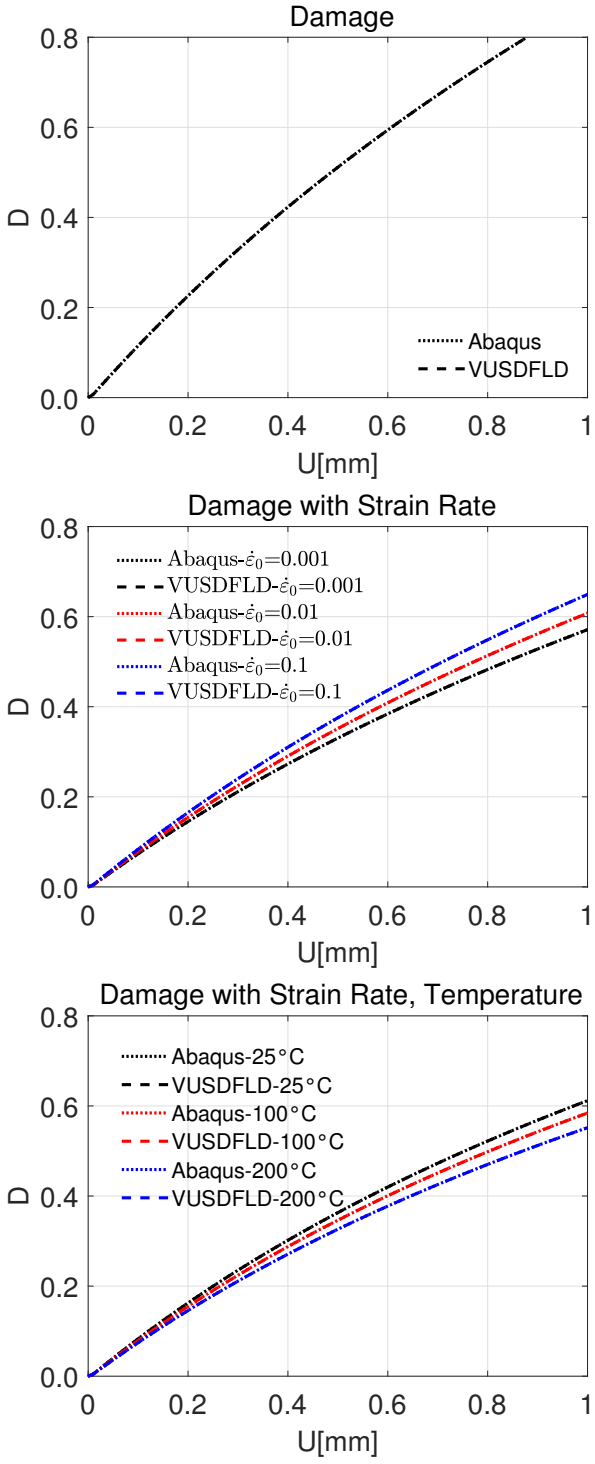

Figure 2.13: Comparison of damage-displacement curves for different damage scenarios.

CHAPTER 3

EXPERIMENTAL IDENTIFICATION AND VERIFICATION OF PLASTICITY AND DAMAGE MODELS

Identification and validation of plasticity and damage models are essential for modeling the fracture behavior of materials under various loading conditions. Experimental and numerical studies have been conducted to model flow stress and ductile fracture. This chapter focuses on the materials, experimental tests, finite element (FE) modeling, and validation of both plasticity and damage models. In the thesis, aluminum alloy 2024 annealed condition (AL2024-O) and Inconel 718 (IN718) are studied. Uniaxial tensile tests are performed on these materials, with detailed explanations provided for the test setup, post-processing procedures, and the different specimen geometries used. The plastic behavior of the materials is modeled based on the experimental force-displacement data, and damage models are calibrated using the same experimental data. Also, multi-parameter models are calculated to calibrate stress triaxiality, Lode parameter, and equivalent plastic deformation at the fracture initiation point.

3.1 Materials

The materials used in the flow forming process and tensile experiments are IN718 and AL2024-O. These materials are selected due to their excellent mechanical properties and wide industrial applications.

IN718 is first focused, as this material is a nickel-based precipitation hardenable superalloy where γ' and γ'' precipitations are nucleated after the aging treatment to have improved mechanical properties. It has good fatigue and creep strength with

high corrosion resistance, and it has been widely used in the hot sections of gas turbine engines such as turbine discs and blades. The chemical composition of the alloy is given in Table 3.1. Figure 3.1 shows the specimens used for this material.

Table 3.1: Chemical composition of IN718 [mass fraction, %].

Element	Ni	Nb	Mo	Ti	Al	Cr	Cu	Si	Fe	Mn	C
Content	54.35	4.96	2.77	0.95	0.56	18.59	0.04	0.32	16.68	0.28	0.5

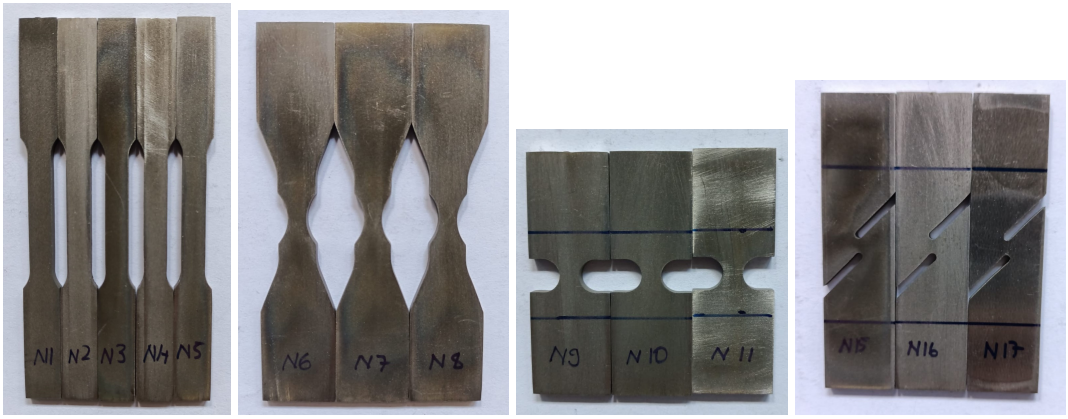

(a) ST (b) NT (c) PST (d) ISS

Figure 3.1: Experimental specimens of Inconel 718 used for tensile tests.

The second material, AL2024-O, is an aluminum alloy known for its high strength-to-weight ratio, good corrosion resistance, and excellent machinability. AL2024-O is commonly used in aerospace applications, including structural components and skin panels, due to its favorable mechanical properties and ease of fabrication. The "O" condition indicates that the alloy is in an annealed state, providing a balance of strength and ductility suitable for forming processes. The chemical composition of Al2024-O is shown in Table 3.2, and the specimens used are shown in Figure 3.2.

Table 3.2: Chemical composition of Al2024-O [mass fraction, %].

Element	Al	Cu	Mg	Fe	Si	Mn
Content	92.5	4.7	1.3	0.2	0.3	0.7

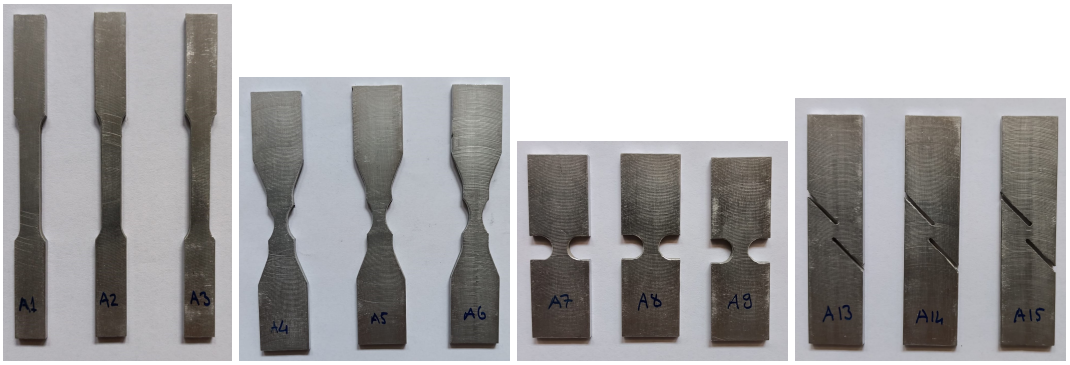

(a) ST (b) NT (c) PST (d) ISS

Figure 3.2: Experimental specimens of Al2024-O used for tensile tests.

These materials are chosen for their unique properties that make them suitable for the flow forming process and subsequent analysis of plasticity and damage behaviors. The experimental results obtained from these materials will be used to calibrate and validate the plasticity and damage models discussed in this thesis.

3.2 Uniaxial Tension Tests

Uniaxial tensile tests are performed to obtain the materials' stress-strain behavior and calibrate the plasticity and damage models using these results. This section summarizes the test procedures and results obtained from the experiments. Specimens with various stress states in different geometries cut from sheet material are produced for both materials. These tests consist of tension tests on smooth tension (ST), notched tension (NT), plane strain tension (PST), and in-plane shear (ISS) specimens. Three pieces of each specimen geometry are employed. All specimens have a thickness of 3 mm, with the geometric dimensions detailed in Figure 3.3.

Displacement measurements are obtained using 2D Digital Image Correlation (DIC), a non-contact measurement technique that calculates the deformation of a speckle pattern on the surface of the specimen. It is frequently used in tensile tests and metal forming processes [114, 115, 116, 117]. The basic process in the DIC method is comparing two images taken from the sample before and after loading. This technique enables full-field displacement measurements. The images are subjected to

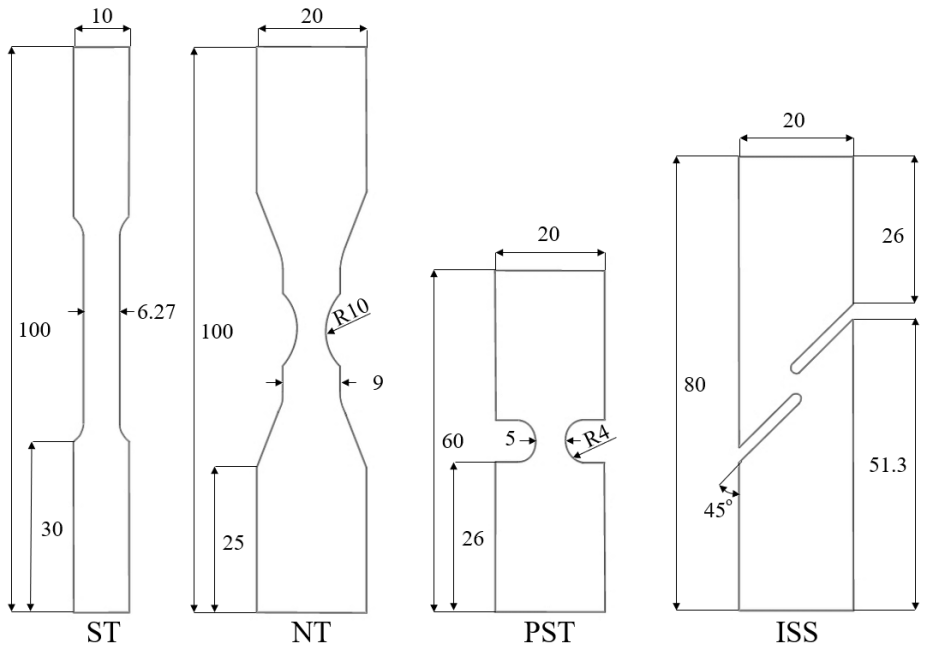

Figure 3.3: Dimensions of the Smooth Tension (ST), Notched Tension (NT), Plane Strain Tension (PST), and In-plane Shear (ISS) specimens used in the tensile tests. Dimensions are given in mm.

a correlation algorithm that tracks intensity patterns in small sections called subsets and calculates local deformations and displacements by comparing these subsets. The specimens must have a speckled structure for the subsets to calculate the change. The specimens are sprayed with white paint and then patterned with black speckles to create a speckle pattern, as shown in Figure 3.4. The speckle pattern size varies from 1 to 10 pixels (1 pixel is approximately 0.045 mm).

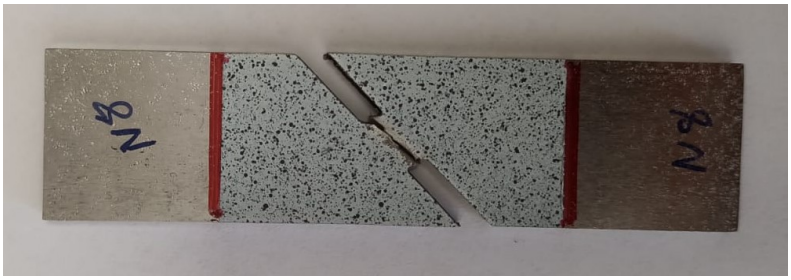

Figure 3.4: The speckle pattern of specimens

The tests are conducted using the MTS 100 kN Tensile–Bending Fatigue/Static testing

machine, as shown in Figure 3.5. Additionally, additional lighting is used so the lenses can see the sample more clearly. During the test, the specimens are clamped at both ends using wedge grips with 5 MPa pressure at a distance of 20 mm from the measurement section. The quasi-static tensile tests are displacement-controlled and perform at a 1 mm/min displacement rate. GOM Aramis 4M (rev03) high-speed camera and Titanar 100 mm lenses capture images at three frames per second (3 Hz). These images are used to determine displacement changes with the DIC method. The camera is positioned at 785 mm to take photos. The DIC setup provider gives this distance in a table for the camera and lens we used.

Figure 3.5: Experimental setup: Uniaxial tension test system and optical equipment for DIC measurement.

NCORR is an open-source MATLAB software for 2D digital image correlation (DIC) and is used to measure surface deformations and stresses of materials [118]. NCORR is run in the MATLAB environment, and they first load the reference and post-deformation images. Next, they select the region of interest (ROI), usually the specimen geometry containing the points taken from displacement data, set the subset and step sizes, and start to calculate the deformation between two images. NCORR visualizes the results via the graphical user interface (GUI), and the obtained data can be exported as data and used in subsequent calculations.

The subset radius is selected as 30 pixels, and the step size is 2 pixels. Step size is referred to as subset spacing in NCORR software. As suggested in the manual of NCORR software, the subset radius is selected to include at least 2-3 black dots in the speckle pattern. We ensured the displacement solution did not change with different subset sizes and step size values (see Figure 3.6). Less than 0.5% difference is observed between the cases shown below. In addition, DIC analysis calculates the displacement in pixels, but the value in mm is used. Conversion from pixel to mm is required, but this conversion may also change as the camera's location changes slightly for each geometry during the tests. For this, the width of the specimen is used as the reference length to determine the pixel-to-mm conversion. It is measured with a digital caliper, with a rated accuracy of 0.02 mm. Pixel to mm conversion is calculated as 0.0452, 0.0456, 0.0451, and 0.0454 for ST, NT, PST, and ISS specimens, respectively. Thus, the maximum difference is about 1% between measurements.

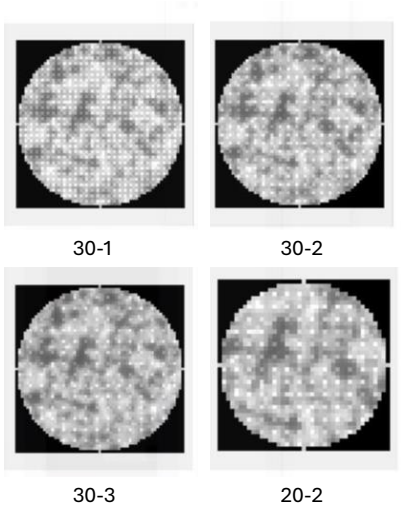

(a) Subset size variations

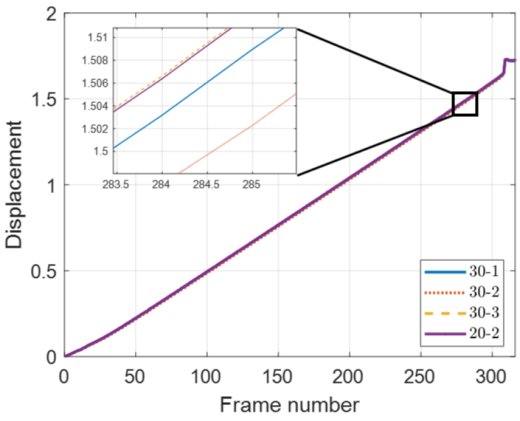

(b) Displacement curves for different subset and step sizes across frame numbers

Figure 3.6: Change in displacement measurement from DIC with different subset size and step size.

Displacements at all solution points are calculated using NCORR. The displacements for the specimens are determined by the difference between two points positioned vertically to the center of the specimen. Figure 3.7 and Figure 3.8 depict the dimensions and displacement measurement points for different specimen geometries. In Figure

3.7, the gauge lengths of IN718 for the ST, NT, PST, and ISS specimens are shown as 40 mm, 50 mm, 8.1 mm, and 28 mm, respectively. In Figure 3.8, the corresponding gauge lengths of Al2024-O for the same specimen types are indicated as 39.8 mm, 48.66 mm, 7.6 mm, and 27.6 mm, respectively. The red dots on the specimens mark the points between displacement measurements, providing critical data for evaluating the material's response to loading.

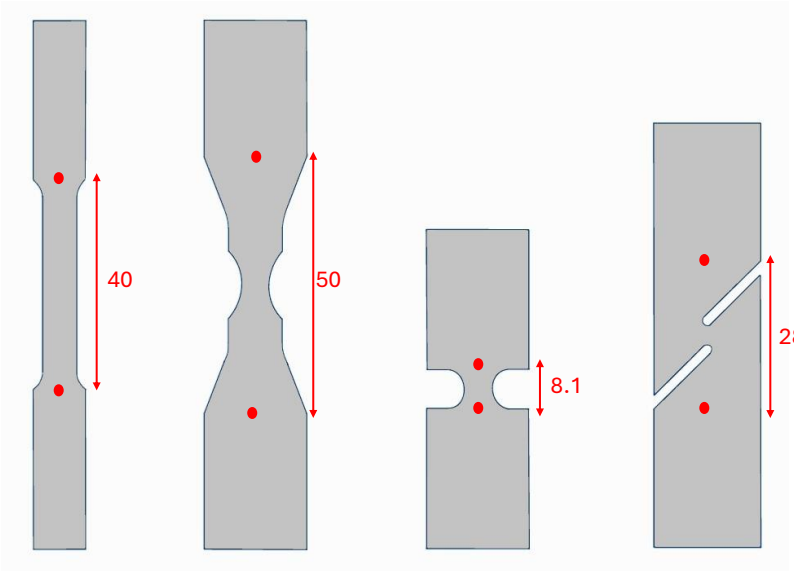

Figure 3.7: Gauge lengths and displacement measurement points for different specimen geometries (ST, NT, PST, ISS) for Inconel 718.

The force data from the testing machine and the displacement data set calculated by DIC are synchronized. For this, it is essential to know the rate of high-speed cameras and machines. The results are presented in force-displacement curves for each specimen geometry, up to and slightly beyond the fracture point. Data could not be obtained for one of the NT samples for Al2024-O and one of the ST samples for IN718 due to some problems encountered during the tests. Multiple tests are performed for each geometry, and some differences in the results are observed. These differences may be due to differences in sample fabrication or differences in the intrinsic microstructure of the material.

Figure 3.9 presents the experimental force-displacement curves for IN718 specimens. The graphs illustrate the performance of different specimen geometries under tensile testing: (a) Specimens N1 and N2 (ST), (b) Specimens N6, N7, and N8 (NT), (c)

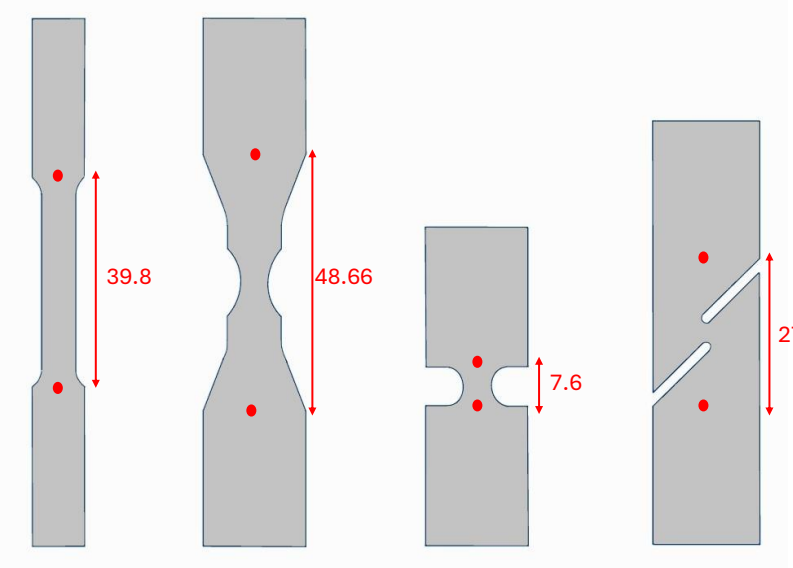

Figure 3.8: Gauge lengths and displacement measurement points for different specimen geometries (ST, NT, PST, ISS) for Al2024-O.

Specimens N9, N10, and N11 (PST), and (d) Specimens N15, N16, and N17 (ISS). Figure 3.10 shows the experimental force-displacement curves for Al2024-O specimens. The graphs illustrate the behavior of different specimen geometries under tensile testing: (a) Specimens A1, A2, and A3 for ST, (b) Specimens A5 and A6 for NT, (c) Specimens A7, A8, and A9 for PST, and (d) Specimens A13, A14, and A15 for ISS. The curves depict the relationship between the applied force and the resulting displacement, providing insights into the material's mechanical behavior and fracture characteristics for each specimen configuration.

3.3 Finite Element (FE) Modeling

Computational methods are employed in engineering evaluations to ensure efficiency in terms of cost and time. One of these methods, the finite element method (FEM), simplifies the analysis by dividing a component into smaller parts. It is crucial to optimize the number of elements to obtain accurate results. Although using more elements increases the details, it may lead to a loss of time and increase computational cost. Displacement-controlled explicit finite element (FE) simulations are performed to calibrate and validate plasticity and damage model parameters. This section em-

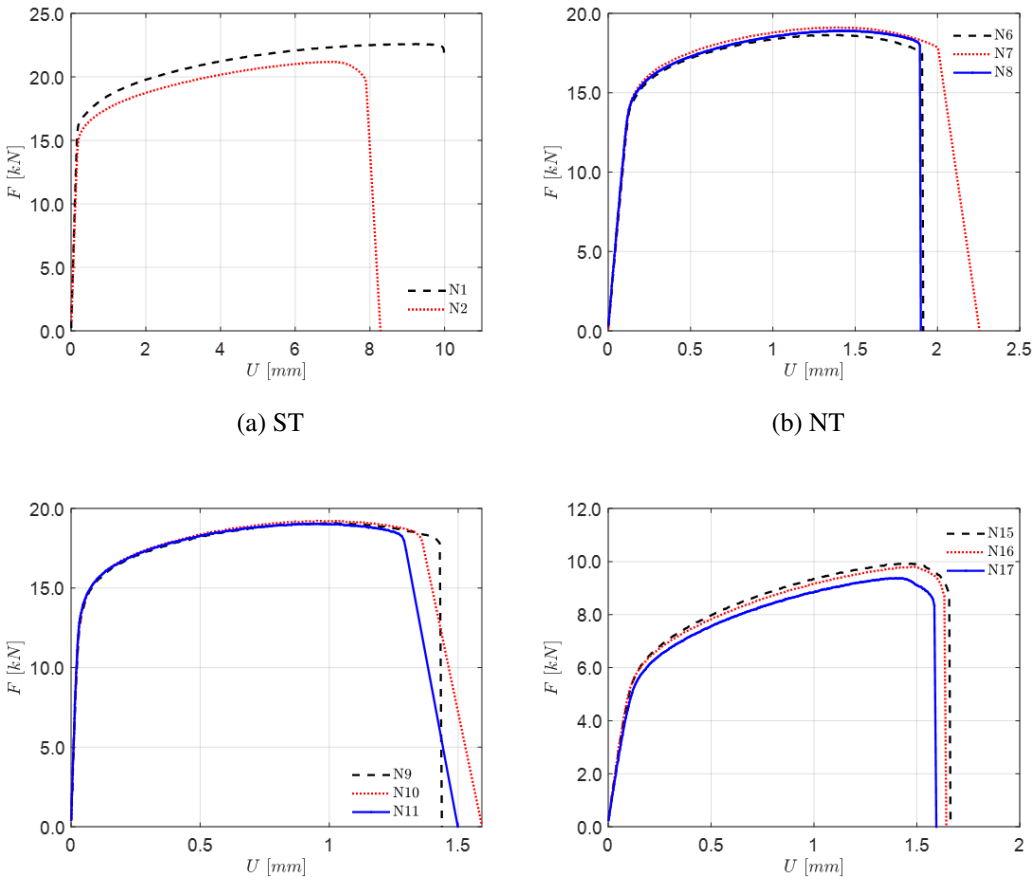

(a) ST

(b) NT

(c) PST

(d) ISS

Figure 3.9: Experimental force-displacement curves for IN718.

ploys the von Mises yield function for IN718, utilizing the plasticity parameters provided in Table 3.3. The parameter set used in the results obtained in the FE modeling section is given in detail in the following section.

In FE analysis, the upper and lower parts clamped in the testing machine are modeled as rigid sections. The painted part from which the images are taken is modeled as deformable, and these two parts are connected with tie constraint (shown in Figure 3.13). A quarter model reduces the computational cost since geometric symmetry exists in the ST, NT, and PST specimens. As shown in Figure 3.11, the results obtained from the whole and quarter models are similar. However, the whole model is used since the ISS specimen has no symmetry plane, like other specimen.

In the study, the codes are implemented for Abaqus/Explicit, and to ensure that the

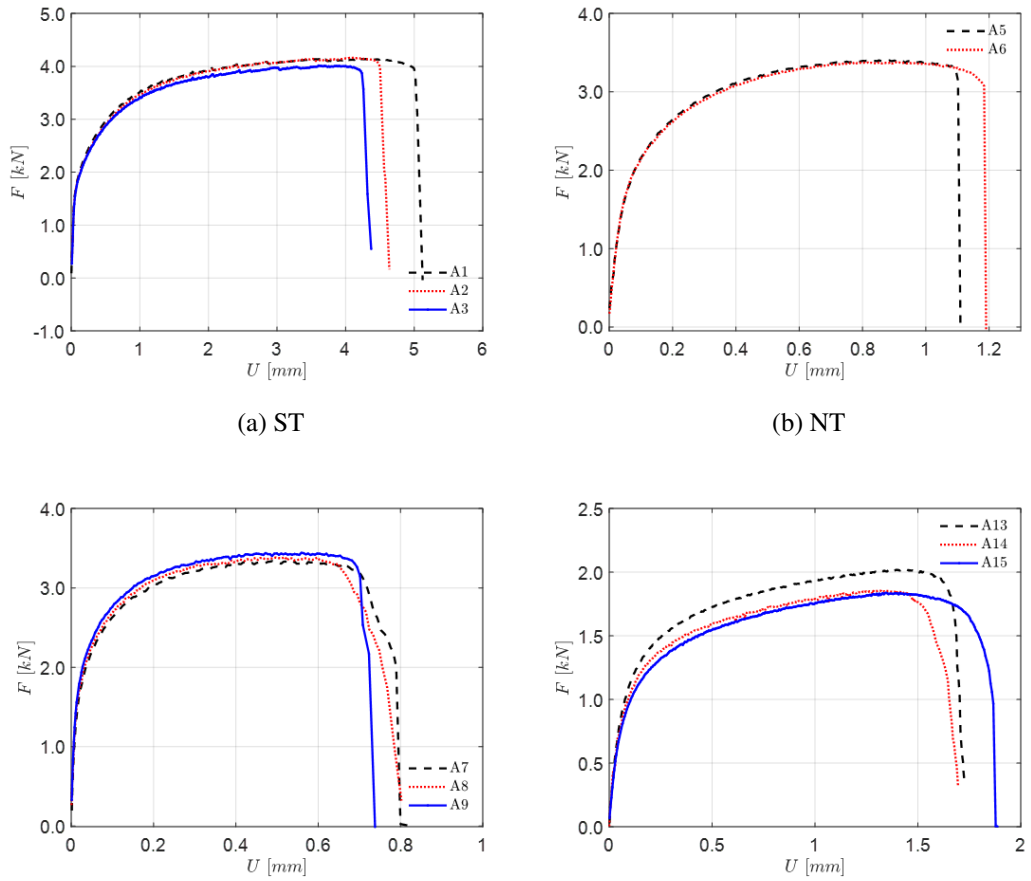

(a) ST

(b) NT

(c) PST

(d) ISS

Figure 3.10: Experimental force-displacement curves for Al2024-O.

explicit finite element model of tensile tests is working correctly, Abaqus/Standard analyses are also taken, and the explicit-implicit results are compared. For this purpose, UHARD and VUHARD are employed and compared using the plasticity parameters for IN718. As shown in Figure 3.12, the results of implicit and explicit solutions are similar. The analysis is continued with an explicit solver to apply the element deletion method to represent material fracture. Although element deletion is available in the implicit solver, it is not preferred due to its increased computational time and complexity.

The boundary conditions are applied to simulate the experimental setup accurately, ensuring that the constraints and load applications reflect real-world scenarios. A displacement-controlled boundary condition is applied from the reference point on

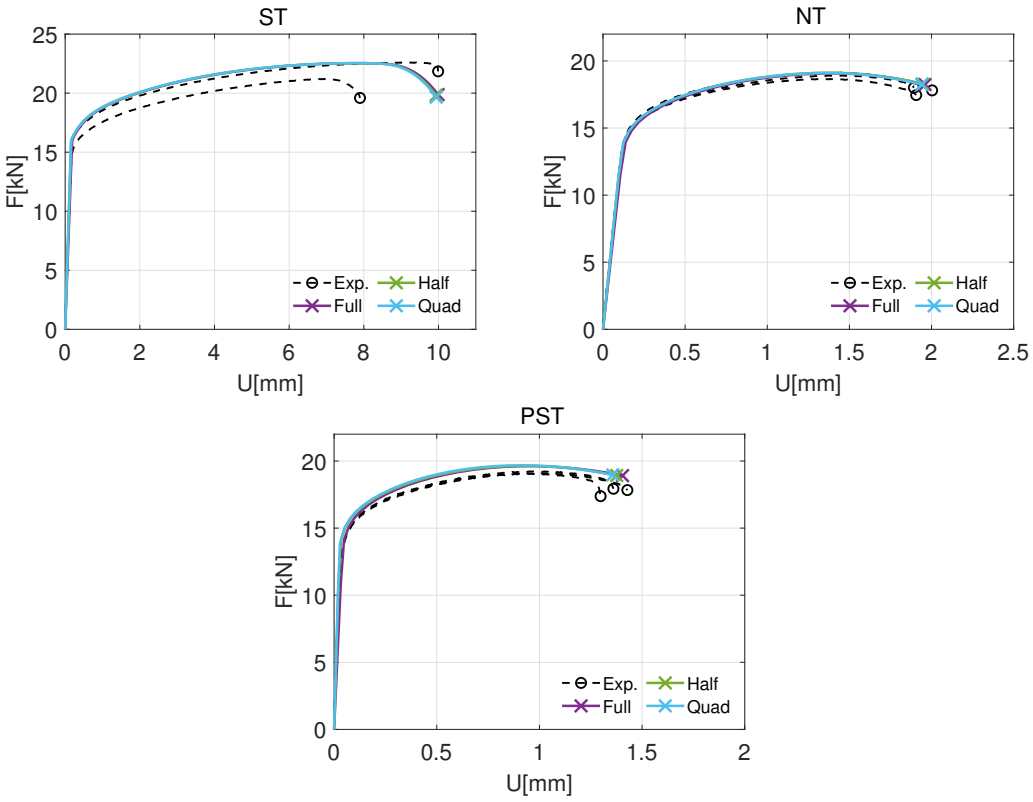

Figure 3.11: The experimental results are compared with simulations using different part models: Half, Full, and Quarter.

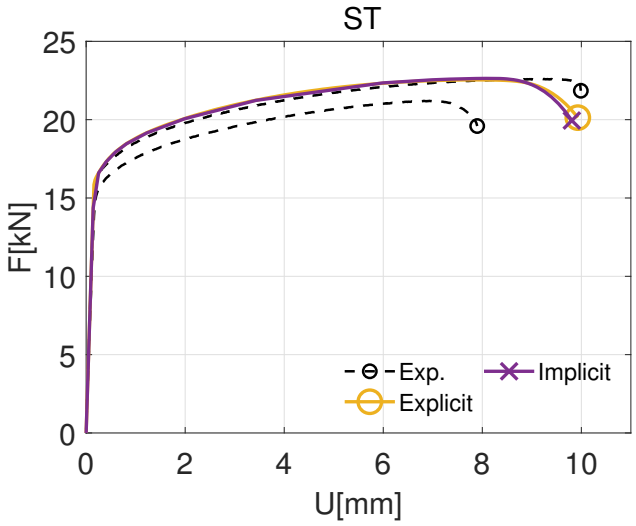

Figure 3.12: Force-displacement curve for ST specimen geometry. The experimental results are compared with simulation results using implicit and explicit methods.

the rigid part, as shown in Figure 3.13. Displacement values vary depending on the species. Additionally, the amplitude value must be given in explicit analyses. The analyses are modeled as smooth step functions throughout 1 second in quasi-static conditions. Since the three specimens are modeled symmetrically, the symmetry boundary condition is applied to the symmetry corrections. The rigid part at the bottom of the ISS specimen is kept from the reference point. Rigid bodies are used to represent the fixtures and grips, while deformable bodies model the actual specimens, allowing for precise stress and strain analysis.

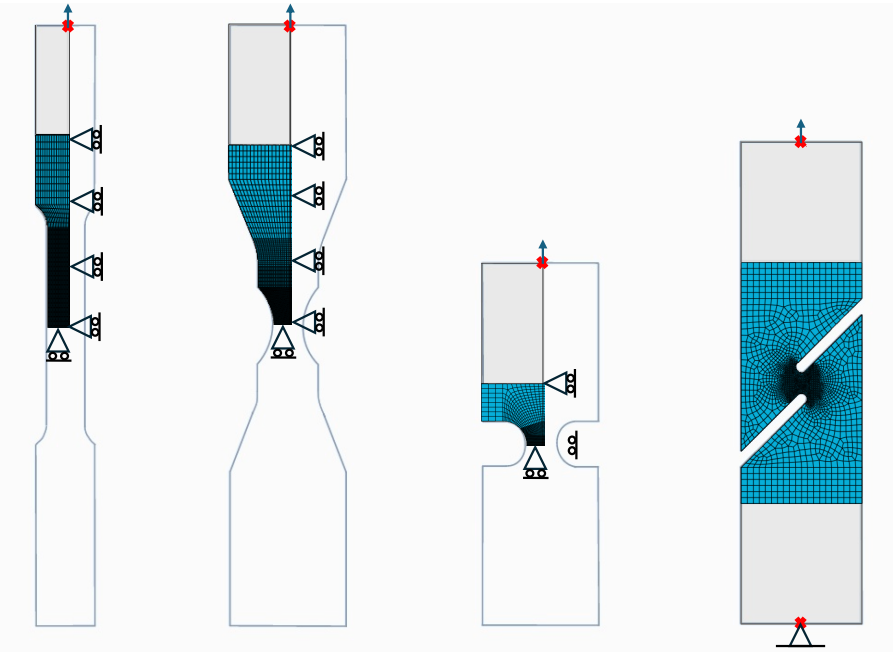

Figure 3.13: Detailed illustration of boundary conditions, rigid and deformable bodies for different specimen geometries used in the study.

Since mesh and time dependency are present in the explicit model, mesh, and mass scaling studies must be done. Since it is impractical to run a quasi-static analysis on a real-time scale, methods such as increasing the loading rate and scaling the material density can reduce the simulation's running time. Density scaling is called mass scaling and is generally preferred because it does not affect the strain rate. If the ratio of kinetic energy to internal energy is below 10%, it can be concluded that the dynamic effects in the model are negligible, and the solutions are stable. It is studied with six different time increments for mass scaling, and the results are shown in Figure 3.14.

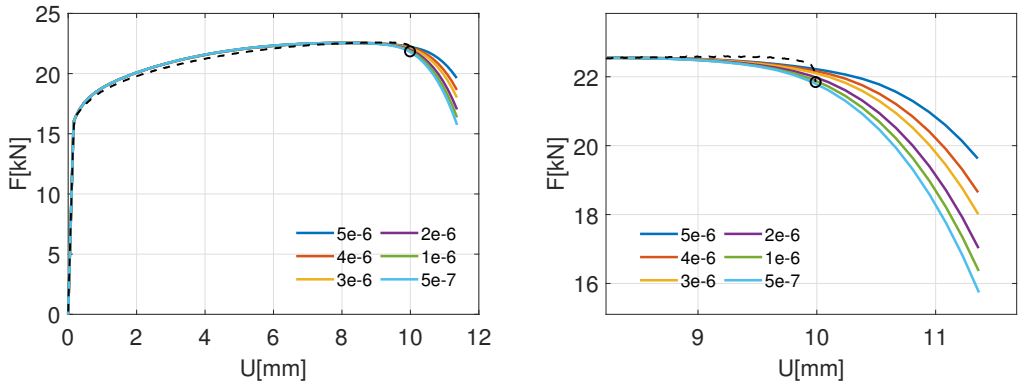

Figure 3.14: Force-displacement curves for different mass scaling factors, showing the effects of various time increments (5e-6, 4e-6, 3e-6, 2e-6, 1e-6, and 5e-7) on the results. The right panel zooms in on the final part of the curves to highlight differences in behavior near the end of the displacement range.

The force-displacement curves are pretty consistent over most of the displacement range; this indicates that mass scaling increases have a small impact on the overall response. However, the deviation becomes more evident as the displacement increases significantly above 9 mm. This result shows that smaller mass scaling time increments tend to give more accurate results in the higher displacement range. Considering these observations, a convergence is observed at the selected mass scaling values of 1e-6 and 5e-7. Considering the computational time, the 1e-6 time increment value is chosen as the appropriate mass scaling.

Similar to a mass scaling study, a mesh study must be conducted to optimize the solution time and results. Generally, for the tensile test meshes, reduced integration eight-node linear brick elements (C3D8R) are used, and the element deletion method is applied to represent material fracture. The mesh is designed so that the elements near the center of the sample have the same size in the in-plane directions and half the size of the elements in the tension direction. The mesh configurations are detailed in Figure 3.15, with refined mesh regions highlighted in the enlarged sections to capture the critical stress and strain gradients accurately. Specimens are conducted with five different mesh configurations using element sizes of 0.5, 0.4, 0.3, 0.2, and 0.1 in the thickness direction, respectively.

Five different meshes are evaluated in the mesh study. The appropriate mesh is de-

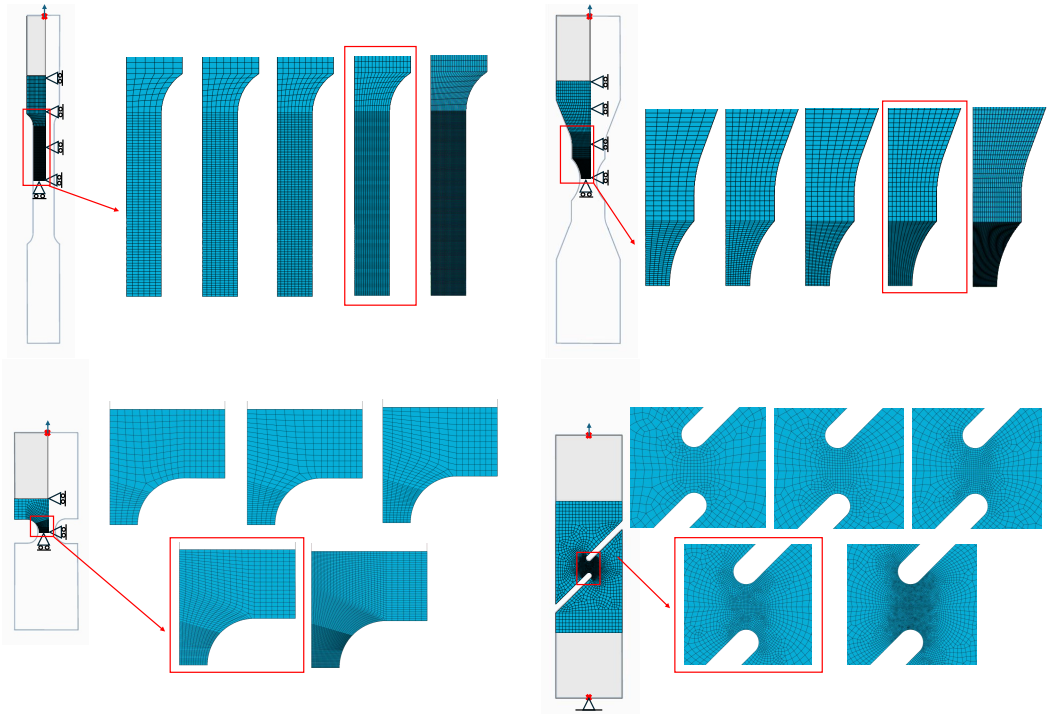

Figure 3.15: Mesh configurations for different specimen geometries used in the study.

cided based on the force-displacement response, relative elongation-equivalent plastic strain, and computational time. Force-displacement curves for different specimen geometries (ST, NT, PST, and ISS) show a strong correlation between experimental results and simulations using varying mesh sizes (see Figure 3.16). For all sample types, simulations with a mesh size of 0.1 to 0.3 generally best fit experimental data, especially in critical regions where the material fails. For example, in the ST, mesh sizes of 0.1 and 0.2 closely match the experimental data, especially in the post-yield region. In contrast, in the NT, mesh sizes of 0.3 and 0.4 show slight deviations initially but converge well at higher displacements. The PST simulation with a mesh size of 0.3 closely agrees with the experimental curve, especially when the force begins to decrease. Similarly, for the ISS, mesh sizes of 0.3 and 0.4 effectively capture the shear behavior. Finer meshes generally show increased accuracy but increased computational cost. In particular, in the ST and NT, the differences between the 0.1 and 0.2 mesh sizes are minimal, and considering the computational time, the element with 0.2 is chosen as the most suitable mesh layout.

For the ST, NT, and PST specimens, the element size in the gauge length is 0.2 mm,

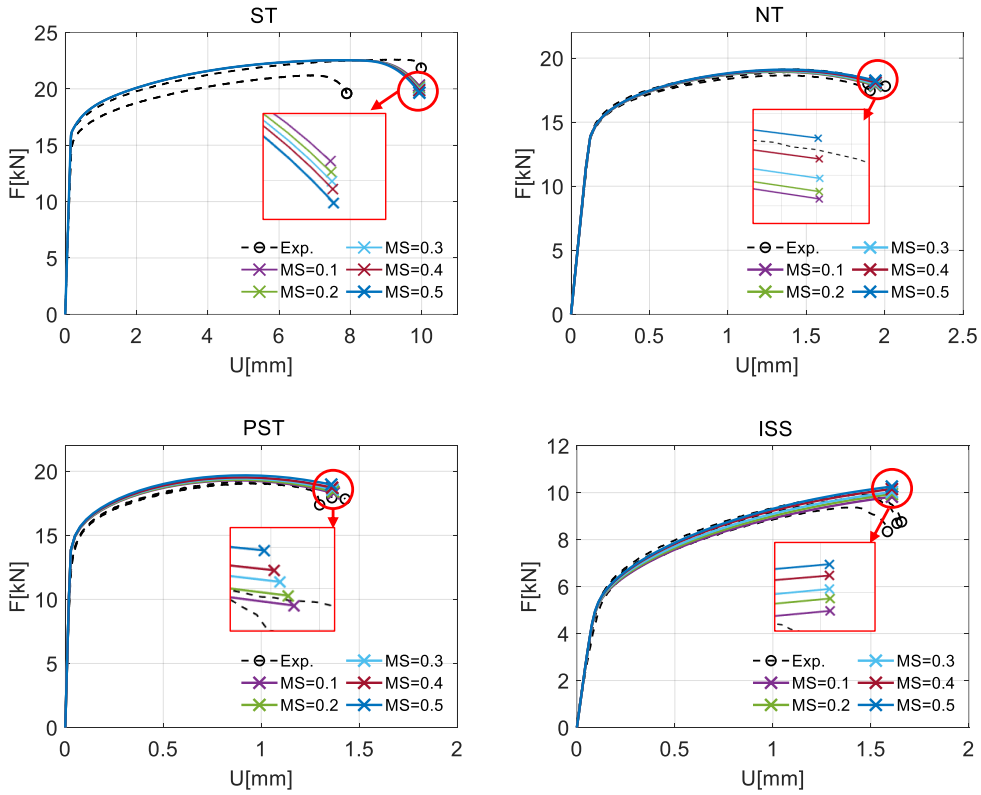

Figure 3.16: Mesh study for tensile test specimens (ST, NT, PST, ISS). MS is mesh size.

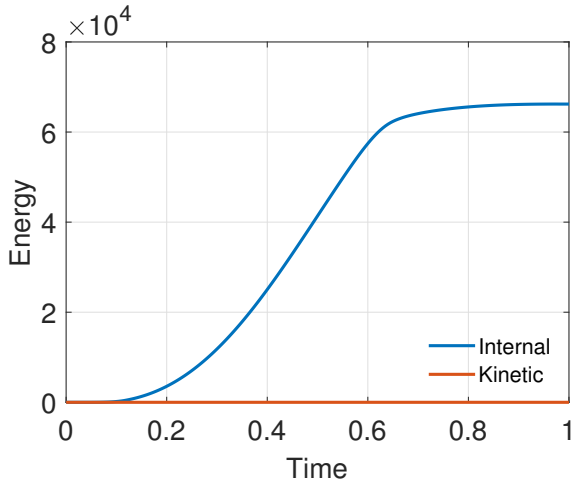

Figure 3.17: Energy-time plot showing the variation of internal and kinetic energy during the simulation.

and the element size of the edge of the tensile direction is 0.1 mm to ensure controlled extension of elements. For the ISS specimen, the element size in the thickness direction is 0.2 mm, and it is 0.1 mm in the gauge region. The selected meshes are highlighted within a red box in Figure 3.15.

The analysis of the energy results obtained for the selected mass scaling and mesh shows that it works quasi-statically and has no dynamic effect. A comparison of internal and kinetic energy is made in Figure 3.17. The internal energy increases steadily, indicating plastic deformation, while the kinetic energy remains negligible, confirming the quasi-static nature of the simulation.

3.4 Identification and Verification of Plasticity Models

A trial-and-error method is used to model plasticity and damage. The main idea is to model the material parameters by comparing the load-displacement response of experiments and numerical simulations. Since this study uses an uncoupled approach to model ductile fracture, hardening parameters can be calibrated with experimental data independently of damage parameters. For plasticity modeling, experimental plasticity data are initially required. This data is obtained by processing the experimental force-displacement data to derive engineering and true stress-strain curves and then taking the plasticity part of the true stress-strain data. Several formulas are used to transition between these values. Engineering stress and strain are calculated from the specimen dimensions and the load and displacement data from the experiments. The formulas for engineering stress-strain are provided below:

$$\begin{aligned} \epsilon_E &= \frac{\Delta l}{l_0} \\ \sigma_E &= \frac{F}{A_0} \end{aligned} \tag{3.1}$$

where Δl is the experimental displacement, l_o is the length between two displacement points (gauge length), F is the recorded load, and A_0 is the initial area of the gauge section.

Similarly, the transition from engineering stress-strain to true stress-strain can be

made using the following formulas. The formulas are as follows:

$$\begin{aligned} \varepsilon_T &= \ln\left(1+\varepsilon_E\right) \\ \sigma_T &= \sigma_E\left(1+\varepsilon_E\right) \end{aligned} \tag{3.2}$$

where ε_T is the true stress, ε_E is the engineering stress, σ_T is the true strain, and ε_E is the engineering strain.

The true strain-stress data obtained consists of two regions: elastic and plastic. The plastic part required for hardening is the part from the yield stress to the ultimate stress value in the data. This part is where the hardening rules are fitted. This process is done for both materials. However, since the yield functions required for these two materials differ, the plasticity modeling of each material is discussed separately.

3.4.1 IN718

The stress-strain curves are obtained from the ST specimen up to the necking point using the experimental force-displacement data. The stress-strain curves used for determining the hardening parameters of the material are shown in Figure 3.18.

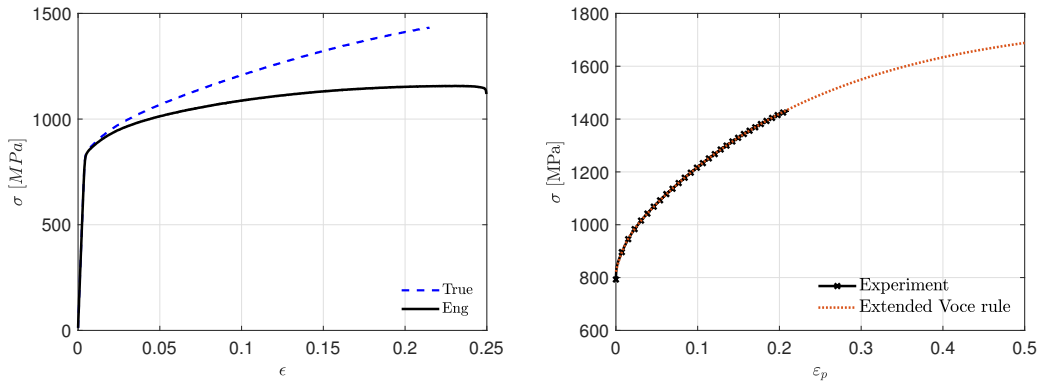

(a) (b)

Figure 3.18: (a) True and engineering stress-strain curves for IN718. (b) Comparison of experimental stress-strain data with the extended Voce rule.

Based on the obtained plastic data and the extended Voce rule given in Equation 2.40, the hardening parameters are determined with the MATLAB curve fitting tool. The

Voce rule extended with experimental data is fitted quite successfully with the determined hardening parameters. These parameters are vital for precise finite element simulations and are listed in Table 3.3.

Table 3.3: Plasticity model parameters for IN718.

σ_0[MPa]	q_1 [MPa]	c_1	b_1	q_2 [MPa]	c_2	b_2
789	499.6	0.1731	106.7	499.6	1.761	4.351
C	$\dot{\varepsilon}_0$	θ_{trans} (K)	θ_{melt} (K)	m	χ	C_p (J/kg K)
0.01	1	293	1593	1.65	0.6	435

It should be noted that only the yield stress and hardening parameters are calibrated using tensile tests; the parameters for the strain rate and temperature-dependent parts are taken from Hao et al. [112]. Although the inelastic heat fraction, χ, is generally considered 0.9, this value has been found to cause excessive thermal softening in quasi-static tensile simulations compared to tensile tests. As discussed in [119, 120], χ = 0.9 is not representative of experimental results and varies between 0.55 and 0.8 for different metals. This study adopts the value χ = 0.6, which fits our experimental results.

3.4.2 Al2024-O

The same procedure as in IN718 is performed to obtain plastic stress-strain data. Using Equations 3.1 and 3.2, the true and engineering stress-strain graph for Al2024-O, as shown in Figure 3.19a, is obtained. Unlike IN718, hardening behavior is modeled with the combination of the Voce (Equation 2.39) and Power (Equation 2.37) rule. The stress-strain curves used for determining the hardening parameters of the material are shown in Figure 3.19.

The plasticity model, initially modeled with the smooth tension specimen using the von Mises yield function, could not fit the hardening behavior of the other three specimens. According to the literature, stress triaxiality and Lode parameters are needed to model the plastic behavior of some materials. For this reason, the Bai-Wierzbicki (BW, [87]) yield function is used instead of von Mises for Al2024-O material. An

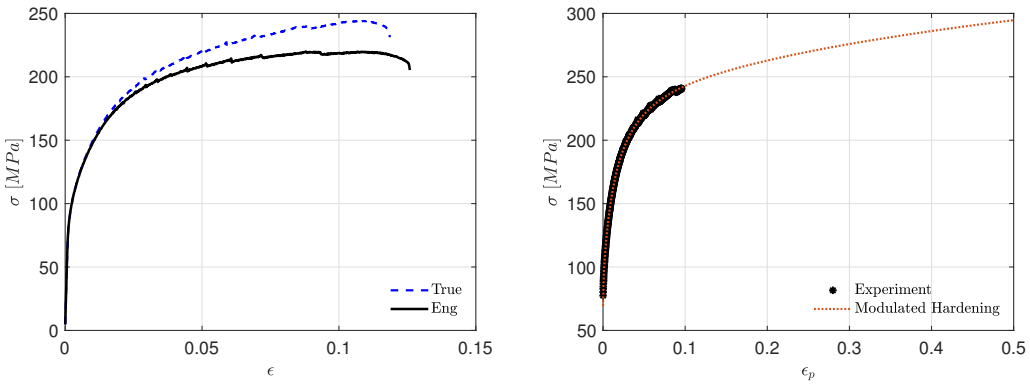

(a) (b)

Figure 3.19: (a) True and engineering stress-strain curves for Al2024-O. (b) Comparison of experimental stress-strain data with the modulated hardening rule.

additional six parameters are added to the plasticity model using this yield function. As shown in Equations 2.25, 2.26, and 2.27, the σ_y part is modeled with ST specimen as shown in Figure 3.19b. The triaxiality terms η_0 and c_η are determined using the NT and PST specimens; the Lode parameters c_s and m are found using the PST and ISS specimens. First, η_0 is taken as 1/3, frequently used as the cut-off value in the literature. However, since the part that needs to be corrected in the NT and PST is larger than the examples in the literature, η_0 is tested with different values and determined to be 0.22 to enhance the effect of the triaxiality correction. There are also studies in the literature that use a reference triaxiality value different from 1/3. Having η_0 at a value different from 1/3 resulted in a minor triaxiality effect in the ST specimen. However, this small difference is acceptable for better fitting the other three specimens as it remained within the experimental data range. Among the other two parameters, c_t is taken as one because it is generally used as 1 in the literature, and c_c is taken as one because it does not have a compression test. The parameters found for the plasticity model are given in Table 3.4.

Force-displacement curves for different geometries (ST, NT, PST, and ISS) show the comparison between experimental results and simulations using both uncorrected (wo-corr) and corrected (w-corr) models in the Figure 3.20. For all specimen types, simulations with correction (w-corr) provide closer agreement with experimental data,

Table 3.4: Plasticity model parameters for Al2024-O.

σ_0[MPa]	q_1 [MPa]	b_1	q_2 [MPa]	b_2	K[MPa]	n
77	60.19	37.59	45.12	116	1613	0.3047
α	c_η	η_0	c_t	c_c	c_s	m
0.1	0.4	0.22	1	1	0.866	20

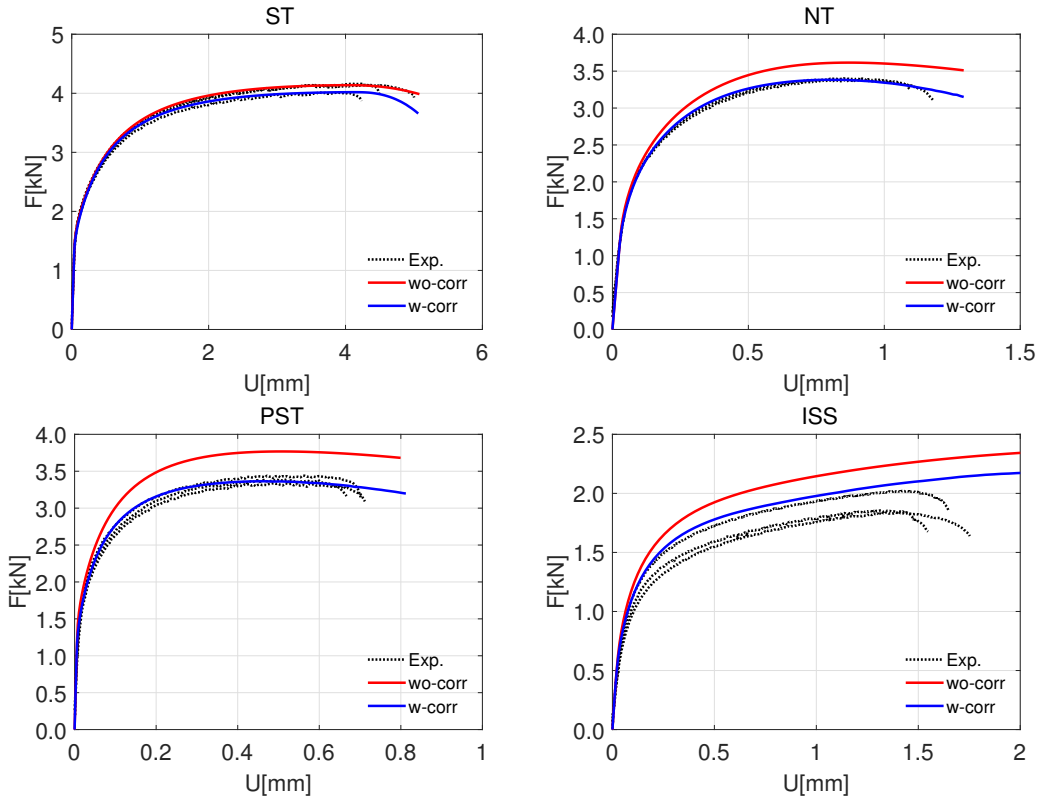

Figure 3.20: Force-displacement curves for different specimen geometries, comparing experimental results with simulations using models without correction (wo-corr) and with correction (w-corr)

especially in the initial elastic region and the early stages of plastic deformation. However, as displacement increases, uncorrected simulations (wo-corr) tend to overestimate the required force compared to experimental data, as shown by the red curves above the experimental curves. Corrected models (w-corr), represented by blue curves, show better agreement with experimental results in all geometries, emphasizing the importance of the BW yield function in models to capture material

behavior in different stress states accurately. This effect is most evident in the PST and ISS, where corrections significantly increase the accuracy of the simulations.

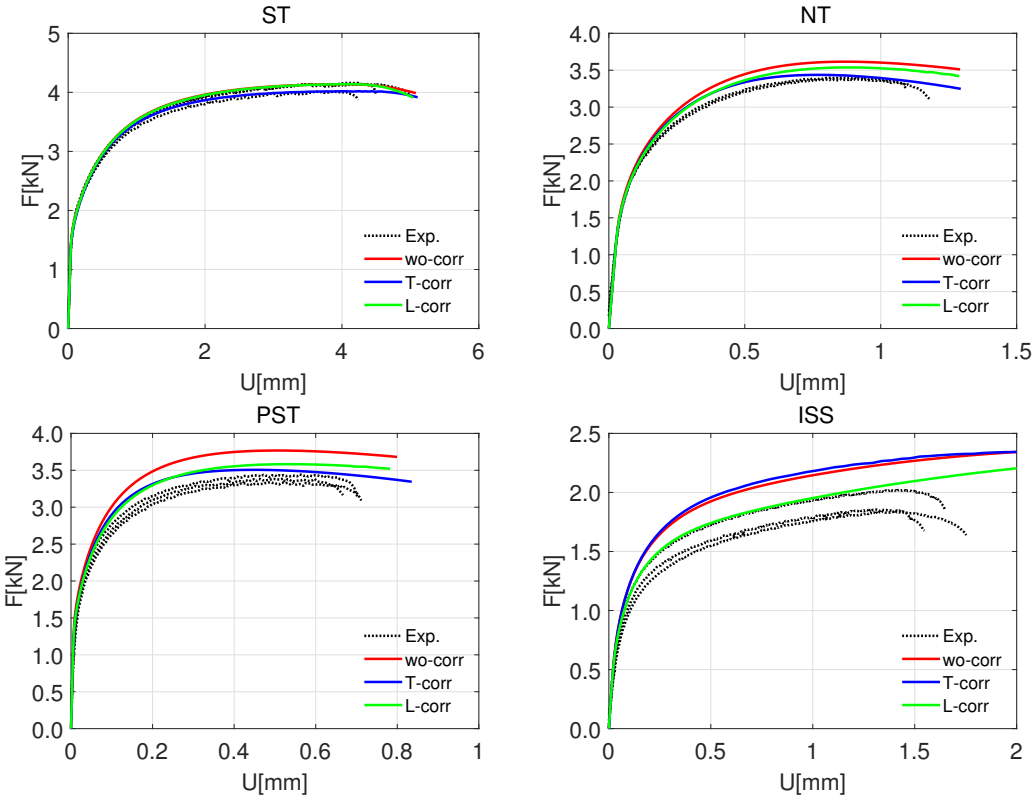

Figure 3.21: Force-displacement curves of Al2024-O for different specimen geometries (ST, NT, PST, and ISS), showing comparison of experimental results (Exp.) alongside simulations using models without correction (wo-corr), with stress triaxiality correction (T-corr), and with Lode parameter correction (L-corr).

In Figure 3.21, the effect of T and L corrections on hardening is shown with green (L-correction) and blue (T-correction) curves. It is seen that the Lode parameter in ST does not create any change in hardening because its value is 1. It is seen that the NT specimen triaxiality has a more significant effect than the Lode parameter, and in PST, the effect of both parameters is equal. Since stress triaxiality is close to zero in the ISS specimen, triaxiality correction does not have much of an effect on hardening, whereas, in this shear-dominant specimen, the Lode parameter alone can make the entire correction.

3.5 Identification and Verification of Damage Models

A hybrid experimental/numerical approach ensures accuracy and reliability in calibrating damage models (see [121]). The fracture point and, therefore, the failure strain have been determined from experiments. However, the accumulation of damage until fracture, average stress triaxiality, and Lode parameter are calculated using finite element simulations.

3.5.1 Single Parameter Damage Criteria

Single-parameter damage parameters are calibrated using the ST specimen, similar to the plasticity model. Running several explicit Finite Element (FE) analyses using the ST specimen for each damage model is prescribed. The damage accumulation rule is applied to all models using the user-defined subroutine (VUSDFLD). Subsequently, the critical value is subtracted from the experimentally observed failure point derived from the FE analysis results. After determining the critical damage parameters (C_i), the damage accumulation rule is normalized, and its accuracy is checked using the force-displacement curve of the ST specimen. In this step, the propagation of the crack is also examined by opening the element in deletion. Since the failure point is single, all models are broken at the same point, as seen in Figure 3.22. Table 3.5 presents the critical damage values determined for each criterion.

Table 3.5: Damage parameters of criteria for IN718.

Ayada (C_1)	Ayada-m (C_2)	Brozzo (C_3)	KH (C_4)	LR (C_5)
0.240	0.449	0.657	3.1.421	615.327
MC (C_6)	OH (C_7)	RT (C_9)	CL (C_9)	Freudenthal (C_{10})
1.483	0.656	1.118	978.061	924.863

Specimens such as notched tensile (NT), plane strain tensile (PST), and in-plane shear (ISS) are used along with the ST specimen to provide a comprehensive understanding of the material's behavior. The ability of both single- and multiple-parameter models to predict fracture is evaluated over these four different specimen geometries.

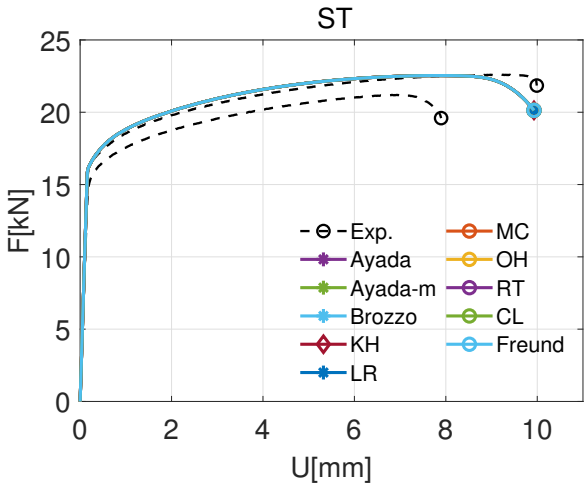

Figure 3.22: Comparison of force-displacement curves using different damage criteria (Ayada, Ayada-m, Brozzo, KH, Le-Roy, McClintock (MC), Oh (OH), Rice-Trace (RT), Cockcroft-Latham (CL), and Freudenthal) against experimental results for ST specimen.

This comprehensive evaluation is crucial to ensure the models can accurately capture material behavior in various stress states.

Since single-parameter models are calibrated only with ST, their ability to predict fracture at different triaxiality ranges is tested using three other specimens. All these single-parameter models predicted a break at the same point in the ST. However, there are differences in the fracture estimates in the other three specimens. The obtained force-displacement results are given as follows in Figures 3.23, 3.24 and 3.25. The crack initiation points are presented zoomed in since the results are close to each other, especially in NT and PST.

Since it is difficult to interpret the results in these graphs, bar charts compare them relatively with the experimental results. Figure 3.26 shows experimental and numerical fracture-initiation displacement comparisons for NT, PST, and ISS specimens. Red bars represent experimental fracture displacements in these figures, while blue bars show predictions from various damage models. In Fig. 3.27, the fracture prediction performance based on the error analysis is illustrated, and the graph shows the individual error values for each sample type (NT blue, PST yellow, and ISS green) and the total error value (red line) for each damage model. The error is calculated

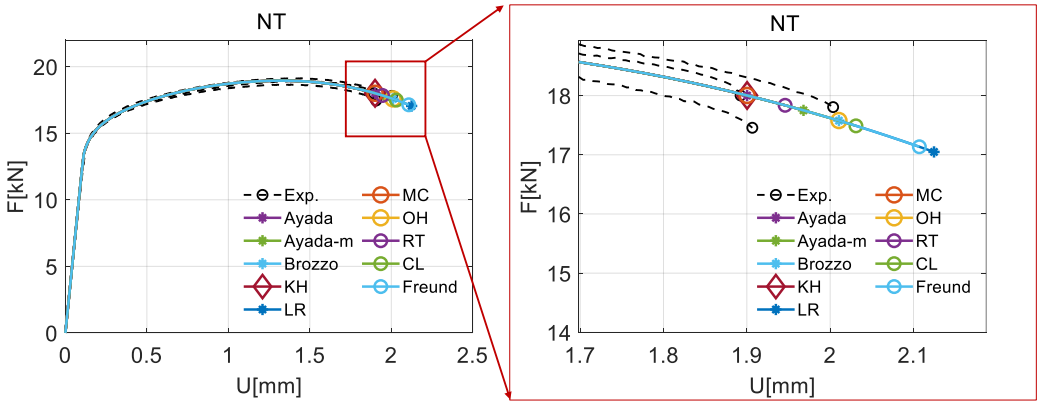

Figure 3.23: Force-displacement curves for NT specimen geometry, displaying experimental results compared with multiple damage criteria models (MC, OH, Ayada, RT, Brozzo, CL, KH, LR, Freund). The inset zooms into the region of significant deviation.

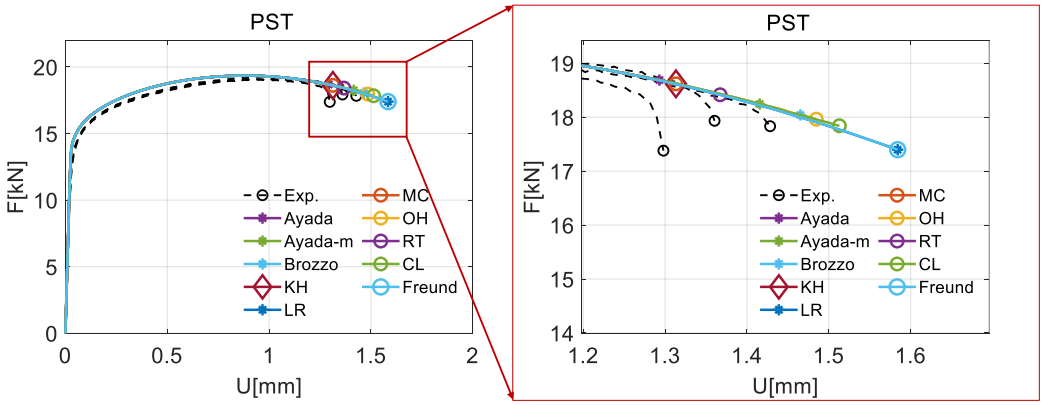

Figure 3.24: Force-displacement curves for PST specimen geometry, displaying experimental results compared with multiple damage criteria models (MC, OH, Ayada, RT, Brozzo, CL, KH, LR, Freund). The inset zooms into the region of significant deviation.

by determining the difference between the average fracture displacements observed in the experiments and those predicted by the damage models. This difference is then expressed as a percentage. The error calculation is conducted separately for each specimen. The total error represents the sum of the errors for all three specimens.

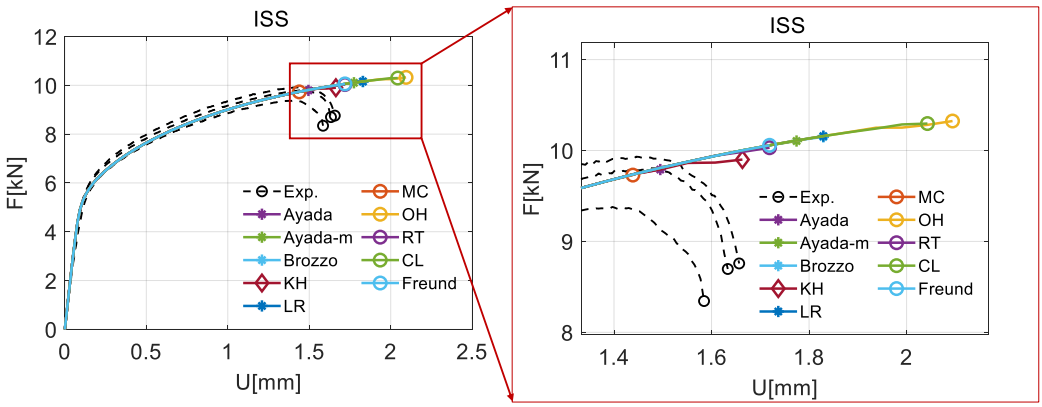

Figure 3.25: Force-displacement curves for ISS specimen geometry, displaying experimental results compared with multiple damage criteria models (MC, OH, Ayada, RT, Brozzo, CL, KH, LR, Freund). The inset zooms into the region of significant deviation.

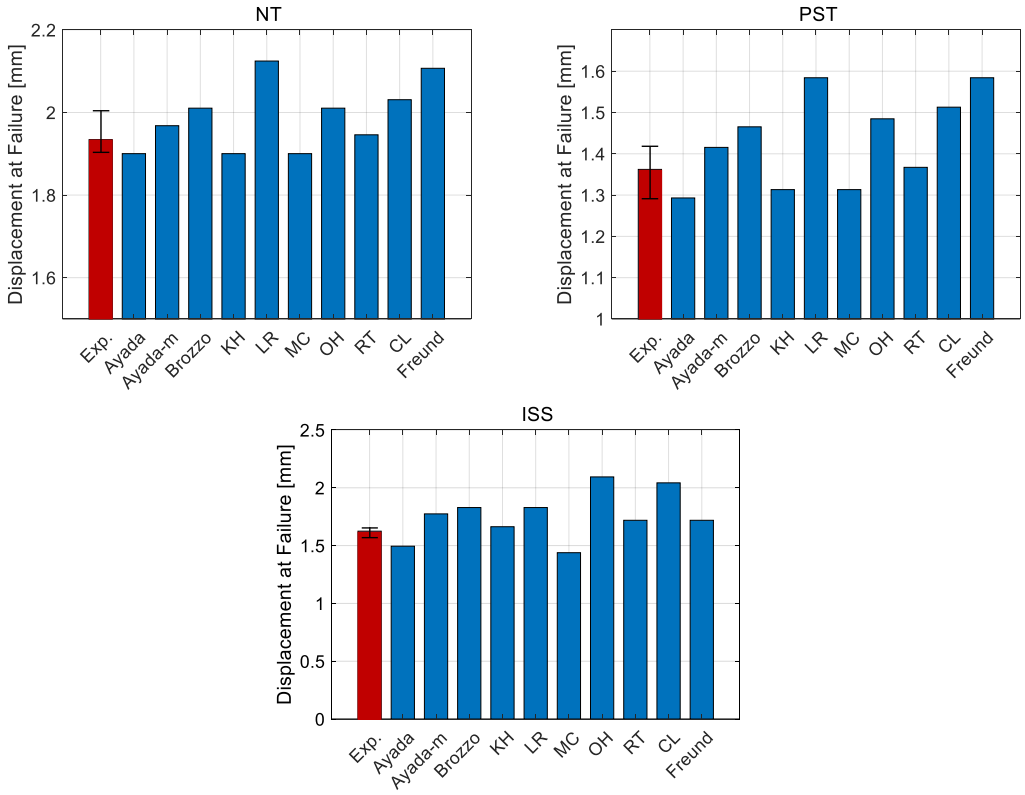

Figure 3.26: Experimental and numerical comparisons of displacement at failure for single parameter damage models.

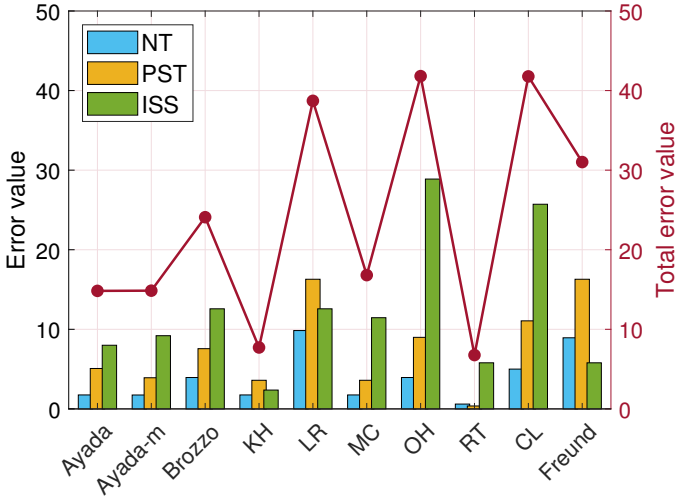

Figure 3.27: Error values for NT, PST, and ISS specimens along with total error values for single parameter damage models.

For the NT specimen, all models except LR and Freudenthal predict fracture displacement values relatively close to the experimental value. In particular, the Ayada, Ayada-m, KH, MC, and RT models successfully predict fracture under notch tensile conditions, showing the closest agreement with experimental data. In the PST specimen, similar to the NT, the predictions of several models, including Ayada, Ayada-m, KH, MC, and RT models, match the experimental fracture displacement more closely than others. For the ISS specimen, the comparison reveals that the KH, RT, and, interestingly, Freundenthal models most accurately predict fracture displacement. Conversely, the Ayada, Ayada-m and MC models, successful in the other two geometries, are not as successful as the other three in their applicability in in-plane shear conditions.

Overall, the analysis of Figure 3.27 reveals that different damage models' ability to predict fracture displacements under different stress states varies. The KH and RT models stand out for their consistency and reliability. In contrast, the Ayada and Ayada-m models may require further refinement to improve their accuracy, especially for in-plane shear conditions. In contrast, the CL, OH, and LR models exhibit the highest total error values, with significant errors observed, especially in the ISS sample estimates.

3.5.2 Multiple Parameter Damage Criteria

While single-parameter models can be calibrated using a uniform tensile (ST) specimen, which provides a simple approach to parameter determination, multiple-parameter models require additional specimens to capture the behavior of materials under different stress states. Additionally, with additional parameters such as stress triaxiality and Lode parameter in these models, a more complex method for calibration is needed. First, these models are represented in 2D or 3D with the help of fracture locus. Average stress triaxiality and average Lode parameter are needed to create each model's fracture curve or surface. The average formulas of these two parameters are as follows:

$$\begin{aligned} \eta_{\text{ave}} &= \frac{1}{\bar{\varepsilon}_{\text{f}}} \int_0^{\bar{\varepsilon}_{\text{f}}} \eta\left(\bar{\varepsilon}_{\text{P}}\right) \mathrm{d}\bar{\varepsilon}_{\text{P}} \\ L_{\text{ave}} &= \frac{1}{\bar{\varepsilon}_{\text{f}}} \int_0^{\bar{\varepsilon}_{\text{f}}} L\left(\bar{\varepsilon}_{\text{P}}\right) \mathrm{d}\bar{\varepsilon}_{\text{P}} \end{aligned} \tag{3.3}$$

First, FE analyses of the modeled material's plastic behavior are simulated using only the plasticity and averaging subroutine. Then, the average stress triaxiality and Lode parameter values are subtracted up to the experimentally observed breaking point. The place where there are sudden decreases in the force-displacement curves is taken as the beginning of fracture, and the equivalent plastic strain value at this point is chosen as failure strain. The average failure stress value obtained from four tests is used for ST, NT, PST, and ISS. The failure strain and mean T, $\bar{\theta}$ values are taken from a critical element determined by the maximum equivalent plastic strain. The critical elements in ST, NT, and PST are located at the center of the specimens. In contrast, the critical element of ISS is located at the center near the curved region in the concentration region. When choosing the critical element, when looking at the literature, it is seen that the equivalent plastic deformation is taken from the point where it is highest. The failure strain, averaged T, and average $\bar{\theta}$ are given in Table 3.6.

The model's function is adapted to the fracture location in 2D or 3D, depending on the requirements of the model with values in the table below. This fitting process is performed using MATLAB's curve fitting tool, which helps model the fracture line or surface. The parameter set that best fits this curve or surface is defined as the

Table 3.6: Fracture strain, averaged T and $\bar{\theta}$ for all specimens.

Specimen	T_{ave}	$\bar{\theta}_{ave}$	ε_f
ST	0.3852	0.9251	0.6240
NT	0.4861	0.7681	0.5151
PST	0.5608	0.5941	0.4691
ISS	0.0592	0.1416	0.5660

damage parameters of that model. The element deletion is opened and repeated with the obtained plasticity and damage models to examine the post-breakage behavior of the models. This iterative process ensured that the model could reliably predict the onset and progression of damage under various loading conditions.

The parameters of the models with multiple parameters, whose formulas are given in Chapter 2, are defined by following the above procedure. Oyane-Sato and JC models are calibrated using ST, NT and PST results. Temperature and strain rate dependent damage parameters D_{24} and D_{25} included in the JC and MMC model are taken from [113]. Oyane-Sato and JC damage model parameters are given in Table 3.7. Figure 3.28 shows the fracture location for the Oyane-Sato and JC models, respectively. Each point in the plots belongs to a specimen under a different stress state and is positioned in 2D space according to the average stress triaxiality and failure strain value.

Table 3.7: Parameters of the Oyane-Sato and JC damage models for IN718.

D_{11}	D_{12}			
2.417	7.487			
D_{21}	D_{22}	D_{23}	D_{24}	D_{25}
0.0989	1.142	2.039	0.04	0.89

Six parameters of BW and MMC are identified in the same way. These two models have six parameters, and the number of tests is insufficient to model simultaneously. Therefore, the parameters are calibrated iteratively. The parameters are defined using the tabular data in Table 3.8, with D_{44} set to 1 for the MMC model. Fracture loci with stress triaxiality, Lode angle parameter, and failure strain axes in the 3D space

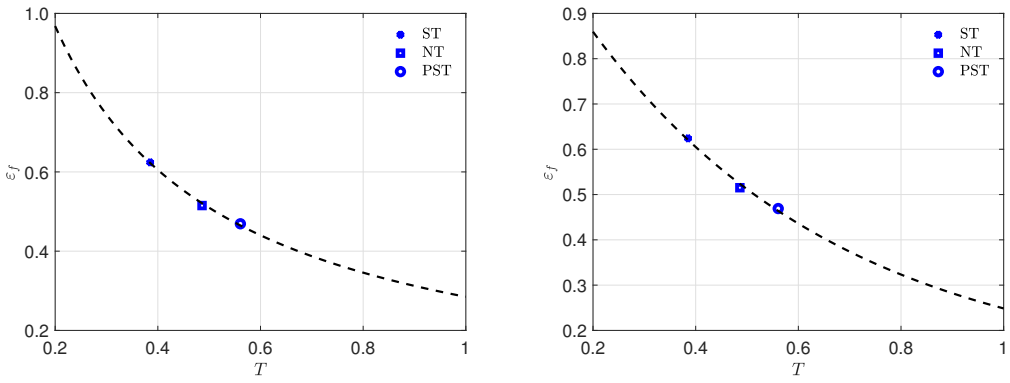

(a) Fracture locus for the Oyane and Sato.

(b) Fracture locus for the JC.

Figure 3.28: Calibrated fracture loci for the Oyane-Sato and JC models.

of these two models are shown in Figure 3.29. Likewise, the parameters and fracture loci of the models belonging to the Lou family are shown in Table 3.9 and Figure 3.30.

Table 3.8: Parameters of the BW and MMC damage models for IN718.

D_{31}	D_{32}	D_{33}	D_{34}	D_{35}	D_{36}
1.468	2.194	0.479	0.004632	0.2968	0.1
A_4	D_{41}	D_{42}	D_{43}	D_{44}	n_4
1910	19.02	16630	2.405	1	2.158

Figure 3.31 compares the force-displacement curves for different specimen geometries (ST, NT, PST, and ISS), showing the experimental results alongside multi-parameter damage models, including Oyane, JC, BW, MMC, DF2013, DF2014, and DF2015. For the ST, all of the models are consistent with the experimental results. Some models predict damage initiation a few steps before or after. In the case of NT, all models show a good fit except DF2014 and DF2015, but these two models are observed to reach the critical value earlier than the other models. PST curves agree well with experimental data, especially in the initial elastic and early plastic regions. As in the NT, except for the DF2014 and DF2015 models, other models made successful predictions in the PST. For the ISS, the failure initiation point of the MMC, DF2013 and

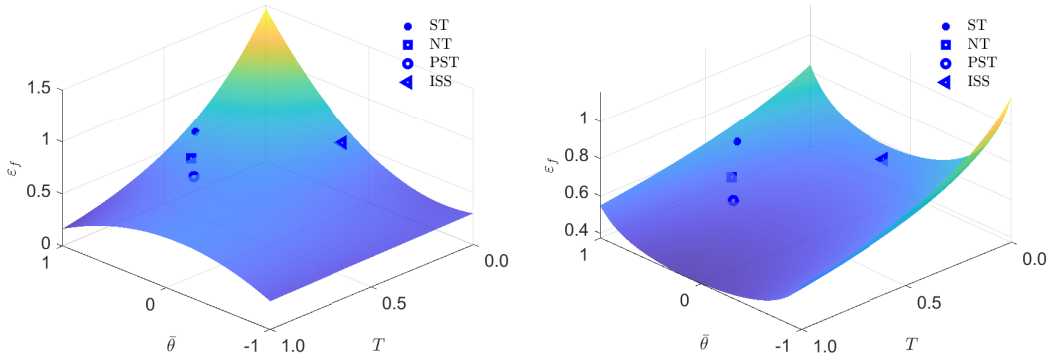

(a) Fracture locus for the BW.

(b) Fracture locus for the MMC.

Figure 3.29: Calibrated fracture loci for the BW and MMC models.

Table 3.9: Parameters of the DF2013, DF2014 and DF2015 damage models for IN718.

D_{51}	D_{52}	D_{53}		
2.861	0.4314	0.6736		
D_{61}	D_{62}	D_{63}	C_6	
1.61	0.8312	0.5314	0.333	
D_{71}	D_{72}	D_{73}	D_{74}	C_7
0.9688	1.037	0.4672	1.488	0.333

DF2014 models is quite successful, while the JC and Oyane-Sato models overpredict the initiation point. The BW model gives a result far from the experimental results, even in the hardening part.

Figure 3.32 also shows the displacement at damage for different damage models (Oyane, JC, BW, MMC, DF2013, DF2014 and DF2015) in comparison with experimental results for three specimen geometries. Displacement values predicted by different models differ significantly. For the NT geometry, the JC and DF2013 models predict higher displacement values at failure compared to the experimental results. In contrast, the Oyane, MMC, and BW models match the experimental values closer. For PST and ISS geometries, the DF2013, DF2014, and MC models tend to predict displacement values that are consistent with the experimental results. In general,

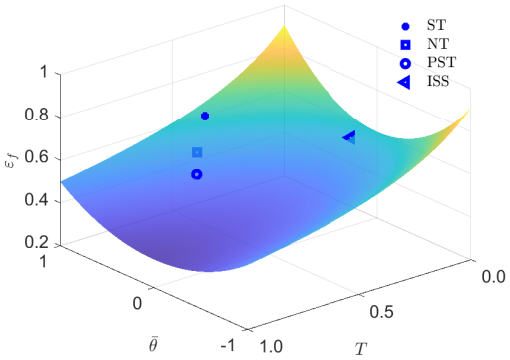

(a) Fracture locus for the DF2013.

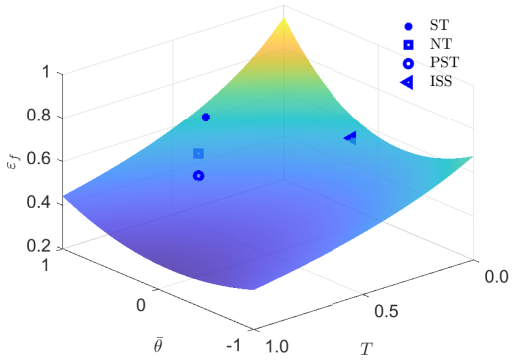

(b) Fracture locus for the DF2014.

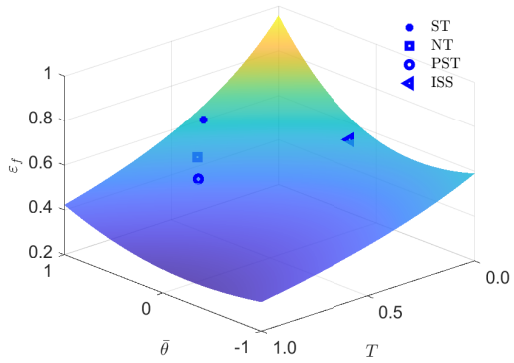

(c) Fracture locus for the DF2015.

Figure 3.30: Calibrated fracture loci for the DF2013, DF2014 and DF2015 models.

displacement at failure varies between models, highlighting differences in predictive capabilities.

Figure 3.33 compares the error values of different damage models with the total error value for NT, PST and ISS geometries. The DF2015 model exhibits high error values for all three geometries, indicating its low accuracy in predicting displacement at the time of damage. While the JC model is successful in NT and PST specimens, it made a very unsuccessful prediction in the ISS specimen in pure shear geometry. The DF2013 and DF2014 models also show lower error values than the JC model but vary between specimen geometries. The total error value represented by the red line highlights the cumulative accuracy of each model across all geometries. The Oyane and MMC models show lower total error values, indicating a better overall

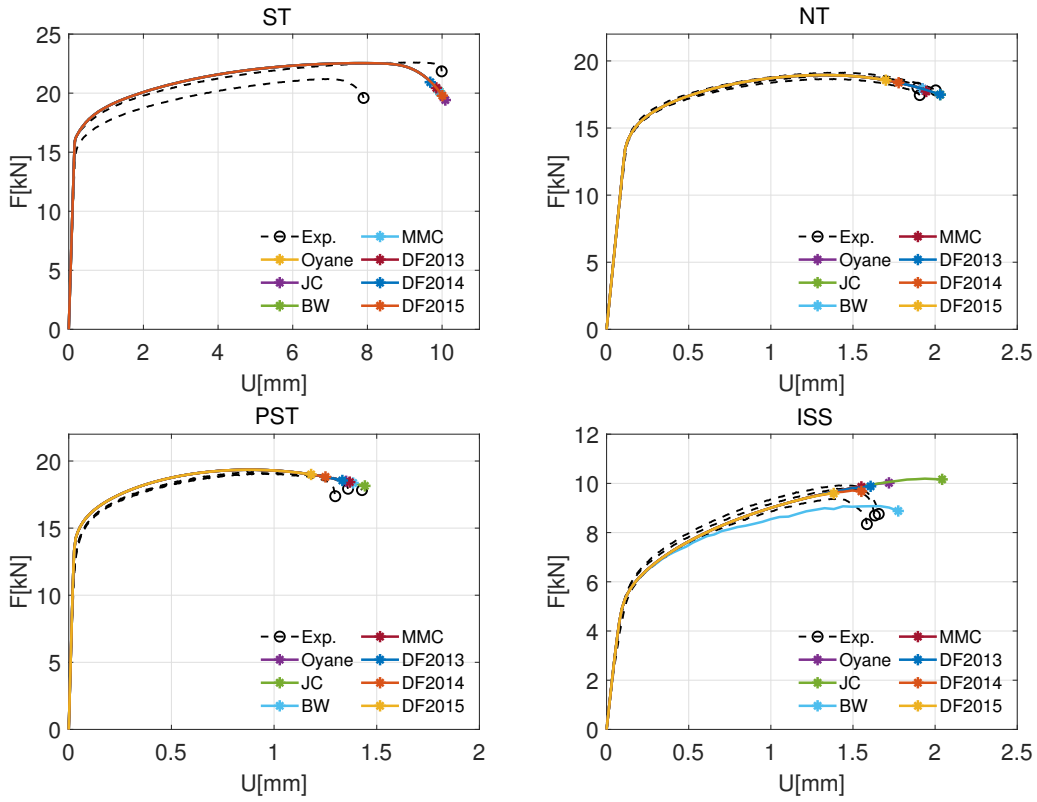

Figure 3.31: Experimental and numerical comparisons of displacement at failure for different damage models.

performance predicting damage displacements in different geometries.

The calibrated plasticity and damage models will be applied to the flow forming process in Chapter 5. These calibrated damage models will be compared with experimental results from the flow forming process to evaluate their ability to predict forming limits and failure locations, similar to their application in ductile failure. Following this, the effects of process parameters will be examined. The plasticity models for IN718 will be extended to study the influence of hardening rules on the stress state during flow forming. Finally, the flow forming results for Al204-O using the VM and BW yield functions will be compared.

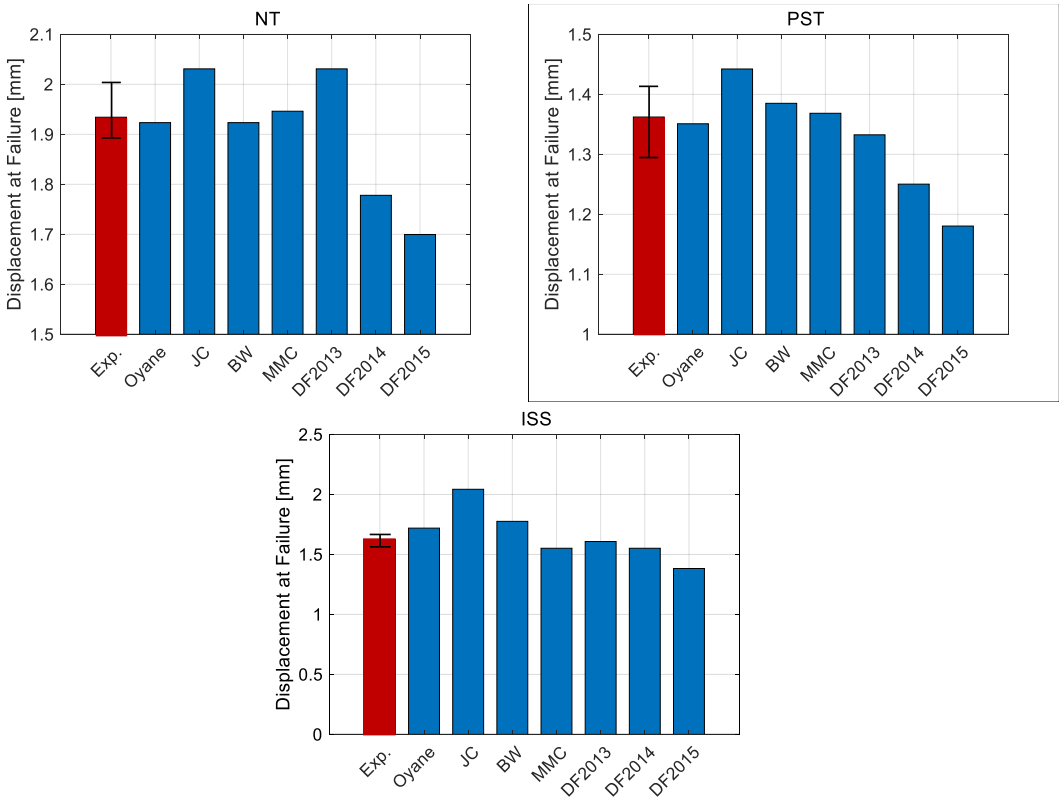

Figure 3.32: Experimental and numerical comparisons of displacement at failure for multiple parameter damage models.

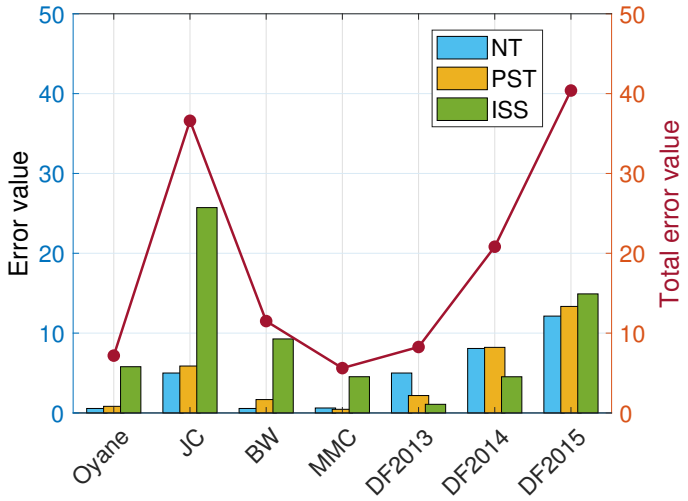

Figure 3.33: Error values for NT, PST, and ISS specimens along with total error values for multiple parameter damage models.

CHAPTER 4

FLOW FORMING TRIALS AND FINITE ELEMENT MODELLING

This chapter addresses the experimental trials and finite element (FE) modeling techniques used in this study to conduct a parameter study of the flow forming process. The experimental setup and geometries of parts used for flow forming experiments will be explained in detail. Following this, the FE modeling approach is presented, covering mesh and mass scaling studies to ensure accurate and efficient simulations. The experimental data and the developed FE model will be used for experimental comparison and parameter study. The results are presented in the subsequent chapter.

In the flow forming process, various terms and parameters significantly influence the process's efficiency and the product's quality. For example, the feed rate represents the roller's axial speed, and its unit is mm/s. Revolution speed controls the rotation speed of the mandrel, and its unit is rpm. Feed ratio, which has different definitions, is defined in this study as the ratio of revolution speed to feed rate. Moreover, force components such as circumferential, axial, and radial forces represent three perpendicular components of roller forces. While formability (spinnability) defines the maximum thickness ratio that can be reduced, the wall thickness of the part is decreased by a certain percentage, called the thickness reduction ratio. Thickness reduction (TR) is formulated as

$$TR = \frac{t_i - t_f}{t_i} \times 100. \tag{4.1}$$

where t_i and t_f refer to the initial and final thickness of the part, respectively.

Figure 4.1 shows that the rollers have a specific radius and two angular values: attack and exit angles. The rollers are modeled around the mandrel with a 120-degree spacing between them. To achieve the desired reduction ratio, the positions of the rollers in the coordinate system are determined by taking into account the mandrel

diameter, roller diameters, and the formula provided above. The offsets of the rollers define the staggered roller configuration. While these offsets shown in Figure 4.2 are defined as axial and radial, the term stagger offset is often used for axial offset. As illustrated in Figure 4.2, axial offset refers to the axial distance between the rollers. While some trials utilize a zero axial offset, working with axial offsets of 5 mm or 7 mm in REPKON is common. The crucial point is that when the axial offset is zero, all rollers begin forming the preform simultaneously. If a specific axial offset exists, the rollers form the preform sequentially. On the other hand, radial offset refers to the percentage difference in the reduction ratios of the rollers relative to each other. For example, when the radial offset is zero, all rollers have the same reduction ratio and apply equal force to the workpiece. In cases where the radial offset differs from zero, the reduction ratios applied by the rollers vary. For instance, in a scenario using three rollers to achieve a 50% reduction ratio in three steps, the first roller reduces by 30%, the second by 40%, and the final roller by 50%, thereby gradually thinning the preform with a specific radial offset. The term radial offset describes these differences in the reduction ratio percentages among the rollers.

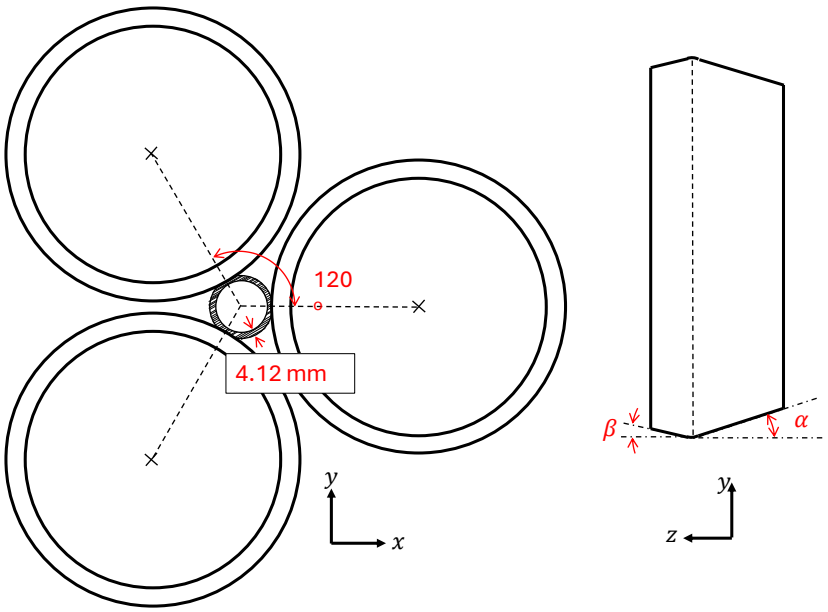

Figure 4.1: Geometry of the rollers. Roller attack angle $\alpha = 20\,\mathrm{deg}$ and exit angle $\beta = 6\,\mathrm{deg}$.

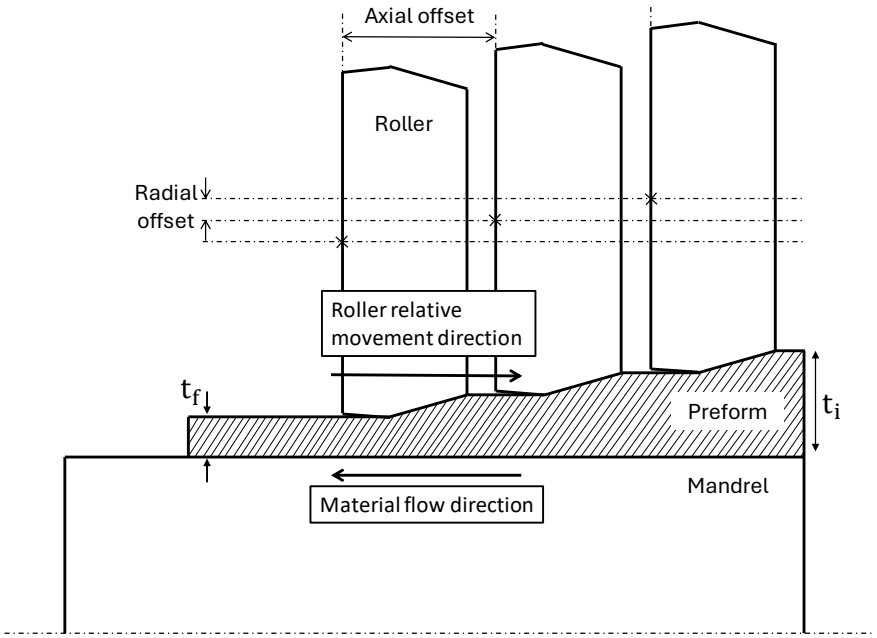

Figure 4.2: Schematic of the roller axial and radial offsets.

4.1 Flow Forming Trials

This section will discuss the part geometries and the experimental setup used in flow forming trials. The trials are conducted on cylindrical tubes made of Inconel 718 alloy using a 3-roller Repkon flow forming machine. The three rollers are placed evenly, with 120° between them, and there is no axial and radial stagger. The detailed geometries of the preform and the rollers are shown in Figures 4.1 and 4.2. The tube-shaped preform has an inner diameter of 40 mm and a wall thickness of 4.12 mm. The entry angle of the rollers is 20 degrees, while the exit angle is 6 degrees.

In the experimental work, axial and radial offsets are set to zero; thus, all rollers contact the preform simultaneously at the start of the process and apply the same reduction ratio. The preform is clamped at one end and pushed through the rollers with a constant feed rate of 0.833 mm/s. The mandrel rotates at a speed of 125 RPM. A lubricant is used on the outer surface of the preform during the process to reduce friction and aid cooling. The preform is initially at room temperature. However, it is observed that during the process, the temperature of the part increased, causing the outer surface to redden due to the temperature rise.

(a) (b)

Figure 4.3: Experimental flow forming results with 37.5% and 70% thickness reduction ratios.

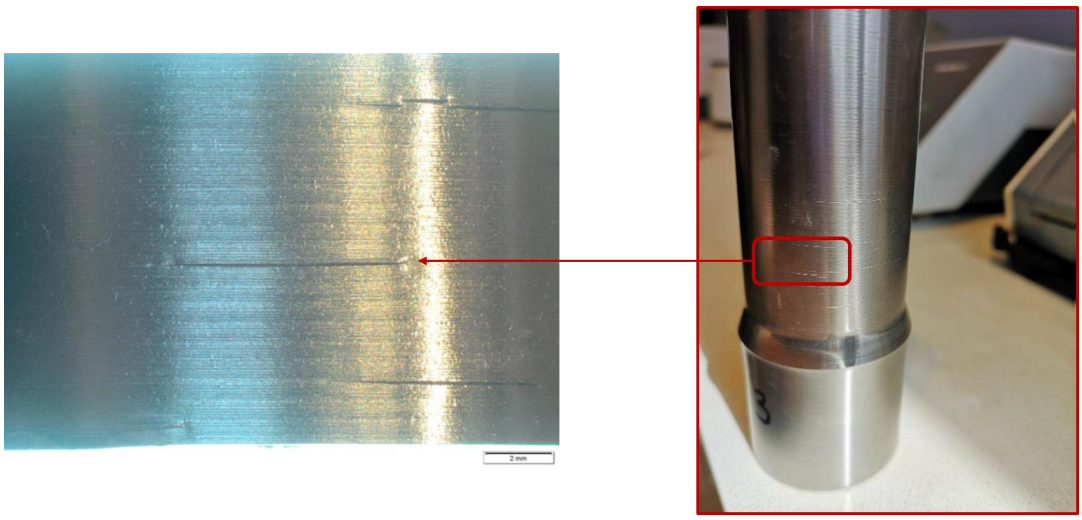

Figure 4.4: The flow forming trial in the 50% thickness reduction ratio, and zoom view of radial cracks.

Trials are conducted at 3 different reduction ratios: 37.5%, 50% and 70% to observe their effects on material flow and defect formation. These trials demonstrate that the

forming process can be completed at 37.5% and 50% TR ratios, but complete fracture of the part occurs at a 70% reduction ratio. In the sample with a 50% TR ratio, cracks are observed on the outer surface, as shown in Figure 4.4. Forming distinctly in the radial direction throughout the formed portion, while the inner surface remained defect-free.

4.2 Finite Element (FE) Modelling

The damage occurring during the trials is examined using finite element (FE) modeling using the dynamic explicit solver in Abaqus, applying the calibrated and validated damage criteria in Chapter 3. The FE model of the flow forming process is demonstrated in Figure 4.5. This model comprises a preform, a mandrel and three rollers. In actual experiments, the mandrel rotates at a constant rotational speed and the rollers move axially at a constant feed rate. In FE modeling, additional kinematic constraints are required to move and rotate the deformable body, significantly increasing computational time. All movements are applied to the rollers while keeping the mandrel stationary to enhance efficiency. Consequently, in the FE model, the rollers possess radial (revolution speed) and axial (feed rate) speeds. While the part flows by the rollers moving this way, the preform moves radially along with the mandrel in the actual process. The preform and mandrel are also constrained at endpoints on the back surface in all directions to prevent rigid body motion. The back surfaces of the mandrel and preform, as illustrated in Figure 4.6, are positioned opposite the flow direction and on the side of the movement direction rollers.

The mandrel and rollers are modeled as rigid bodies, while the preform tube is modeled as deformable. Positioning the rollers according to the mandrel controls the reduction ratio and stagger offset. Rollers are placed around the mandrel with 120 degrees between them and a specific axial and radial offset. There is no offset value in experimental trials, but offsets at various values are studied to examine the effect of the stagger offset parameter.

There is surface-to-surface contact between the mandrel-preform and the preform-roller. The model has tangential and normal contact features, with a friction coeffi-

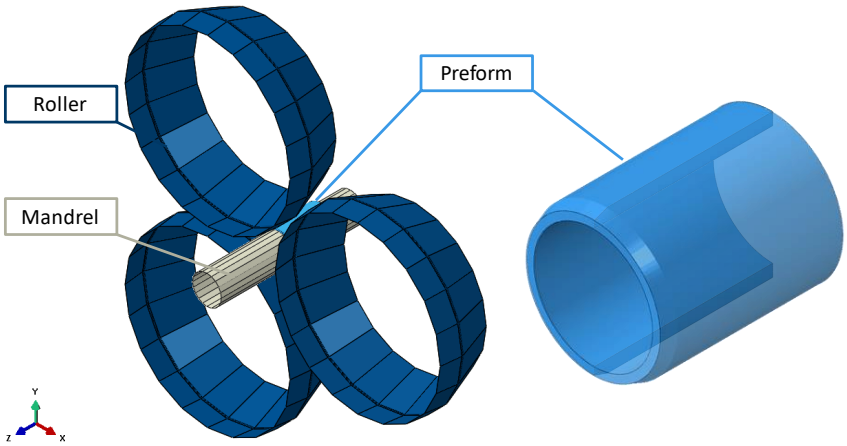

Figure 4.5: The finite element model of flow forming process.

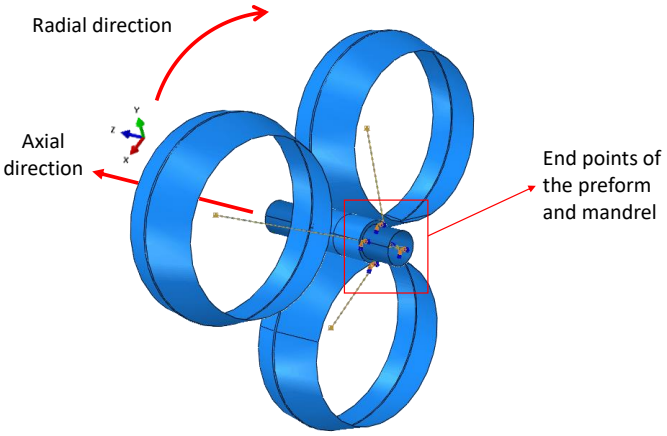

Figure 4.6: Boundary conditions of flow forming process.

cient of 0.12 for the contact between the mandrel and the preform and 0.08 for the contact between the rollers and the preform. Since no experimental friction values are available, these values are selected based on an average estimation. A mesh convergence study is conducted in the various configurations. Details will be mentioned in the next section.

Two different models are created to study the effect of temperature in the FE simulations. The first model, labeled as model 1 in the following figures, does not include any temperature effects in the plasticity or damage model. Model 2 is a fully displacement-temperature coupled model that includes heating up due to plastic de-

formation and friction. Cooling is simulated with a constant heat constant applied over the outer surface of the preform with a temperature of 293 K and film coefficient of 5.5. Heat conduction inside and between the preform, the mandrel, and the rollers are also modeled. The hardening relation and JC, MMC damage model have temperature-dependent parts while single-parameter criteria do not in model 2. However, since temperature dependency exists in the hardening relation, the temperature effect and change can be indirectly observed in single-parameter models.

4.2.1 Mesh Study

While performing the mesh study, the preform tube is meshed using hexagonal elements with reduced integration (C3D8R and C3D8RT), and an improved hourglass control is employed to prevent mesh distortion. Different meshes are tested to balance computational efficiency and accuracy of results. The model's mesh size sensitivity is analyzed by comparing the predicted results with experimental data. The optimum mesh density is determined based on the convergence of key parameters (e.g., strain distribution and damage localization).

During the process, the elements shrink in thickness and lengthen in the axial direction. For this reason, working with a uniform mesh can cause significant disproportions in element sizes as the process progresses, potentially affecting the FE results. Therefore, it is essential to investigate different mesh configurations to determine the most efficient and accurate approach. Three different mesh configurations are initially tested to evaluate their impact on calculation time and result accuracy. Elements with three different configurations are studied, as shown in Figure 4.7, to observe the effect of the ratio. The first is the uniform element with all sides equal, the second is the non-uniform element with a certain ratio for the axial side, and the third is the non-uniform element with specific ratios for both axial and radial sides. The analyses use a feed rate of 2 mm/s and a revolution speed of 300 rpm, with mass scaling applied as a time increment of 5e-6.

As shown in Figure 4.7, the first configuration uses a uniform mesh with an element size of 0.587 mm. The analyses are conducted on a formed length of 26 mm, and at the end of this forming process, the highest von Mises stress (VM) and equivalent

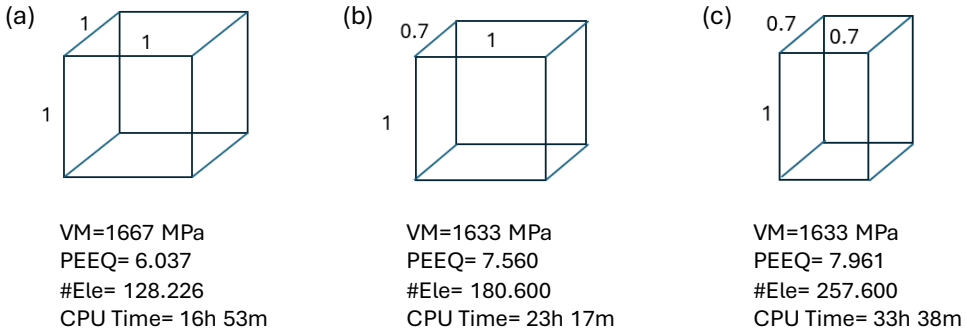

Figure 4.7: Different configurations of mesh: (a) Uniform mesh, (b) Non-uniform mesh refined in the axial direction, (c) Non-uniform mesh refined in both the axial and radial directions.

plastic strain (PEEQ) values in the preform are compared. This configuration results in 128,226 elements, a VM of 1667 MPa, and a PEEQ of 6.037. The computational time for this configuration is 16 hours and 53 minutes. The second configuration uses a finer mesh with an element size of 0.412 mm in the axial direction, resulting in 180,600 elements. This configuration produces a VM of 1633 MPa and a PEEQ of 7,560 with a computational time of 23 hours 17 minutes. The third configuration also uses an element size of 0.412 mm but a different mesh size in radial and axial directions, resulting in 257,600 elements. This configuration achieves a VM of 1633 MPa and a PEEQ of 7.961. The computational time for this setup is 33 hours 38 minutes.

Based on these initial experiments, reducing the element size increased the accuracy of the results, as evidenced by the closer alignment of VM and PEEQ values. However, this also significantly increased the computational time. Therefore, a balance between mesh density and computational efficiency is sought to optimize the mesh configuration for flow-forming simulations.

The equivalent plastic strain (PEEQ) distributions for each configuration are shown in Figure 4.8. It can be observed that the more refined meshes in configurations 2 and 3 have a higher strain distribution than configuration 1. However, a very high PEEQ value is not preferred as it can lead to distortions and significantly alter the geome-

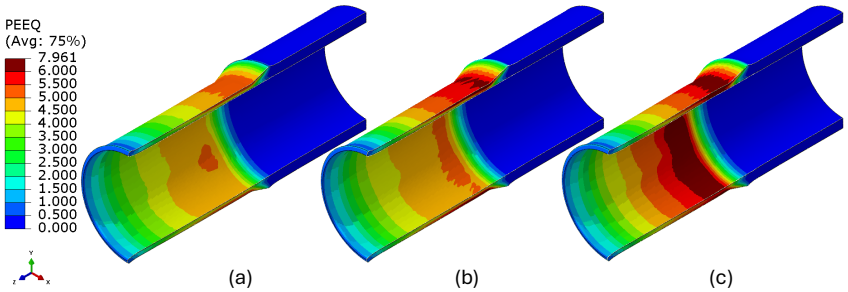

Figure 4.8: The equivalent plastic strain (PEEQ) distributions are shown for the three mesh configuration: (a) a uniform mesh, (b) a non-uniform mesh refined axially, and (c) a non-uniform mesh refined both axially and radially.

try of the formed material. In addition to PEEQ, damage distributions according to Ayada and KH criteria are shown in Figure 4.9. Finer mesh configurations again show more detailed and localized damage patterns. Significantly, the damage distributions for configuration 2 exhibit a more uniform distribution than the other configurations. Based on these results, Configuration 2 is the optimal balance between computational efficiency and result accuracy. It provides sufficiently detailed strain and damage distributions without excessive computational time.

It has been observed that using a specific ratio for one edge instead of a uniform mesh significantly affects the analysis. Therefore, to decide what the value of this ratio should be, the axial edge is analyzed with values at different ratios. The ratio used refers to the axial edge relative to the radial edge. In the analyses, the radial edge is kept constant, while the dimensions of the axial edge are varied. Based on different ratios of 1, 0.9, 0.8, 0.7, and 0.6, the equivalent plastic strain (PEEQ) distribution shows significant differences in Figure 4.10 at the target forming distance of 26 mm. When the ratio is 1, the PEEQ distribution is more homogeneous but has lower localized strain values. As this ratio increases, the PEEQ distribution shows more localized strain concentrations. However, excessive can sometimes lead to unrealistic deformation estimates and potential numerical instabilities.

The damage distributions for the Ayada and KH criteria across different element size ratios are illustrated in Figure 4.11. Damage localization becomes more evident for both damage criteria as the element ratio decreases from 0.8 to 0.6. The Ayada crite-

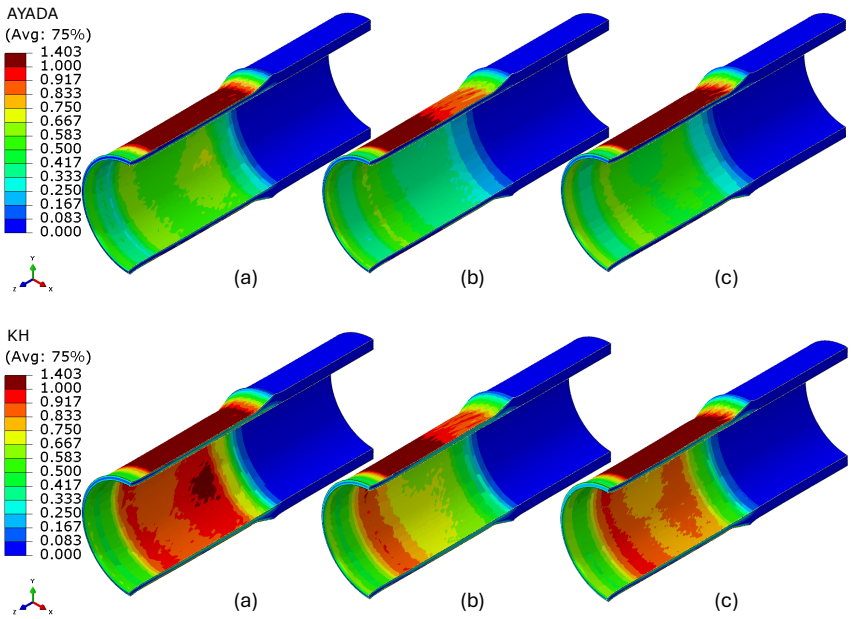

Figure 4.9: Damage distributions for Ayada and KH criteria across the three mesh configuration: (a) uniform mesh, (b) non-uniform mesh refined axially, and (c) non-uniform mesh refined both axially and radially.

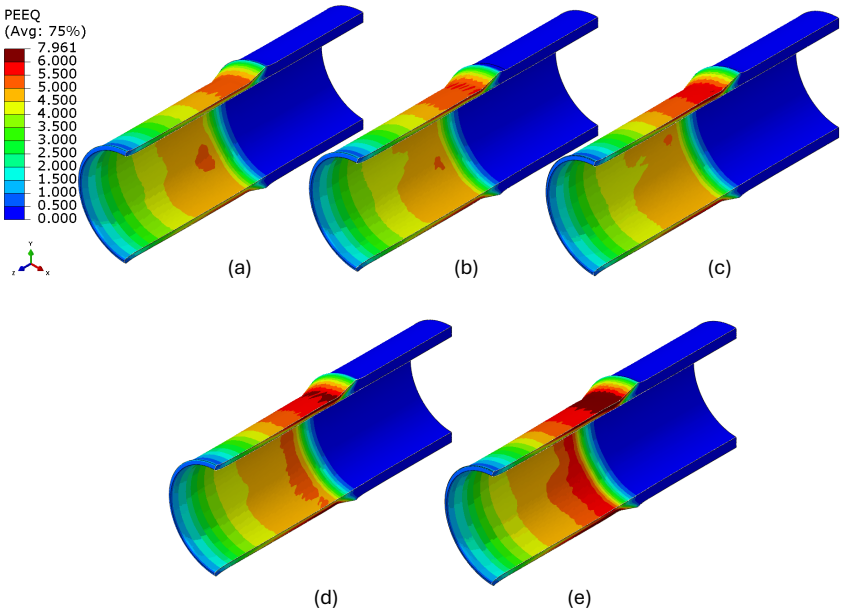

Figure 4.10: Equivalent plastic strain (PEEQ) distribution for various element size ratios: (a) 1, (b) 0.9, (c) 0.8, (d) 0.7, and (e) 0.6.

rion (top row) consistently increases localized damage areas with finer meshes, highlighting more detailed damage regions. Similarly, the KH criterion (bottom row) shows a similar trend, capturing higher damage densities with finer meshes. The maximum damage values at 0.7 and 0.8 are pretty close, but the damage distribution at 0.7 is less localized than at 0.8. These observations suggest that reducing the element ratio increases the ability to capture localized damage events accurately but also increases computational costs. From these findings, it is clear that the ratio of 0.7 provides a good balance between capturing localized deformations and maintaining numerical stability without excessively increasing computational time.

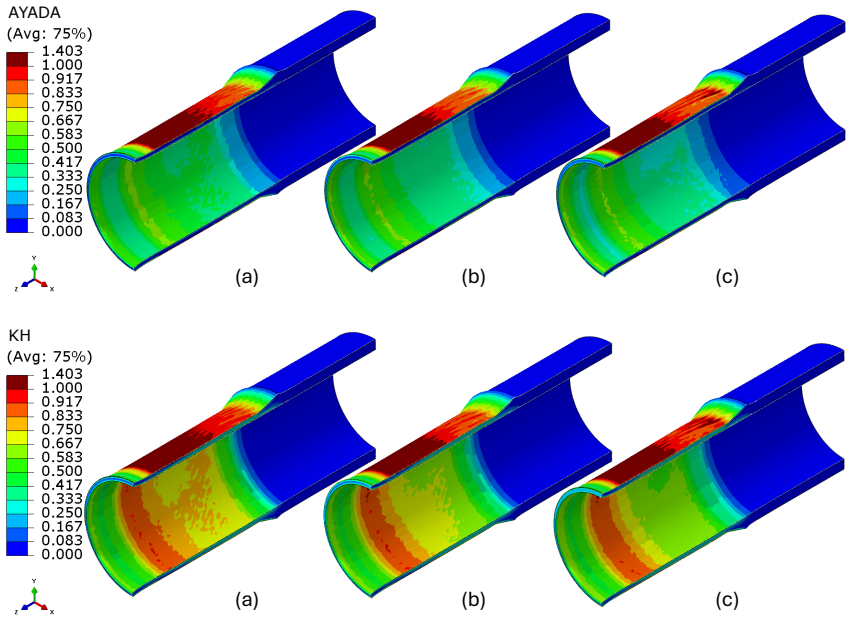

Figure 4.11: Damage distributions for different element ratios using Ayada and KH criteria: (a) 0.8, (b) 0.7, and (c) 0.6.

After selecting Configuration 2 (ratio = 0.7) as the most effective mesh configuration, a detailed study is carried out to determine the number of elements in the thickness of the preform. This study aimed to find a balance between computational efficiency and the accuracy of results. The number of members tested through the thickness is 4, 5, 6, 7, 8 and 9. Equivalent plastic strain (PEEQ) distributions for each configuration are shown in Figure 4.12. The results indicate that as the number of thickness elements increases, the PEEQ distribution decreases and is localized. The cases with 6, 7, and 8 elements especially show that it is a suitable candidate when looking at the PEEQ

values and distributions.

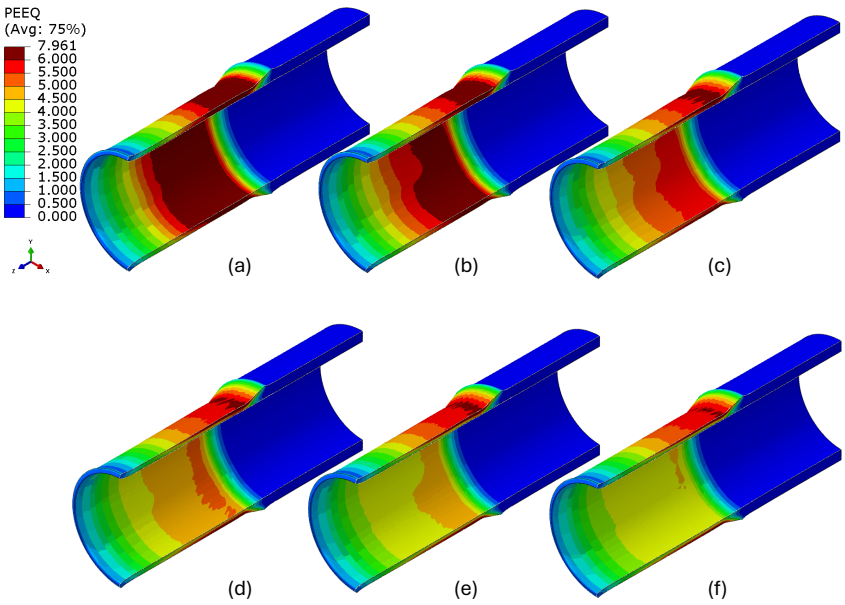

Figure 4.12: Equivalent plastic strain (PEEQ) distributions for Configuration 2 with varying numbers of elements through the thickness: (a) 4 elements, (b) 5 elements, (c) 6 elements, (d) 7 elements, (e) 8 elements, (f) 9 elements.

The damage distributions according to the Ayada and KH criteria are also examined using these configurations. The damage distributions for these criteria with varying numbers of elements through the thickness are shown in Figure 4.13. It can be observed that the configurations with 6 and 7 elements provide a detailed and accurate representation of the damage. However, considering the computational cost of finite element simulations, using six elements through the thickness is considered the appropriate choice, providing a good balance between computational time and accuracy.

These results show that for both damage criteria, the ratio 0.7 and the 6-element configuration across the thickness provide the optimal balance regarding computational time and accuracy. The mesh density in the right part of the model has been reduced to reduce calculation time and has a total of 154,800 elements; the model, which has six elements in the thickness direction, has elements sized of 0.589 mm in the radial direction and 0.412 mm in the axial direction, as shown in Figure 4.14.

Unlike in tensile tests, the kinetic energy exceeds the internal energy at the beginning

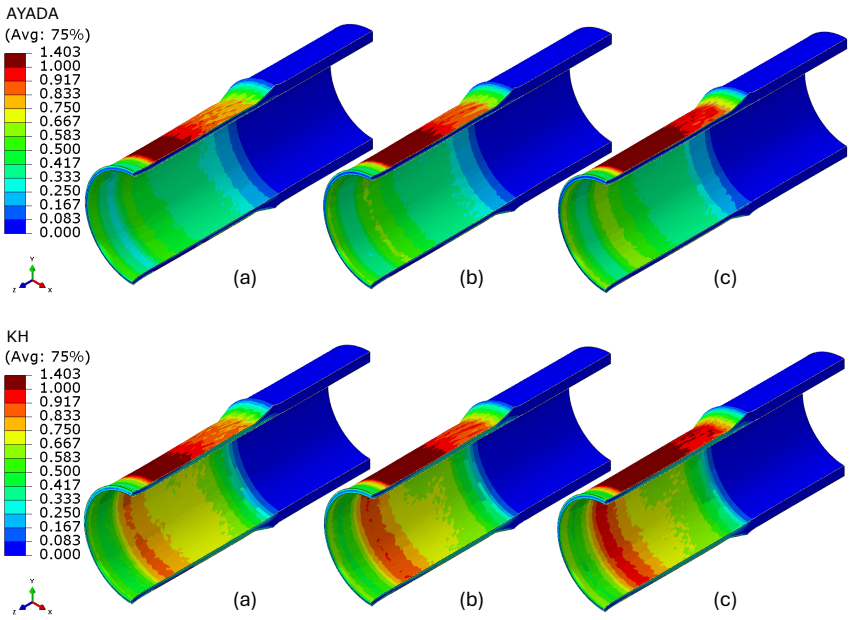

Figure 4.13: Damage distributions for Ayada and KH criteria with varying numbers of elements through the thickness: (a) 6 elements, (b) 7 elements, (c) 8 elements.

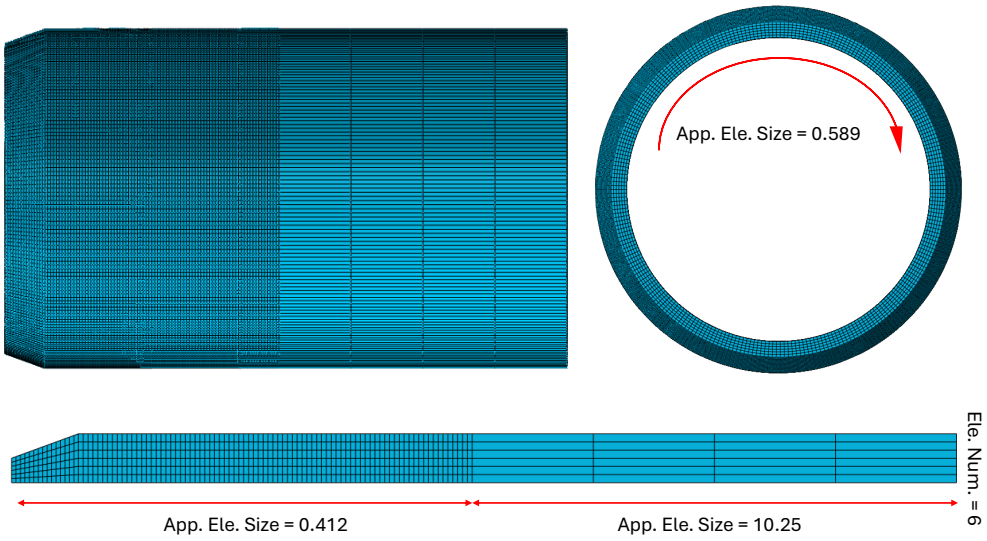

Figure 4.14: Meshing details of the flow forming model.

of the analysis for a brief period (see Figure 4.15). However, after this initial phase, the internal energy remains higher than the kinetic energy until the end of the analysis. This situation occurs only during a small fraction (0.2 seconds) of the 15-second

analysis, which is considered acceptable and indicates no significant dynamic effects.

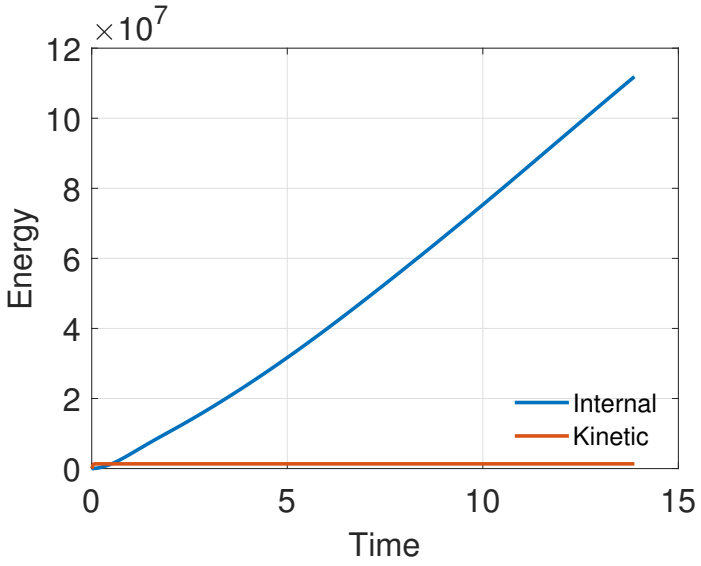

Figure 4.15: Energy-time plot showing the variation of internal and kinetic energy during the simulation.

4.2.2 Mass Scaling Study

The mass scaling technique is used to reduce the computational time while maintaining the accuracy of the simulations. Mass scaling is a method used in dynamic explicit simulations to artificially increase the mass of elements to allow more significant time steps and thus reduce computational time. However, it is crucial to ensure that the added mass does not significantly alter the physical response of the system. The impact of different mass scaling factors on the simulation results is examined to ensure that the dynamic effects do not change significantly. This study focused on evaluating the balance between computational efficiency and model suitability in capturing the failure prediction of the flow forming process.

This study examined five different mass scaling with 1e-6, 2e-6, 3e-6, 4e-6, and 5e-6 time increment values to observe their effect on the results. Equivalent plastic strain (PEEQ) distributions for various mass scaling time increments are shown in Figure 4.16. Damage distributions with different time increments according to the Ayada and KH criteria are shown in Figure 4.17. From the analysis, it can be seen that

as time increment increases, PEEQ values and damage distributions change slightly. Specifically, higher time increments tend to increase PEEQ and damage values. These results are indicative of more localized plastic deformation and damage accumulation.

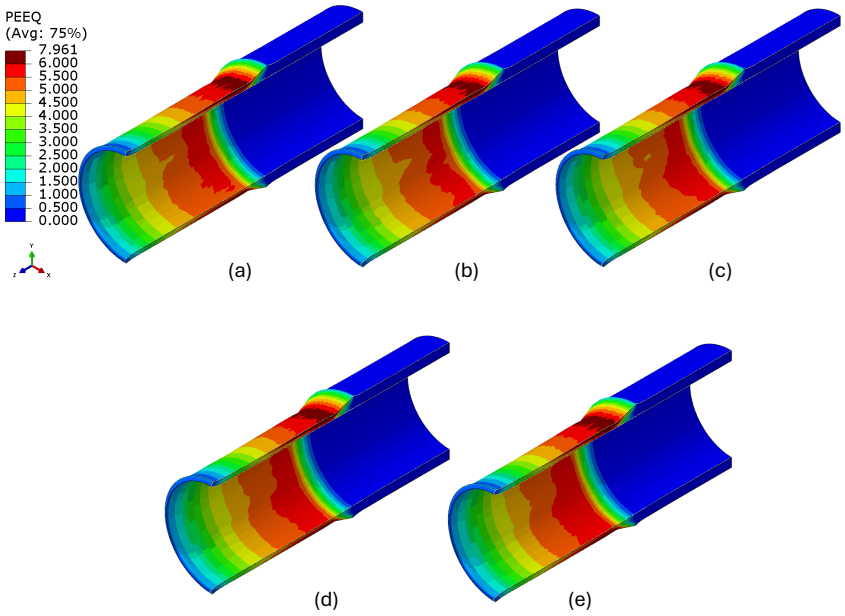

Figure 4.16: PEEQ distributions for different mass scaling time increments: (a) 1e-6, (b) 2e-6, (c) 3e-6, (d) 4e-6, (e) 5e-6.

DMASS, calculated by Abaqus/CAE, indicates the percentage change in the total mass of the model as a result of mass scaling. As shown in Figure 4.18, the change of DMASS value over time varies considerably depending on the time increment value. As the time increment value increases, the material's artificially changing density value increases, resulting in more considerable mass changes.

Time increment changes over the simulation interval for different mass scaling values are shown in Figure 4.19. It can be seen that with increasing time increments, the stability of the time increment decreases, causing fluctuations that may affect the accuracy of the simulation results. In other words, at high time increment values, the time increment value does not remain constant throughout the process and tends to decrease to 3e-6. When comparing the computational times of the analyses, there is a noticeable decrease in CPU time from 1e-6 to 5e-6. The average computational times are approximately 137 hours, 69 hours, 46 hours, 35 hours, and 21 hours, re-

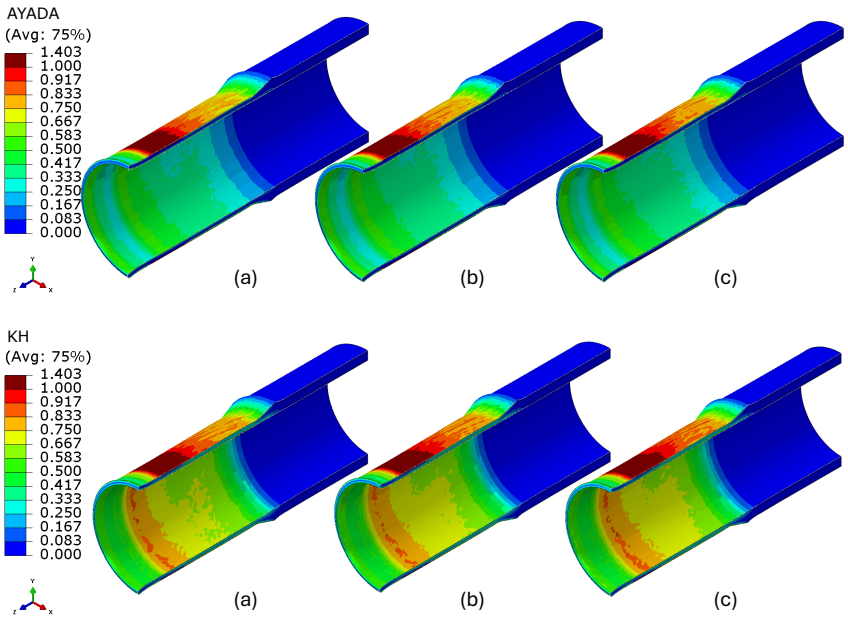

Figure 4.17: Damage distributions for different mass scaling time increments for Ayada and KH criteria: (a) 2e-6, (b) 3e-6, (c) 4e-6.

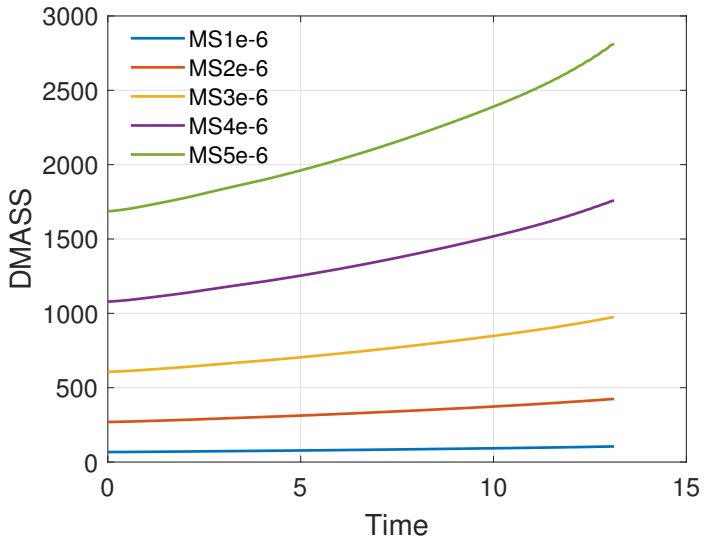

Figure 4.18: The effect of different time increment values on the DMASS value over time.

spectively. Consequently, while mass scaling can significantly reduce computation time, choosing an appropriate time increment is crucial to maintain the accuracy and stability of FE simulation results. This study balances computational efficiency and

result accuracy using a time increment 3e-6.

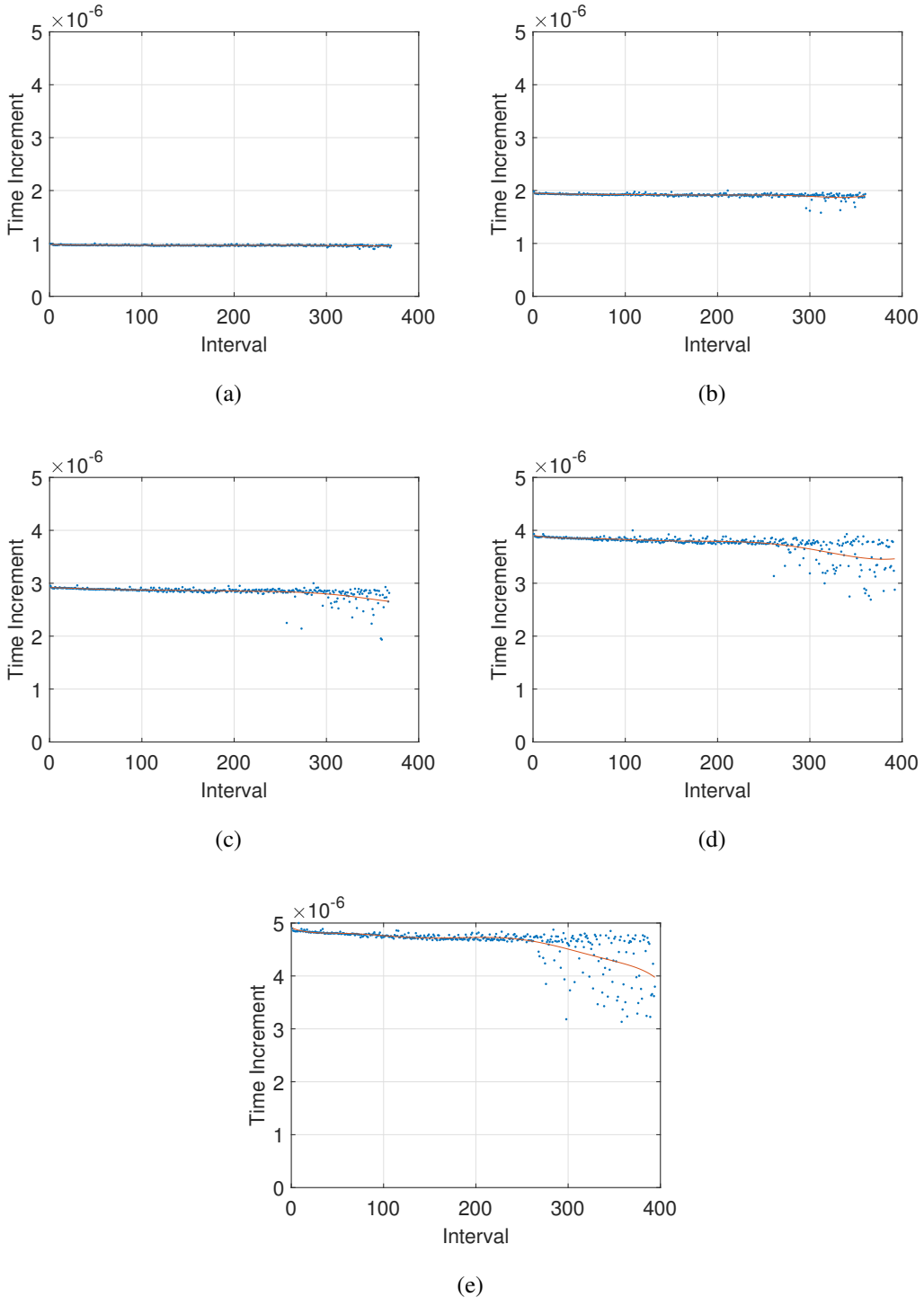

Figure 4.19: Time increment variations over the simulation interval for different mass scaling: (a) 1e-6, (b) 2e-6, (c) 3e-6, (d) 4e-6, and (e) 5e-6.

CHAPTER 5

RESULTS AND DISCUSSION

This chapter examines the effects of process parameters, hardening rules, and yield functions on the flow forming (FF) of IN718 and Al2024-O. The calibrated damage models for IN718 are first assessed for their capability to predict fracture during the flow forming process. Subsequently, the effects of process parameters such as feed rate, rotational speed, thickness reduction ratio, and roller offsets on damage and plastic strain in flow forming are analyzed for this material. Different hardening rules, including Voce, Swift, and modulated hardening, are evaluated for accuracy in predicting material response. For Al2024-O, the study compares the Bai-Wierzbicki yield function with the von Mises yield function to assess flow forming performance.

5.1 Comparison of Experiments and FE Results of Flow Forming

This section compares the forming limit predictions and failure location estimations of single and multiple parameter damage models for IN718 at three different reduction ratios. These comparisons have been conducted for a specific target forming distance and are also compared to how long the models can form.

5.1.1 Comparison of Single Parameter Damage Models

In this part, ten different single-parameter models are compared. These models include the Ayada, Ayada-m, Brozzo, Ko-Huh (KH), Le-Roy (LR), McClintock (MC), OH, Rice-Tracey (RT), Cockroft-Latham (CL), and Freudenthal criteria. Figure 5.1 and Figure 5.2 show the results of flow forming FE simulations with single-parameter

damage models. Figure 5.1 shows the damage distribution in the preform after flow forming at a 37.5% thickness reduction rate predicted by various damage models. These results show that if the damage prediction of models at the thickness reduction ratio exceeds one, these models cannot accurately predict the forming limits. Ayada, Ayada-m, KH, and MC models correctly predict that the damage values remain below one, and successful forming is achieved at this reduction ratio. Ayada, Ayada-m, KH, and MC models do not predict failure with maximum damage values of approximately 0.85, 0.879, 0.834, and 0.95, respectively. In contrast, the Brozzo, LR, OH, RT, CL and Freudenthal models show damage values exceeding 1. While cracks occur on the inner surface in the Brozzo, OH and CL models; LR, RT and Freudenthal also predict high damage accumulation throughout the entire part. Contrary to the experimental results, Brozzo, OH, and CL models predict high damage accumulation in certain areas on the inner surface, with damage values of 1.213, 1.070, and 1.113, respectively.

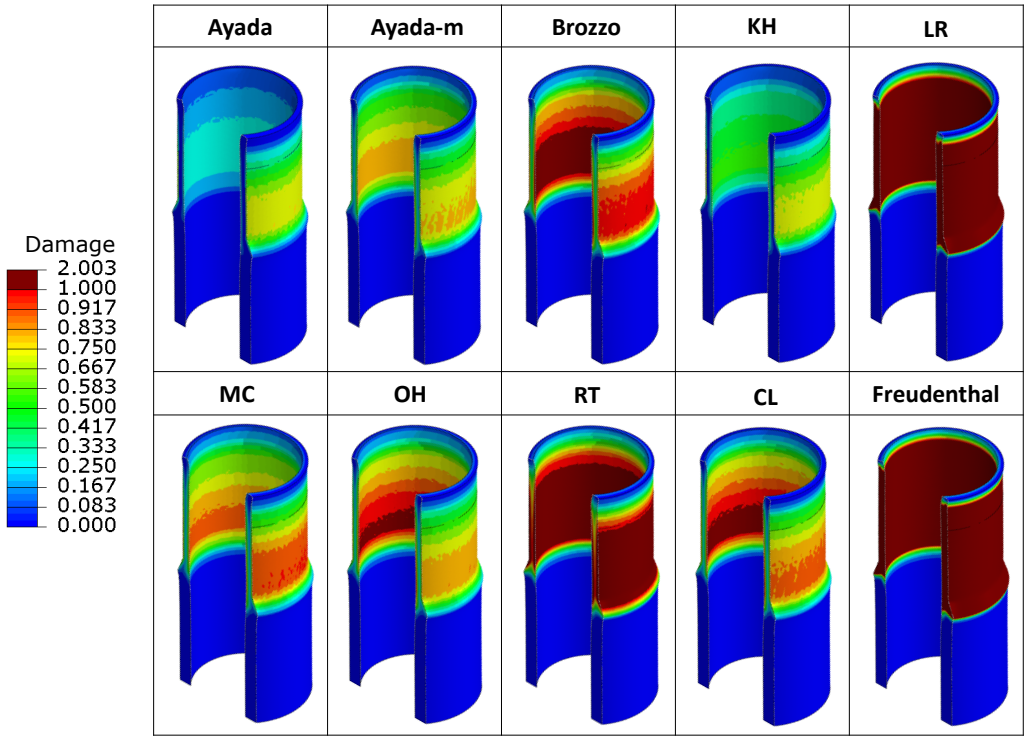

Figure 5.1: Numerical comparison of flow forming results of single parameter damage models with 37.5% thickness reduction .

Figure 5.2 shows the damage distribution of flow forming at 50% thickness reduction for the calibrated models. Damage distributions are presented for Ayada, Ayada-m, Brozzo, KH, MC, OH and CL models. However, this figure does not include models that cannot predict correctly at lower reduction ratios, such as LR, RT and Freudenthal. Although Brozzo, OH and CL models predict failure in the inner surface at a low reduction ratio, they are shown in this figure to see their performance at 50% reduction ratio where it should be observed that most of the part remains below the critical damage limit. However, except for Ayada, all other models predicted damage on both the outside and inside surfaces. Along with the Ayada model, the KH model also demonstrated good performance; however, in the KH model, the damage value slightly exceeded the critical value in a small area on the inner surface. Although the Ayada-m and MC models initially indicate damage initiation on the outside during the process, the damage subsequently exceeds the critical value on both the outside and inside surfaces.

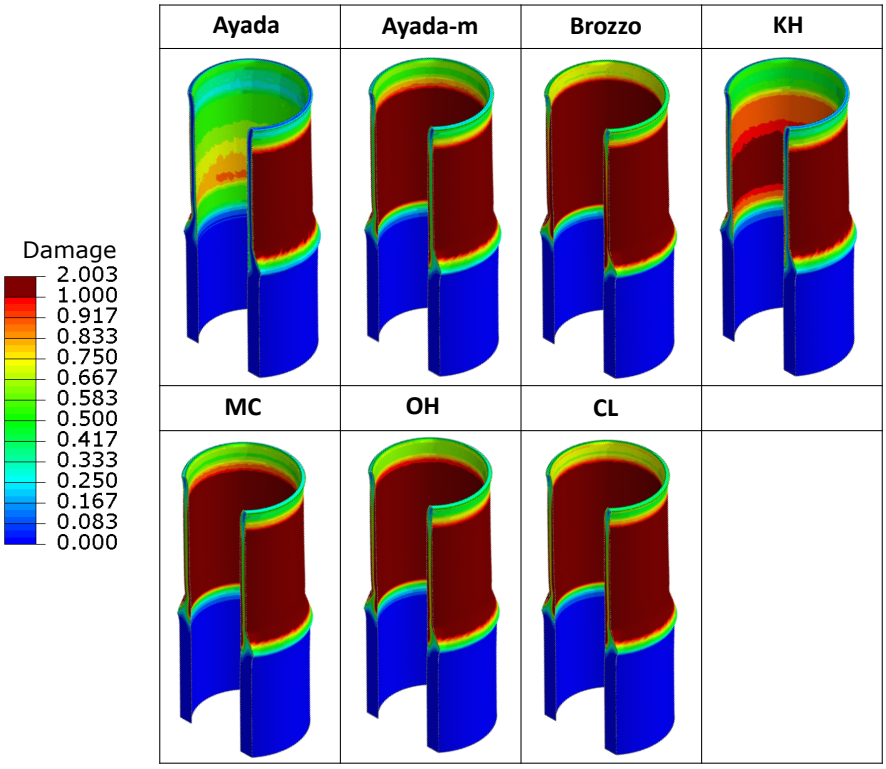

Figure 5.2: Numerical comparison of flow forming results of single parameter damage models with 50% thickness reduction.

In the Ayada-m and MC models, damage accumulation reaches high values of 2.233 and 2.395, respectively. On the other hand, the damage prediction of the Ayada model is consistent with experimental observations, showing damage on the outer surface of the formed part. While Ayada ve KH models predict a damage value of around 1.3 on the outer surface, their distributions on the inner surface differ. Ayada and KH models estimate damage values of 0.8 and 1.13 on the inner surface, respectively. Nevertheless, the Ayada model exhibits a more uniform and conservative damage distribution on the inner surface than the KH model. At 70% TR, fracture occurred at the start of the forming process, as shown in Figure 5.3. Simulation with the Ayada model shows a vast region with damage surpassing critical value inside and outside the specimen. Also, the small formed region has taken an oval shape with a significant increase in out-of-roundness.

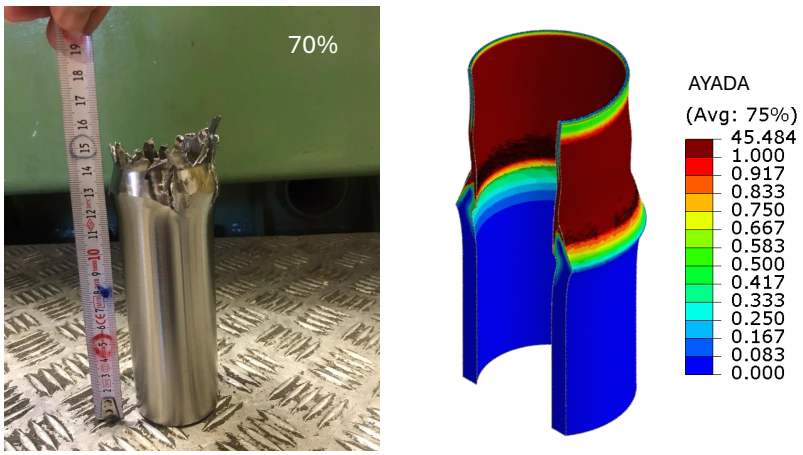

Figure 5.3: Experimental and numerical comparison of flow forming results with 70% thickness reduction.

In order to examine the damage evolution, equivalent plastic strain and damage parameter results are taken from 4 different elements shown in Figure 5.4. Elements 1 and 3 are on the outer surface (in contact with rollers), while elements 2 and 4 are on the inner surface (in contact with mandrel). Element positions are selected based on critical locations. Elements 1 and 2 are the outer and inner elements along the path where the damage value first reaches the critical value. Elements 3 and 4 are the outer and inner surface elements where the equivalent plastic strain is at its maximum and where damage models typically predict failure on the inner surface.

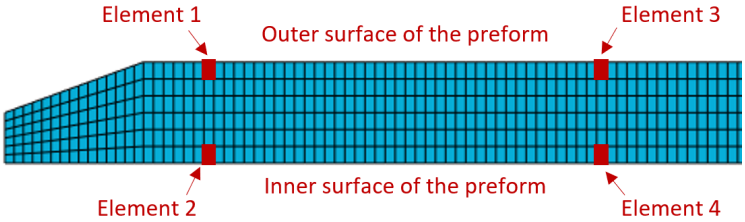

Figure 5.4: The critical elements are shown with the red box for two different paths.

Figure 5.5 shows the relationship between damage (D) and equivalent plastic strain (PEEQ) for single parameter damage models taken from inner and outer elements in two different places. The comparison includes CL, Ayada, Ayada-m, Brozzo, KH, MC and OH damage models. Other models with significantly high damage accumulation are not included in the graph.

All elements exhibit a gradual increase in damage with increasing plastic strain. The outer elements show a higher damage accumulation than the inner elements for all models. In elements 1 and 2, especially in OH and MC models, the damage accumulation is very high, while Ayada and KH models have a relatively lower damage accumulation trend. This trend is more clearly seen in the inner element. Elements 3 and 4 also show a similar trend of increasing damage with plastic strain. The damage accumulation rates of the models in these elements are higher than those in elements 1 and 2, especially for the inner element. This is because the equivalent plastic strain value in elements 3 and 4 is higher than in the other two elements at the same solution time.

5.1.2 Comparison of Multiple Parameter Damage Models

In this part, a comparison has been made for seven different multiple-parameter models. Flow forming analyses have been conducted for the Oyane-Sato, Johnson-Cook, Bai-Wierzbicki (BW), modified Mohr-Coulomb (MMC), DF2013, DF2014, and DF2015 models. Results are presented for reduction ratios of 37.5% and 50%. The results for 70% are not shown here, as none of the models in this section could make successful predictions at the 50% reduction ratio. Figures 5.6 and 5.7 provide

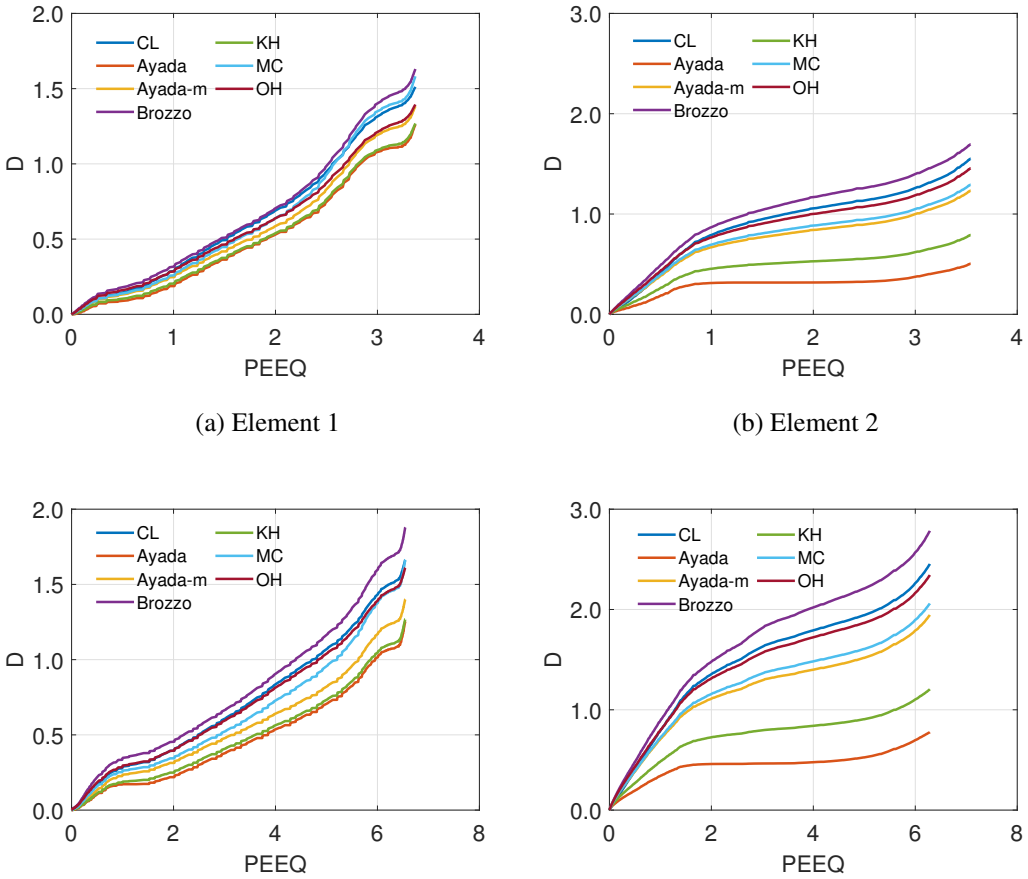

(a) Element 1

(b) Element 2

(c) Element 3

(d) Element 4

Figure 5.5: Damage (D) versus equivalent plastic strain (PEEQ) curves for single parameter damage models.

a numerical comparison of flow forming results using multi-parameter damage models at different thickness reductions. Figure 5.6 illustrates the damage distribution for 37.5% thickness reduction in various models: Oyane-Sato, JC (Johnson-Cook), BW (Bai-Wierzbicki), MMC, DF2013, DF2014 and DF2015. While the Oyane-Sato model shows moderate damage primarily near the inner surface and middle sections with a value of 0.833, the JC model predicts localized damage accumulation near the inner surface with a value of 1.054. The BW and MMC models predict severe damage, indicating almost complete failure of the tube. While the damage accumulation in the BW model is significantly higher than the critical value, the MMC model shows damage accumulation around 1.67. Models DF2013, DF2014, and DF2015 display varying degrees of damage; DF2014 and DF2015 show slightly higher damage accu-

mulation than DF2013 but still predict more damage than the MMC model.

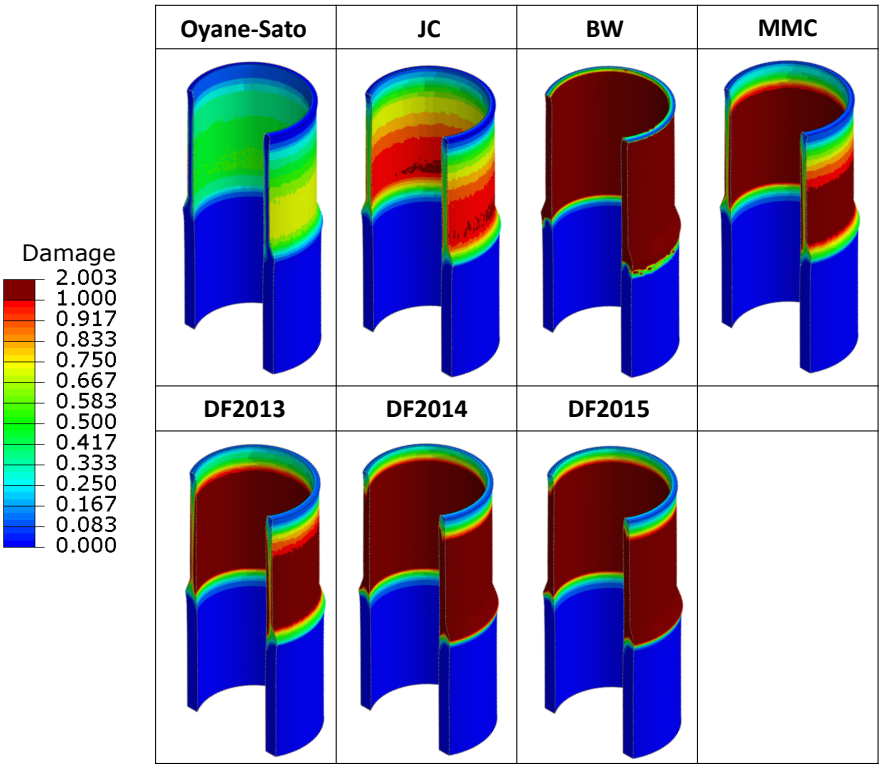

Figure 5.6: Numerical comparison of flow forming results of multiple parameters damage models with 37.5% thickness reduction .

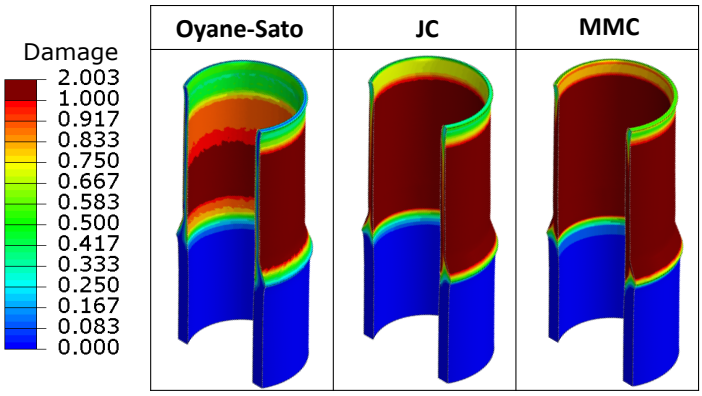

Figure 5.7: Numerical comparison of flow forming results of multiple parameters damage models with 50% thickness reduction.

Figure 5.7 shows the damage distribution for 50% thickness reduction comparing Oyane-Sato, JC and MMC models. Oyane-Sato model again shows moderate damage to the inner surface and near the middle sections. JC model shows more significant damage than the 37.5% reduction case, while the MMC model indicates very high damage, similar to the previous reduction case, predicting extensive damage and possible failure. These comparisons illustrate that different damage models predict varying degrees of damage accumulation during flow forming. BW and MMC models show higher levels of damage, whereas the Oyane-Sato model predicts more moderate levels of damage and provides an appropriate damage model based on the specific forming process requirements and conditions.

Figure 5.8 illustrates the relationship between damage (D) and equivalent plastic strain (PEEQ) for multi-parameter damage models taken from the inner and outer elements in two different places (see Figure 5.4). The comparison includes Oyane-Sato, JC, MMC and DF2013 damage models. Since the damage accumulation in the other models is very high, it is not included in the graph. As seen in this figure, the damage accumulation rates of the damage models are quite different. In the multi-parameter models, only Oyane-Sato could reach the experimental results. When comparing the damage evolution in single-parameter models to that in multiple-parameter models, the multiple-parameter damage models show higher damage accumulation. This can be attributed to the significant increases in equivalent plastic strain and the fluctuations in stress triaxiality and Lode parameter.

5.1.3 Comparison of Forming Distance

Figure 5.9 compares the forming distances achieved by different damage models at a 37.5% thickness reduction ratio. The figure highlights the moments when each model reaches its critical damage value, underlining the varying performance across different modeling approaches. The target forming distance is 26 mm, but none of the models reach this target except Ayada, Ayada-m, Oyane-Sato, MC and KH. The Johnson-Cook (JC) and OH models achieve the highest forming distances of 20 mm and 21 mm, respectively, coming closest to the target. The Brozzo and CL models also perform reasonably well, forming 15 mm and 18 mm distances. Interestingly,

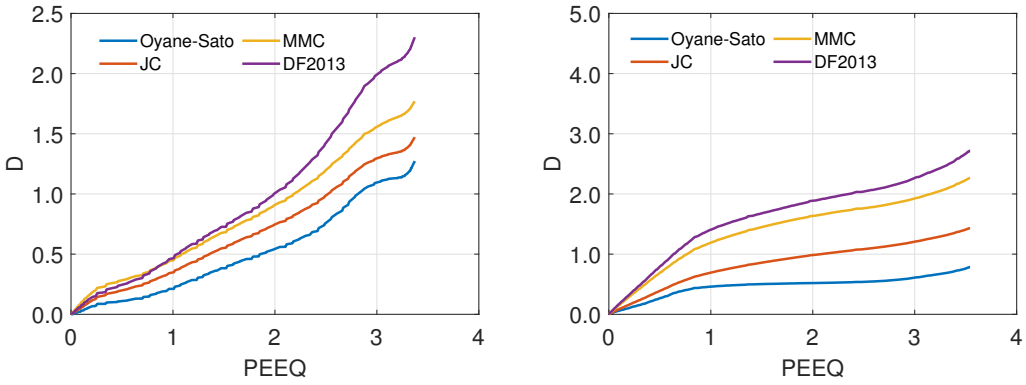

(a) Element 1

(b) Element 2

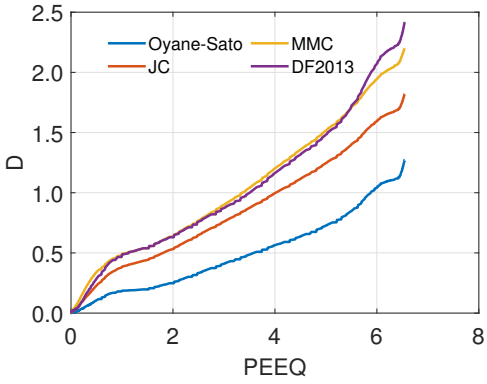

(c) Element 3

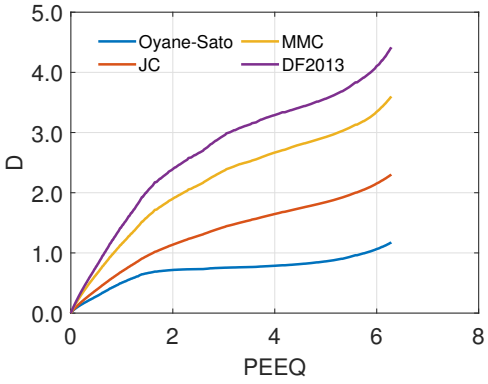

(d) Element 4

Figure 5.8: Damage (D) versus equivalent plastic strain (PEEQ) curves for multiple parameters damage models.

models like MMC and DF2013, which performed well in tensile tests, show poor performance here, each achieving only 8 mm. The Freudenthal and LR models show the worst performance, reaching only 0.5 mm and 1 mm, respectively. The models in the top row show a relatively better ability to approach the target forming length, while the others fall significantly short.

Figure 5.10 presents the forming distances achieved by different damage models at a 50% thickness reduction ratio. Here, the damage distributions are depicted when the first critical value is reached and when the initial fracture is observed on the inner surface. The five models presented here achieved the target forming distance at a 37.5% reduction ratio. The Ayada model stands out by achieving the target forming

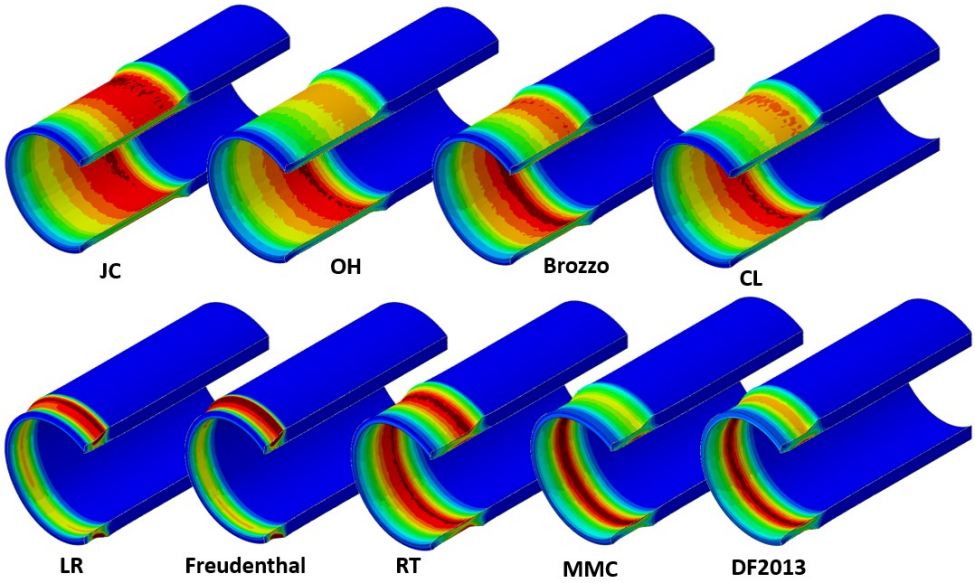

Figure 5.9: Damage distribution of flow forming results of damage models with 37.5% thickness reduction for forming distance comparison.

length of 26 mm, with no significant damage accumulation on the inner surface. This result indicates that the Ayada model effectively managed the damage throughout the process. The KH and Oyane-Sato models performed moderately well, achieving forming distances of 16 mm and 17 mm, respectively. However, they did not reach the target length, and some damage accumulation is noted on the inner surfaces. In contrast, the Ayada-m and MC models performed poorly, forming distances of only 7 mm and 6 mm, respectively. These models quickly concentrated damage on the inner surface, leading to early failure. Despite reaching the first critical value nearly simultaneously as the other models, their ability to manage the damage and achieve longer forming distances is significantly different.

Single-parameter models have proven more effective in predicting failure locations among all the models compared. Although multiple-parameter models performed well in tensile tests, they are less successful in predicting failure during the flow forming process. The MMC and similar failure criteria, calibrated with tensile experiments using different geometries, have been shown to overpredict damage accumulation significantly in shear forming [86] and single point incremental forming [122, 123] as demonstrated here for flow forming as well. This issue has been discussed as related to the change in loading history during incremental forming processes, which is rel-

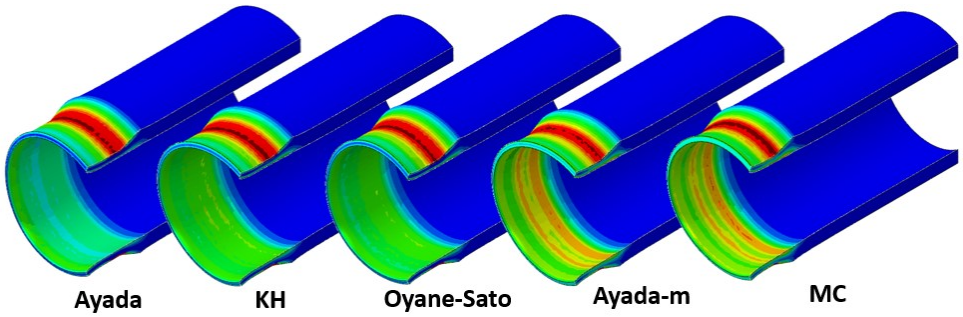

(a) The first moment when the damage reaches a critical value.

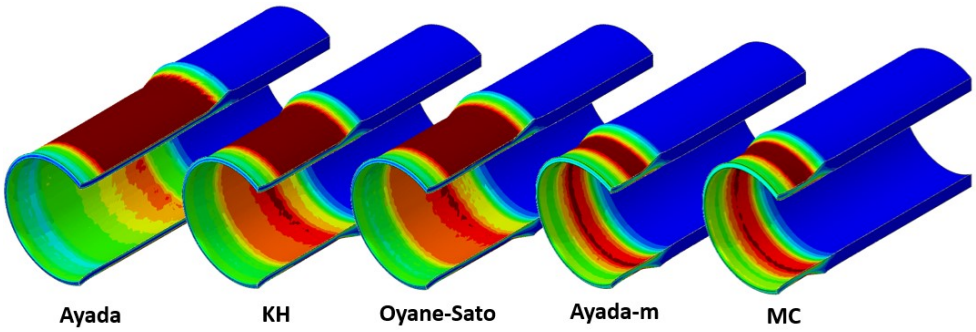

(b) The moment when the damage value reaches the critical value on the inner surface.

Figure 5.10: Damage distribution of flow forming results of damage models with 50% thickness reduction for forming distance comparison.

atively constant in tensile experiments. Non-linear damage accumulation rules (e.g. [124, 125]) have been proposed to solve this issue; however, calibrating the damage accumulation rule requires additional experiments with non-proportional loading histories. Furthermore, the calibration procedure is not as straightforward as done for the linear damage accumulation rule, and an additional parameter is required to measure the non-proportionality of the loading.

5.2 Process Parameter Effect on Flow Forming for IN718

In this section, the results from the flow forming tests and FE simulations of IN718 are presented and discussed in detail. FE analysis uses the same process parameters in the flow forming experiments section. The results obtained in this section have been compared with the experimental findings shown in Figures 4.3 and 4.4. It is

observed that the forming process can be completed at 37.5 and 50% TR ratio while complete fracture of the part occurs at 70% reduction. Cracks are observed at the outer surface of the specimen at 50% TR, and they occur all over the formed portion, and they occur distinctly in the radial direction while the inner surface is defect-free.

5.2.1 Effect of Increasing Feed Rate in Fixed Feed Ratio

Since a parametric study is aimed, solution time is critical, and in forming studies, process speeds are often adjusted to shorten solution times. Figure 5.12 shows the effect of different feed rates on the damage distribution at a constant revolution speed-feed rate ratio for the Ayada, KH and Oyane-Sato criteria. The data are extracted from the element integration points of two paths through the thickness where 0 mm point refers to the outer surface, and 4.12 mm is the inner surface in contact with the mandrel (see Figure 5.11). These two paths are specifically selected. The first path is determined as the path where the damage value reaches the first critical value. The second path is defined as the path where the equivalent plastic strain is maximum and where damage models usually predict fracture on the inner surface.

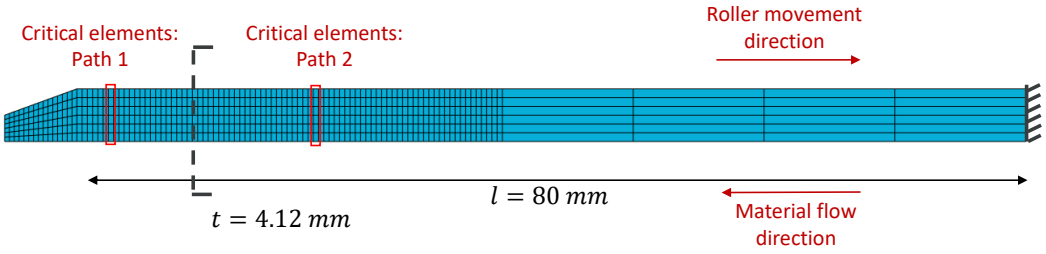

Figure 5.11: The location of the element outputs are shown with the red box.

Changing the feed rate while keeping the rate constant does not significantly affect the damage distribution. Data from the Ayada, KH, and Oyane-Sato models show that damage accumulation decreases with increasing feed rate due to the increasing plastic strain. When the critical analyses at 1 mm/s and 2 mm/s speeds are compared, similar damage accumulation is observed on the inner surface at experimental speeds. In contrast, a slightly lower damage accumulation is noted on the outer surface at 2 mm/s speed.

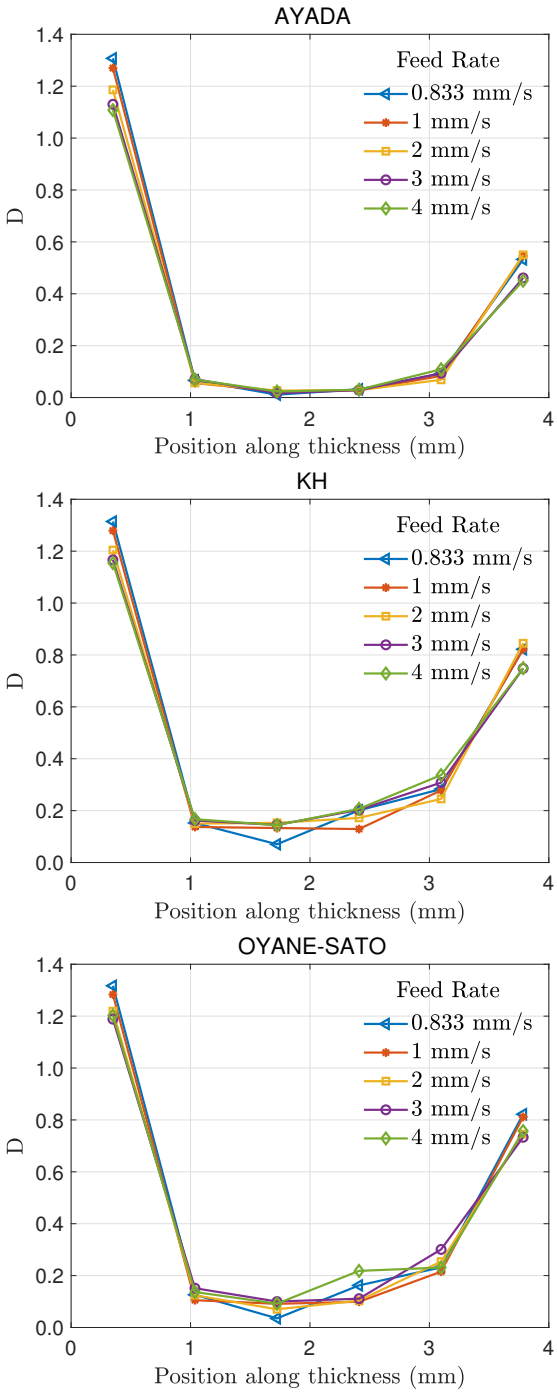

Figure 5.12: The effect of different feed rates in same ratio on damage distribution for Ayada (top), KH (middle) and Oyane-Sato (bottom) criteria.

There are changes in PEEQ, temperature, and damage location at different feed rates, aside from von Mises stress in the overall distribution in the tube. First, in this comparison, the von Mises stress values are almost the same except when the feed rate is

4 mm/s. For PEEQ, values significantly increase as the feed rate increases. The high plastic strain has a negative effect on forming, so working between maximum values of 6-7 is vital for both damage values and formability. Therefore, 3 and 4 mm/s feed rates are unsuitable for parametric studies due to the enormous plastic strain. Compared to the other three feed rates, the feed rate of 2 mm/s is very advantageous regarding solution time because the solution time is 3 times less than at experimental speeds. Analyses take an average of 9 days at 0.833 feed rate, 6 days at 1 mm/s, and 3 days at 2 mm/s.

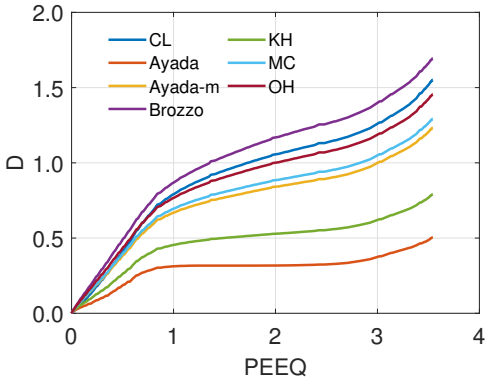

(a) Element 2 - Feed rate is 0.833 mm/s

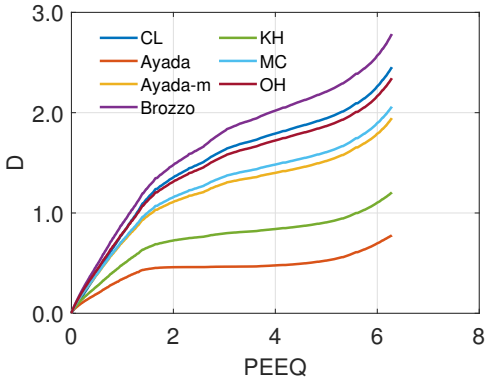

(b) Element 4 - Feed rate is 0.833 mm/s

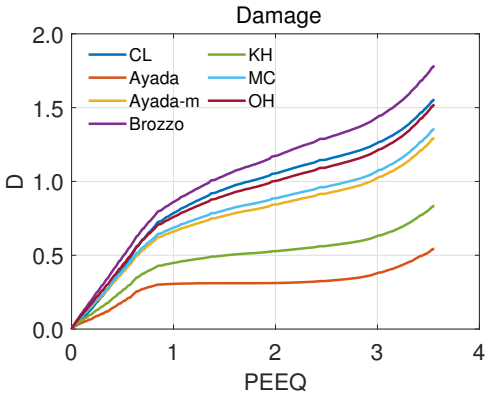

(c) Element 2 - Feed rate is 2 mm/s

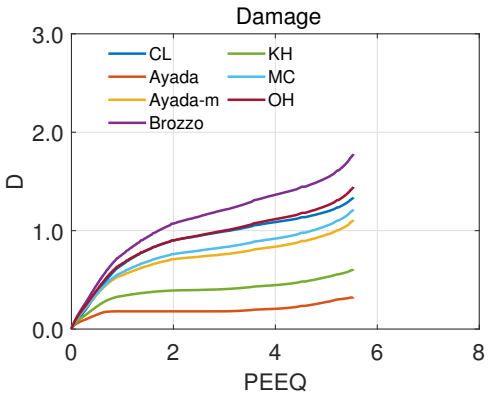

(d) Element 4 - Feed rate is 2 mm/s

Figure 5.13: Comparison of damage (D) with equivalent plastic strain (PEEQ) at varying feed rates.

The graphs shown in Figure 5.13 demonstrate the damage evolution in the inner element of Path 1 and Path 2 obtained at 0.833 mm/s and 2 mm/s feed rates. The damage accumulation and equivalent plastic strain values in Path 2 are quite different between

the two feed rates. However, when Path 1 is examined, it is seen that the two feed rates have very close damage evolution. Since working at experimental speeds triples the solution time and working at experimental speeds would be inefficient for doing parametric work, the comparisons at the beginning of this section are made with the results obtained at experimental speeds. In contrast, a feed rate of 2 mm/s and a rotation speed of 300 rpm are used for the parametric work. In addition, all comparisons are made with the results obtained from Path 1 to ensure consistency.

Finally, there are differences between feed rates in location estimates of damage accumulation. While only the Ayada model matched the experimental results for damage location prediction in the general distribution, the KH and Oyane-Sato models predicted regional cracks on the inner surface at the experimental speeds. Since the damage values predicted by these two models are very close to the critical value, they are promising in terms of damage prediction in this process.

5.2.2 Effect of Temperature Dependency

The effect of including temperature in FE analysis is depicted in Figure 5.14. In model 1, no temperature dependency is considered in FE analysis, while in model 2, simulation is conducted using a fully temperature-displacement coupled approach with the CL model, as explained before. Data are extracted from element integration points in Path 1 shown in Figure 5.11. It can be observed that both models predict higher damage accumulation on the outer surface of the formed part. The results also show increased accumulated plastic strain throughout the thickness due to thermal softening in the material. The damage increases slightly at the outer and inner surfaces while remaining unchanged inside the part. Modeling of thermal effect could be essential to increase prediction accuracy with the simulation of flow forming utilizing the FE method.

5.2.3 Effect of Feed Ratio

Figure 5.15 depicts the variation of damage with changing feed ratio, the ratio of revolution speed to feed rate, at the inner and outer surfaces of the specimen predicted

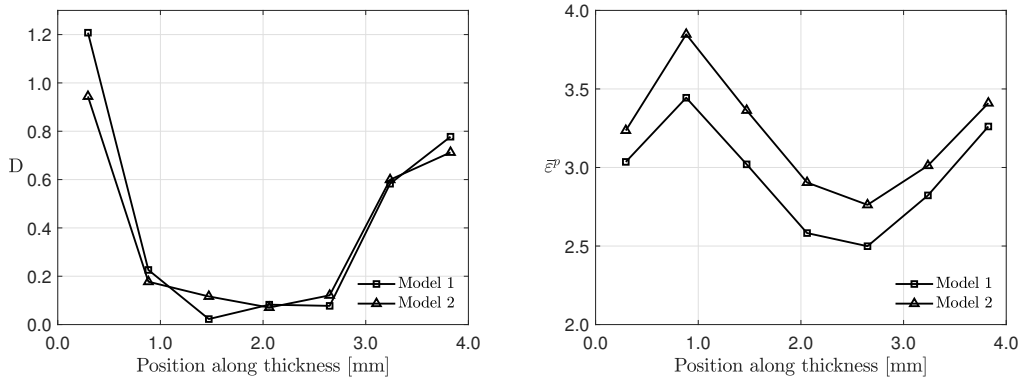

(a) (b)

Figure 5.14: Comparison of model 1 and 2. Distribution of (a) damage and (b) plastic strain through the thickness of the specimen.

by the Ayada and KH models. This ratio governs the roller's helical path around the preform and is an important design parameter for flow forming or spinning processes. A 150 [rpm/mm/s] feed ratio corresponds to the value of the experimental work. The Ayada model shows that damage to the outer element generally increases with higher rotational speeds and feed rates, peaking at around 225 rpm/mm/s. In contrast, the inner element exhibits relatively stable damage levels with a slight decrease of around 150 rpm/mm/s. Similarly, the KH model shows increased damage to the outer element with increasing rotational speeds and feed rates, peaking at around 225 rpm/mm/s. However, the internal element provides a more consistent level of damage at different speeds and rates, showing a slight reduction at 150 rpm/mm/s. The Ayada and KH models predict very similar behavior with varying ratios. Only the KH model calculates a higher damage value on the inner surface than Ayada, but the trend is the same.

The plastic strain distribution in the tube shown in Figure 5.16 emphasizes the importance of the ratio. The results show that higher ratios (75 to 112.5 rpm/mm/s) lead to a significant plastic strain accumulation; higher PEEQ values are concentrated around the outer surface of the tube, which causes severe deformation and indicates an increased risk of material failure. Conversely, as the ratio increases from 150 rpm/mm/s to 300 rpm/mm/s, the PEEQ distribution becomes more uniform, and the

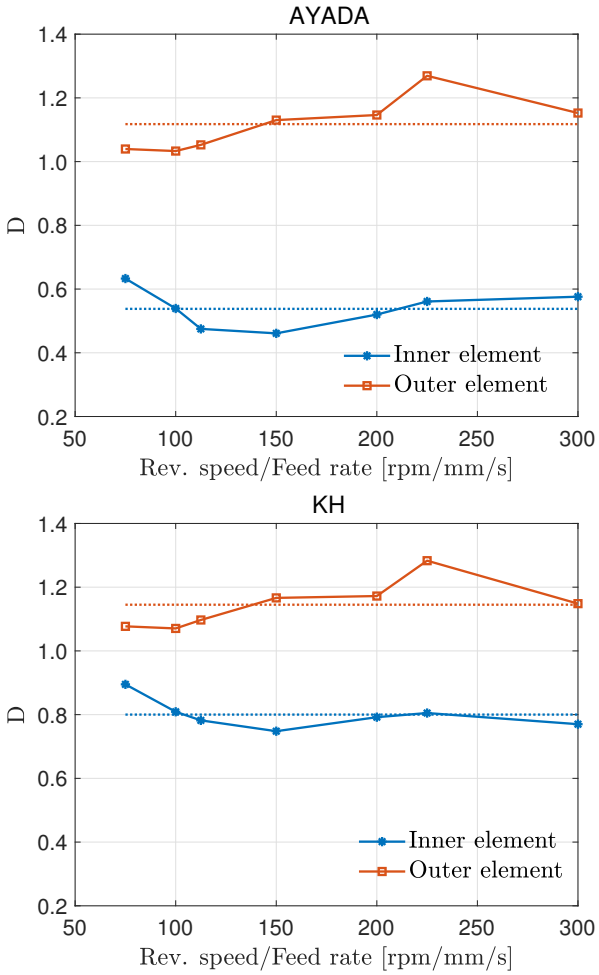

Figure 5.15: Change of damage predicted by the Ayada and KH models with respect to revolution speed/feed rate at inner and outer elements.

maximum PEEQ values decrease significantly. This result shows that greater ratios result in a more controlled deformation process with a better strain distribution and less possibility of local failure. Therefore, it is crucial to optimize the turnover rate in the flow forming process to improve material performance and structural integrity.

5.2.4 Effect of Feed Rate and Revolution Speed

The effect of feed rate and revolution speed on formability and temperature can further be investigated from Figure 5.17. The temperature and damage distributions of the Ayada model are shown in this figure. Simulations are performed at a constant revolution speed but increasing the feed rate. It can be seen that the temperature of

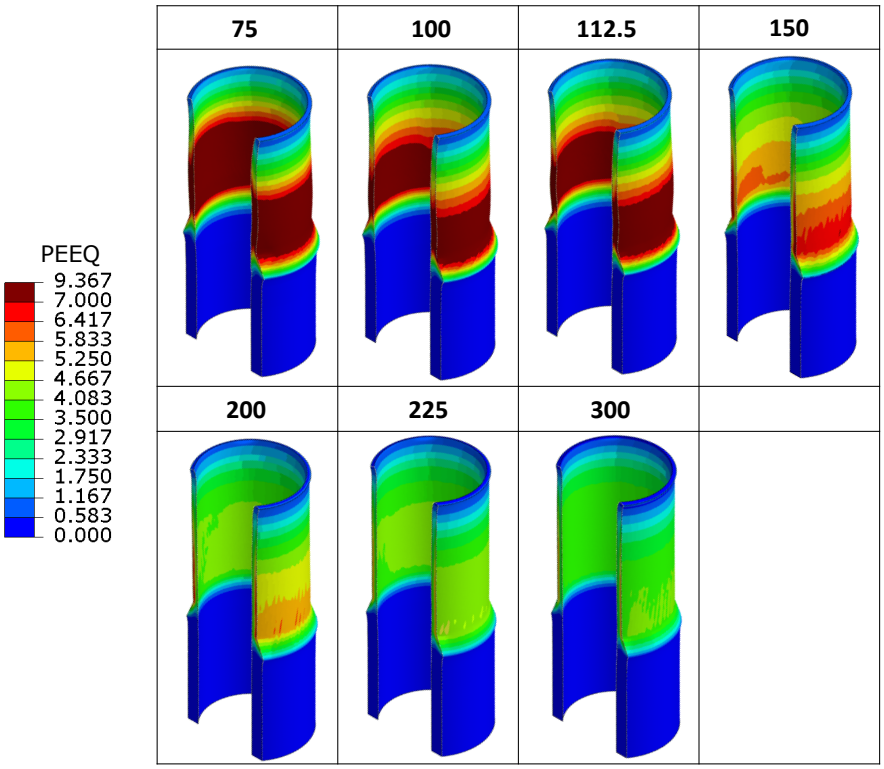

Figure 5.16: PEEQ distribution for different revolution speeds/feed rate (rpm/mm/s).

the part can surpass 1000°K in FE simulations in each case, and the temperatures are increased with increasing feed rate. As the feed rate increases, we observe a decrease and increase in accumulated damage while the maximum damaged region changes from the outer to the inner surface. On the other hand, increasing the revolution speed has a negligible effect on temperature distribution but results in increased damage. The highly damaged region is more dispersed as well.

Figure 5.18 shows how the equivalent plastic strain (PEEQ) varies through the thickness at a constant feed rate and revolution speed. Since uncoupled damage models are used in this study, the equivalent plastic strain is the same across all models. The graphs on the left show the effect of constant feed rate (2 mm/s, 3 mm/s, and 4 m/s) at different revolution speeds (300 rpm, 450 rpm, and 600 rpm). The graphs on the right show the effect of different feed rates (2 mm/s, 3 mm/s, and 4 mm/s) at a constant revolution speed (300 rpm, 450 rpm and 600 rpm). The analyses evaluate the effect of revolution rates and feed rates on the equivalent plastic strain, both at constant feed

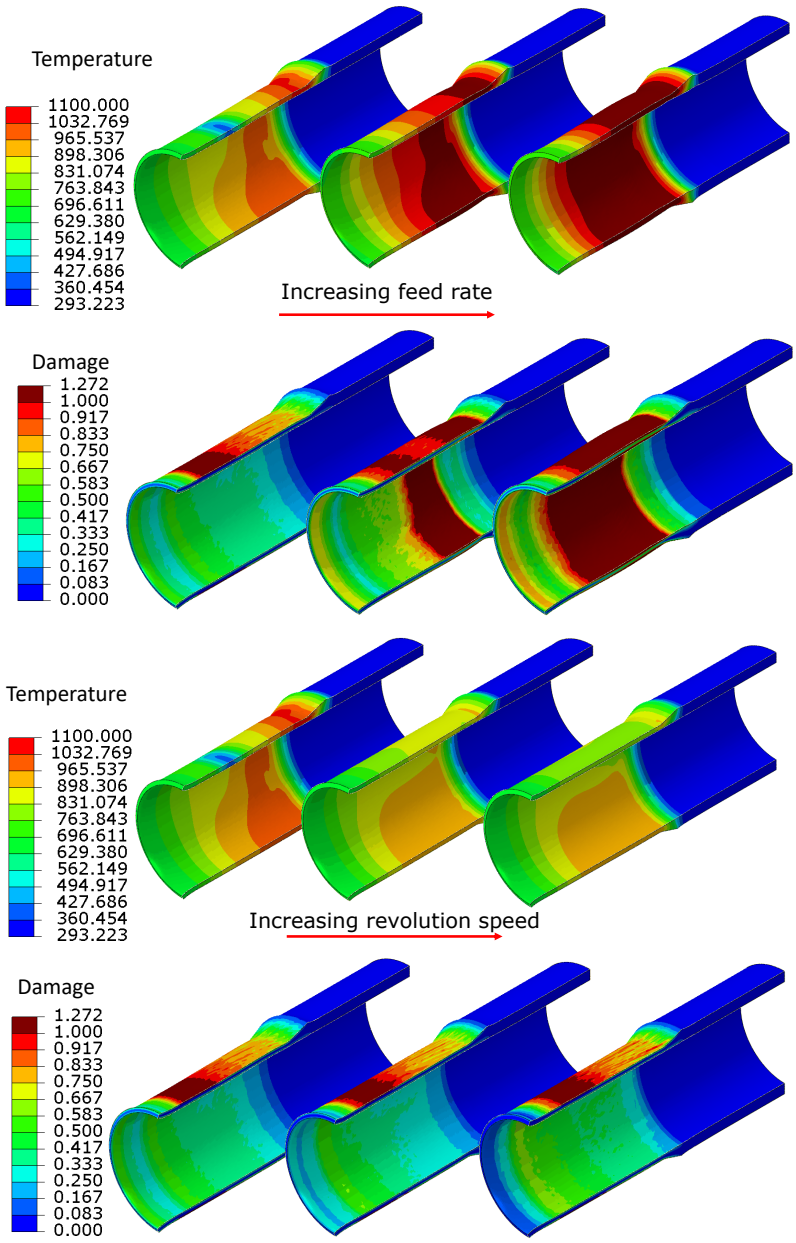

Figure 5.17: Contour plots of temperature (K) and total damage with increasing feed rate (constant revolution speed) and increasing revolution speed (constant feed rate).

rate and constant revolution rate. Significant differences are observed between equivalent plastic strain values from the outer surface to the inner surface. At constant feed rate (left graphs), plastic strain values are generally highest at a revolution speed of 300 rpm. These values decrease slightly at 450 and 600 rpm revolution speeds, except for the second element from the outer surface. As the feed rate increases, the change in plastic strain values at different revolution speed values is less than the low feed

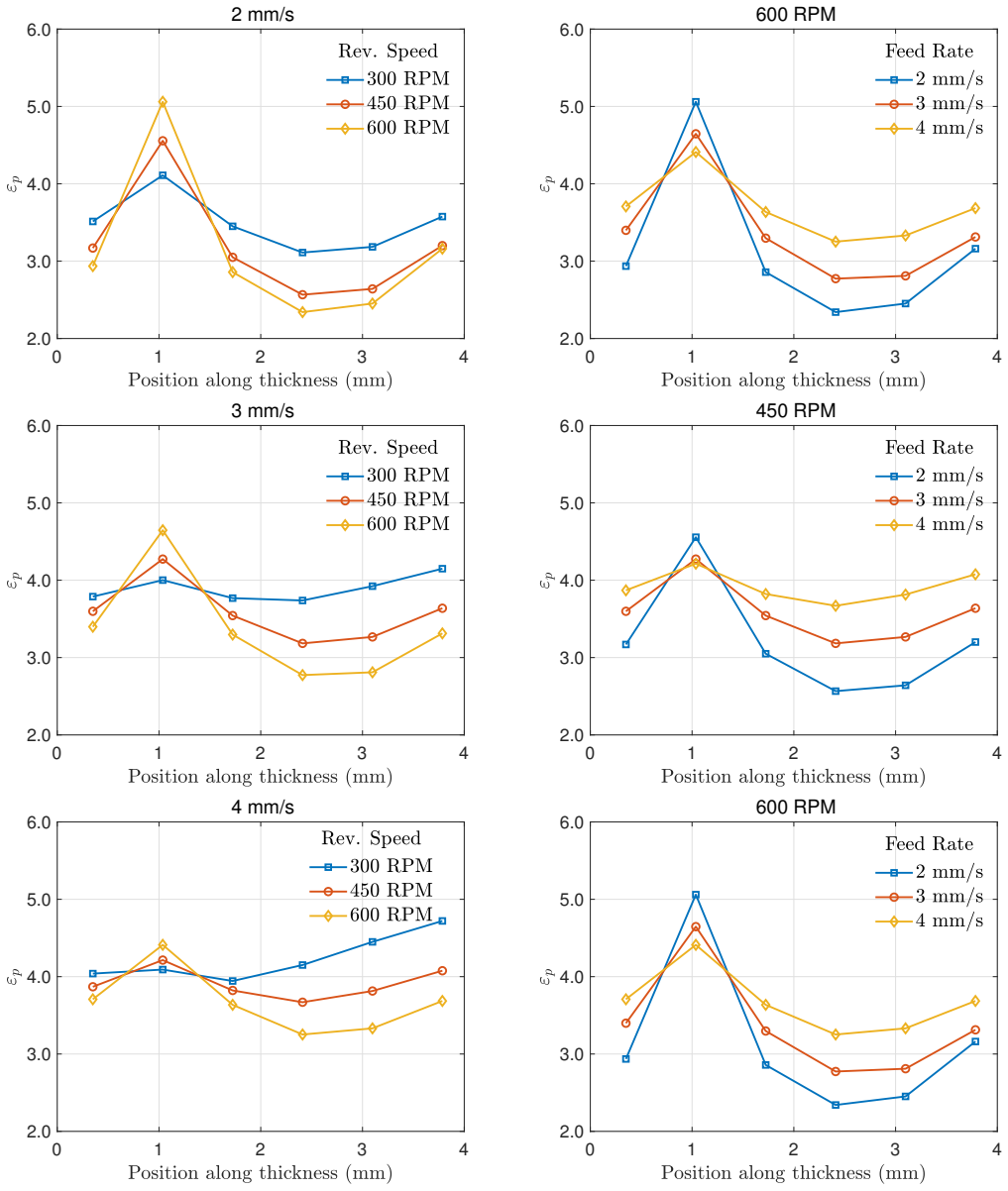

(a) Fixed feed rate

(b) Fixed revolution speed

Figure 5.18: The variation of equivalent plastic strain along the thickness of the preform under fixed feed rate and fixed revolution speed.

rate value. In other words, as the feed rate increases, the plastic strain distribution throughout the thickness becomes more uniform.

At constant revolution speed (right graphs), a significant increase in equivalent plastic strain values is observed with increasing feed rate. In particular, the 4 mm/s feed

rate has higher plastic strain values than the 2 mm/s and 3 mm/s speeds, except for the second element from the outer surface. This shows that higher feed rates cause more deformation of the material. In both cases, when examining the distribution of equivalent plastic strain along the thickness, it is observed that the plastic strain distribution is generally equal on the inner and outer surfaces. However, as it moves from the outer to the inner surface, there is some fluctuation in the plastic strain values. Notably, the second element from the outer surface often reaches the highest value. These results show that both revolution speed and feed rate significantly impact the equivalent plastic strain, and these parameters need to be optimized.

5.2.5 Effect of Thickness Reduction Ratio

Figure 5.19 shows how damage (D) and equivalent plastic strain (PEEQ) vary through-thickness for different thickness reduction ratios using the Ayada model. The upper graph shows the damage distribution throughout the thickness, and the lower graph shows the equivalent plastic strain distribution. As seen in the upper graph, as the reduction ratio increases, it is observed that the damage generally accumulates on the inner and outer surfaces. At 60% thickness reduction, damage values are quite high, up to 2.0, especially on the inner surface. As the reduction ratio decreases (60%, 50%, 40%, 30%, and 20%), the damage values decrease significantly and are more evenly distributed. Especially at 10% and 20% thickness reduction ratios, damage values are pretty low on the interior and exterior surfaces.

The lower graph shows how the equivalent plastic strain values vary through thickness. At 60% thickness reduction, plastic strain values increase to 7.0, which remain almost constant throughout the thickness. As the thickness reduction ratio decreases, plastic strain values generally decrease. At 10% and 20% reduction ratios, plastic strain values show a lower and more balanced distribution on the inner and outer surfaces. The 70% results are not included in these graphs because there are significant increases in damage and plastic strain values along with the 60% reduction. These results show that the thickness reduction rate significantly impacts both damage accumulation and plastic strain distribution. As can be understood from the obtained results, it can be said that the formability limit for this material, with the experimental

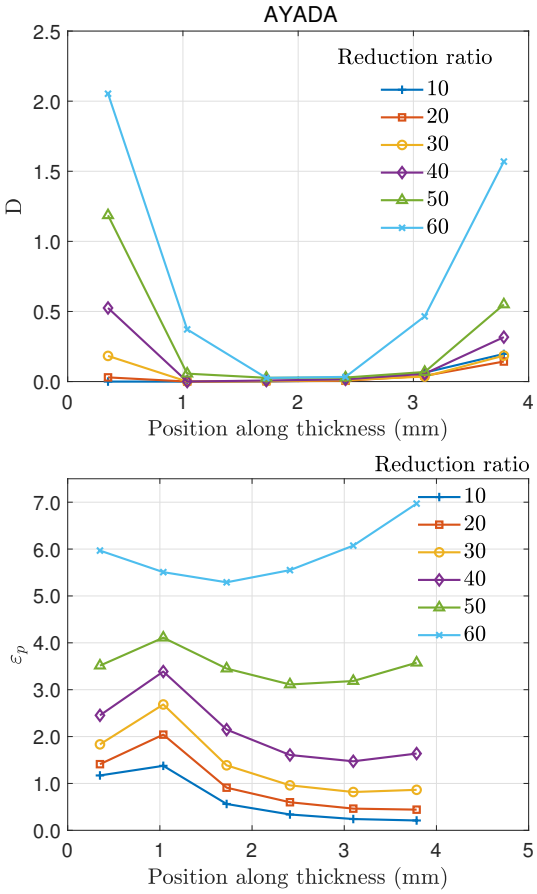

Figure 5.19: The variation of damage and equivalent plastic strain along the thickness for different thickness reduction ratios.

process parameters, is slightly below a reduction ratio of 50%. Therefore, selecting appropriate thickness reduction ratios is critical to achieve optimum forming performance.

In Figure 5.20, the comparison between the Ayada and KH models reveals that both models show similar trends in damage and plastic strain predictions for inner and outer elements. As the reduction ratio increases, an increase in damage and PEEQ values is observed in both models. Notably, the damage and plastic strain values on the outer surface are higher than those on the inner surface. This result shows that the stress accumulation on the outer surface is more significant, and the risk of fracture is higher in these areas. In the Ayada model, the damage values on the internal and external surfaces are at similar levels and show lower damage accumulation than in the KH model. These data demonstrate that damage and plastic strain distributions at

different reduction rates are critical for understanding the mechanical behavior of the modeled material and the usability of Ayada and KH models in such analyses.

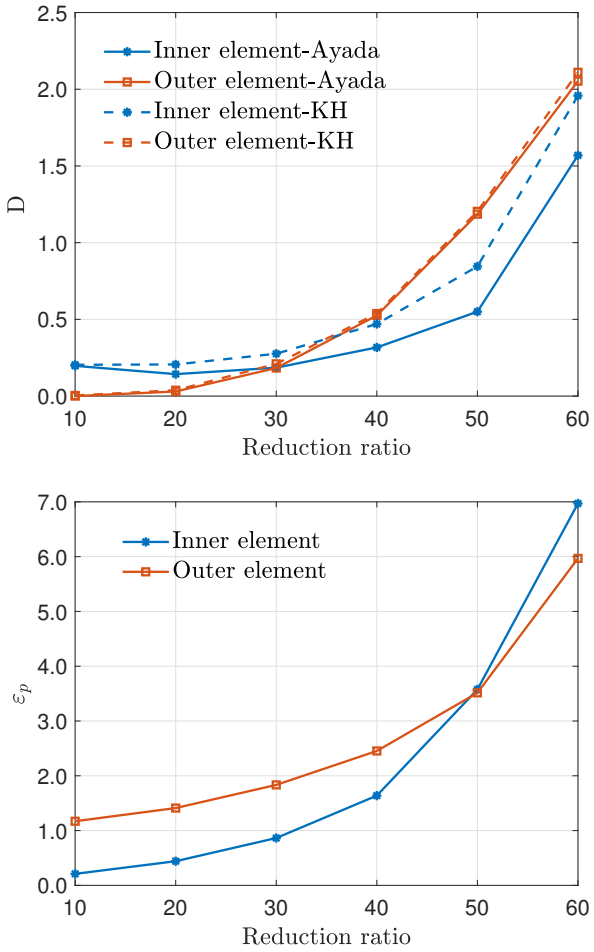

Figure 5.20: Comparison of various reduction ratios with Ayada and KH models. Distribution of damage and plastic strain in the inner and outer elements of the tube.

5.2.6 Effect of Radial and Axial Offset

The flow forming process is usually performed with axial and radial roller offsets or a multi-pass forming approach to increase formability (e.g. [81]). Another parametric study examines the effect of radial and axial offset values on plastic strain and damage. In this context, twelve additional FE analyses are performed with rollers with 1 mm, 3 mm, 5 mm, and 7 mm axial offsets and three radial offsets reaching 50% thickness reduction in three steps. The distribution of damage and plastic strain

through the thickness is shown in Figures 5.21 and 5.22. These simulations examine the effect of axial and radial offsets of the roller on the formability predicted by the Ayada model. Results for the KH and Oyane models are not included as their trends were similar.

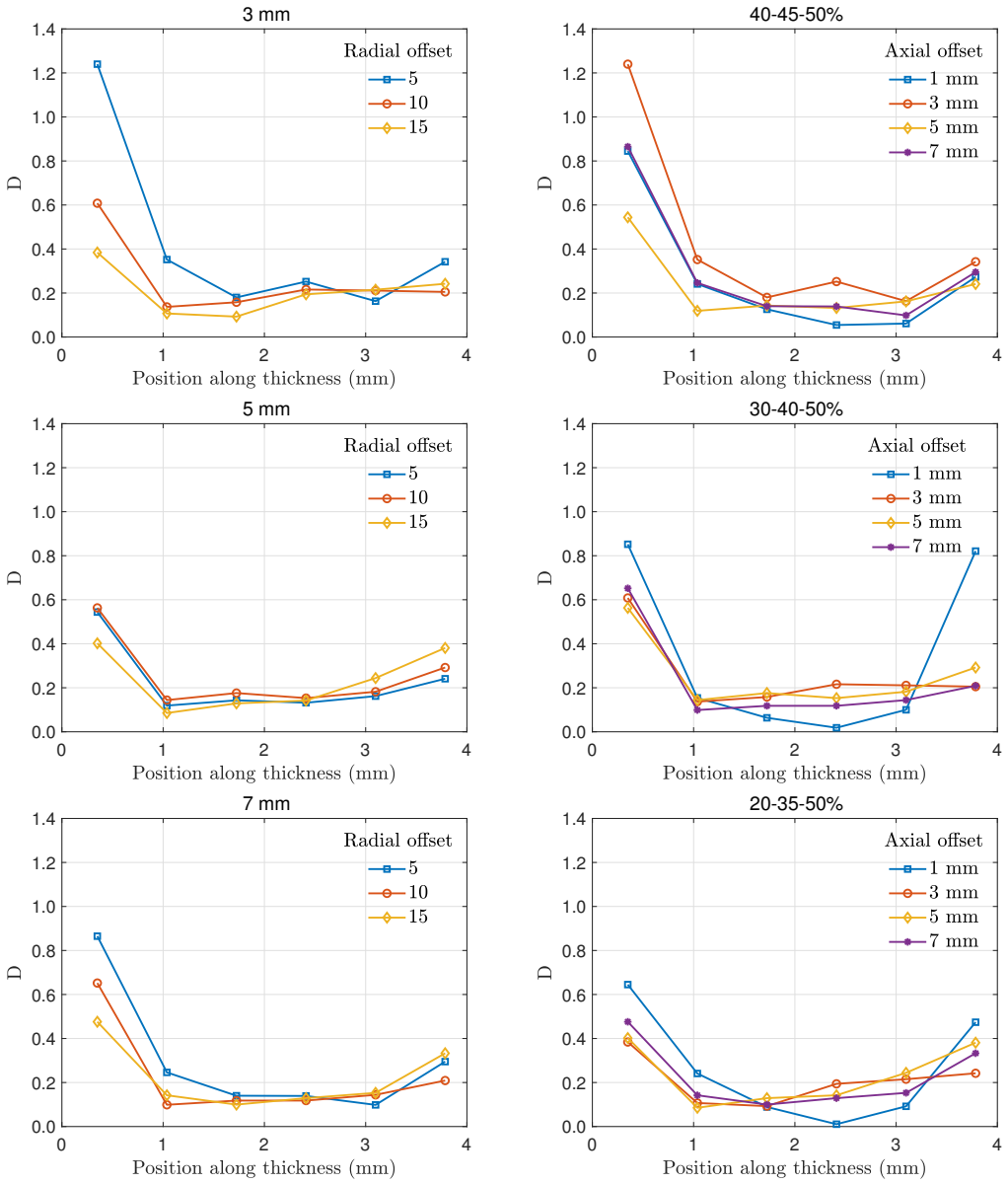

(a) Fixed axial offset

(b) Fixed radial offset

Figure 5.21: The variation of damage along the thickness of the preform under axial offsets and fixed radial offsets for the Ayada model.

Figure 5.21 shows the variation in damage distribution along the thickness of the

preform when axial and radial offsets are kept constant according to the Ayada model. In the graphs on the left, the effect of different radial offsets (5 (40-45-50%), 10 (30-40-50%), and 15 (20-35-50%)) on damage for fixed axial offset values (3 mm, 5 mm, and 7 mm) is examined. In the graphs on the right, different axial offsets (1 mm, 3 mm, 5 mm, and 7 mm) are shown for fixed radial offset values (40-45-50%, 30-40-50%, 20-35-50%). Graphs for 1 mm axial offset were not provided because, in this case, the part experiences high plastic strains, causing interruptions in the contact between the material and the mandrel in certain areas. Therefore, a graphical comparison would not be accurate.

At fixed axial offset values, it is observed that as the radial offset increases, the damage accumulation along the thickness generally significantly decreases. Particularly for the 15 (20-35-50%) radial offset value, the damage is reduced significantly on the outer surface for all axial offset values. Regarding the change in the inner surface, it can be said that a 10 (30-40-50%) radial offset predicts less damage than other radial offsets. The most notable result from the fixed axial offset findings is that the case with a 5 mm axial offset is almost independent of the radial offset values and is minimally affected.

As the axial offset increases, differences are observed in the damage values on the inner and outer surfaces at fixed radial offset values. There is an apparent decrease in damage accumulation with increasing radial offset. As the percentage difference between each roller's forming amount increases, a reduction in damage accumulation and an increase in formability are observed. Except for the 5 (40-45-50%) case, it can be said that 3 mm and 5 mm axial offsets predict the lowest damage value. This indicates that axial offsets significantly affect damage accumulation and that exceeding a specific offset value may cause the material to experience more damage. It can be seen that starting with a smaller TR and increasing the TR by equal amounts (20-35-50%) reduces overall accumulated damage. It is also not beneficial to apply a major part of the reduction at the start and the remaining amount in smaller steps (40-45-50%). These data highlight that axial and radial offsets significantly affect the damage distribution throughout the thickness of the preform and that these parameters need to be optimized. Determining optimum offset values can improve the material's performance and reduce the failure risk.

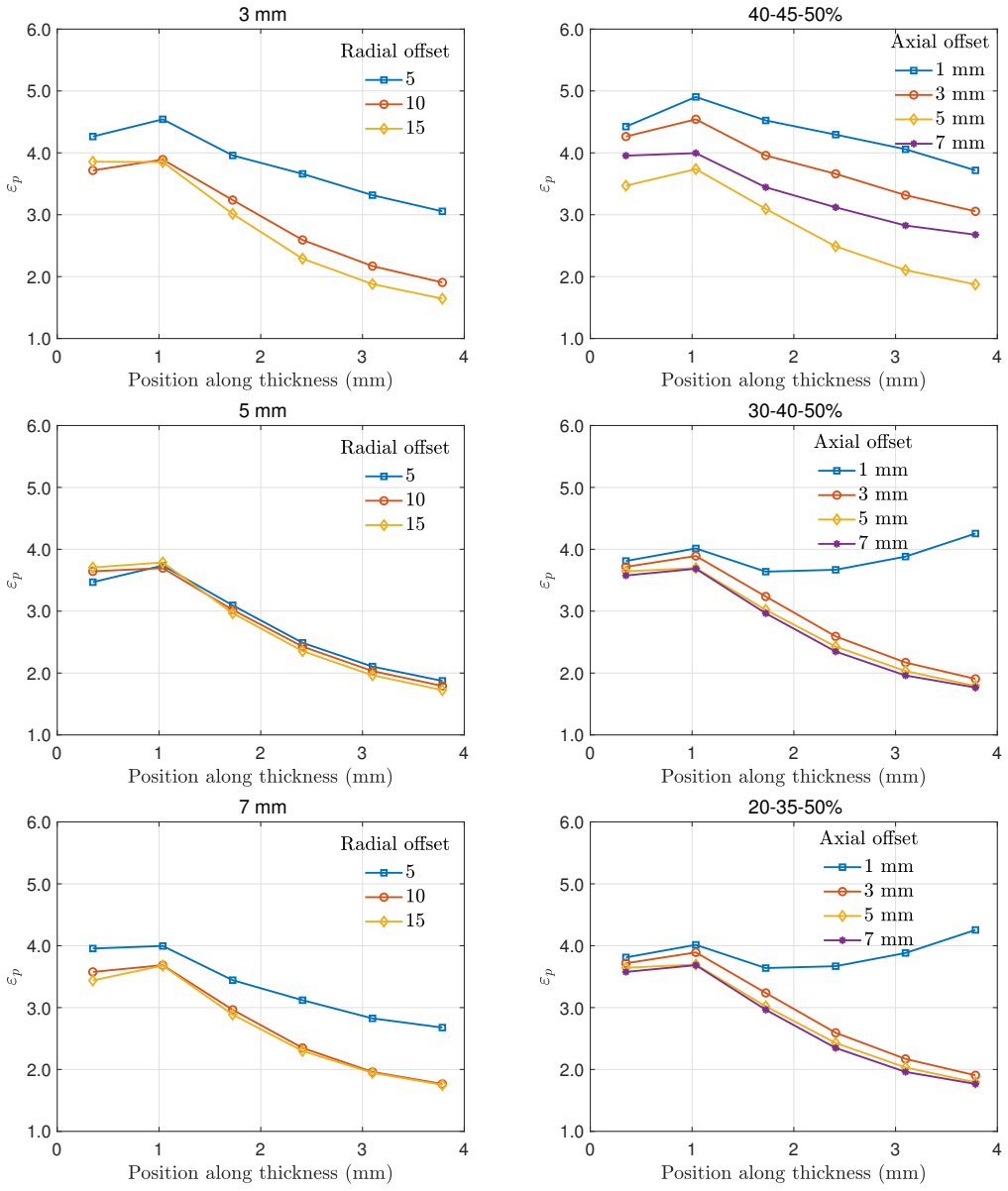

(a) Fixed axial offset

(b) Fixed radial offset

Figure 5.22: The variation of equivalent plastic strain along the thickness of the preform under axial offsets and fixed radial offsets.

Figure 5.22 shows the change of equivalent plastic strain along the thickness of the preform when axial and radial offsets are kept constant according to the Ayada model. In the graphs on the left, for fixed axial offset values (1 mm, 3 mm, 5 mm, and 7 mm), different radial offsets (5 (40-45-50%), 10 (30-40-50%), and 15 (20-35-50%)) on the equivalent plastic strain are studied. In the graphs on the right, different axial offsets

(1 mm, 3 mm, 5 mm, and 7 mm) are shown for fixed radial offset values (40-45-50%, 30-40-50%, 20-35-50%).

As the radial offset increases, a significant decrease in equivalent plastic strain values is observed at fixed axial offset values. Mainly, in 3 mm and 7 mm axial offsets, the strain values obtained with a radial offset value of 5 (40-45-50%) are higher than other radial offsets. This indicates that lower radial offsets lead to greater plastic deformation in the material. At fixed radial offset values, decreases in equivalent plastic strain values are observed as the axial offset increases. The equivalent plastic strain at higher levels at 1 mm axial offset value is lower at 7 mm axial offset value. This suggests that higher axial offsets can reduce material deformation but could also affect damage accumulation.

Overall, both axial and radial offsets significantly affect the distribution of equivalent plastic strain along the thickness of the preform. Determining the optimal offset values can enhance the efficiency of the forming process by controlling material plastic deformation and minimizing unwanted deformations.

5.3 Hardening Rule Effect on Flow Forming for IN718

The plastic behavior of the material is modeled using experimental plastic true stress-strain data. However, strain data obtained from experiments are limited and insufficient to model plasticity behavior in processes such as flow forming involving high plastic strain. Uniaxial tensile tests are a commonly used test type in both literature and industry, and material modeling is performed using the data obtained from these tests. Through these tests, various hardening rules such as Power, Swift, Voce, and Johnson-Cook (JC) are used to model plastic behavior beyond experimental strain values. In addition, higher plastic strain values can be achieved through various tests. In the tests conducted for DP600, while a plastic strain is around 0.2 in the uniaxial tensile test, values of 0.9 can be reached with the in-plane torsion test, 0.72 with the plane strain compression test, and 0.65 with the hydraulic bulge test, levels not attainable with uniaxial tensile tests [126]. However, the use of the mentioned hardening rules remains necessary to model the plastic behavior in processes like metal forming,

where high amounts of plastic strain are reached.

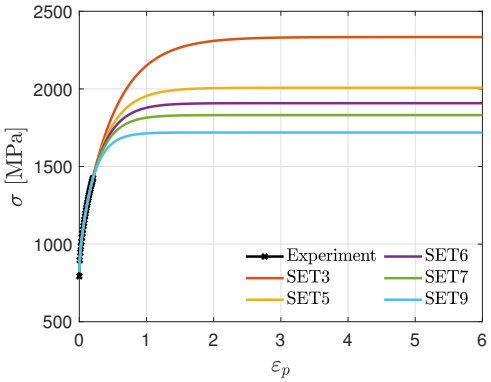

(a) Voce rule

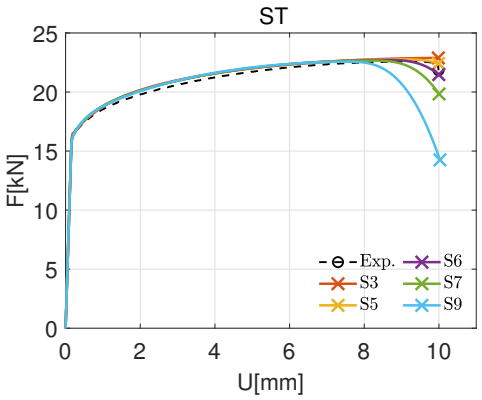

(b) Voce rule

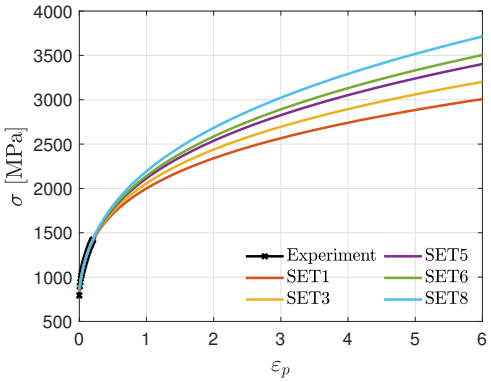

(c) Swift rule

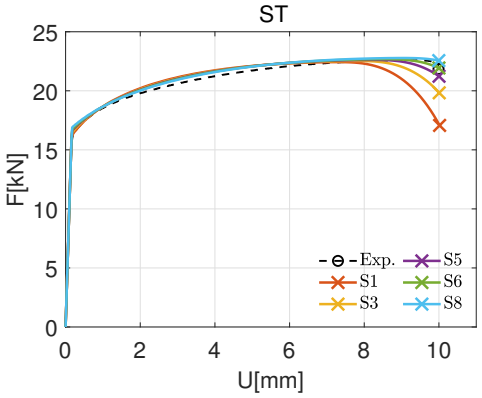

(d) Swift rule

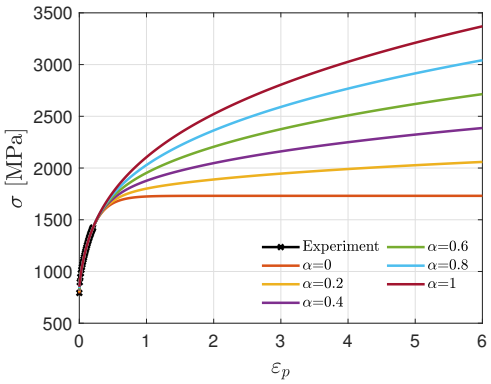

(e) Modulated

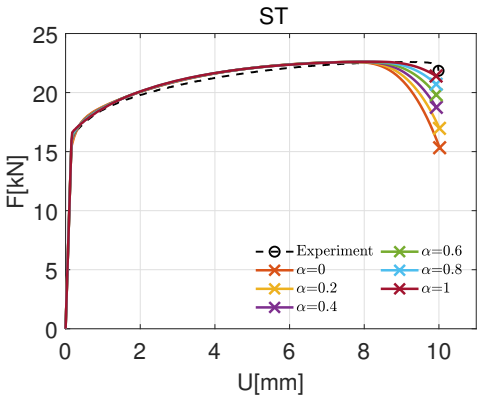

(f) Modulated

Figure 5.23: Stress-strain and force-displacement curves for three different hardening rules (Voce, Swift and modulated), using various parameter sets.

In complex processes such as flow forming, plasticity can be modeled with these rules, but the stress values obtained from the rules modeled with the same plastic data may be quite different. In other words, even if these models fit the same experimental data, they exhibit different stress states, significantly affecting the process's plastic behavior and, therefore, the damage prediction. For example, using various parameter sets, Figure 5.23 shows the stress-strain and force-displacement curves for three hardening rules (Voce, Swift, and modulated). The comparison highlights how each hardening rule predicts significantly different behavior under high-strain conditions typical of flow forming while providing an excellent fit to the initial experimental data. This discrepancy highlights the importance of choosing an appropriate hardening rule to model plasticity and accurately predict damage in high-strain processes.

This section investigates the effects of different hardening rules on tensile tests and flow-forming processes. By analyzing the performance of these hardening rules, the aim is to determine which models best capture the material's response under specific flow forming conditions. Two distinct flow forming models are utilized. Model 1 is temperature-independent and does not account for temperature effects in the plasticity or damage model. Model 2 is a fully displacement-temperature dependent model used for comparing process parameters. Model 1 is employed to provide a more precise comparison of the effects of the hardening rules. However, due to the influence of temperature on formability, the results are also compared with Model 2.

Four different cases are studied. In the first case, the experimental data is used as tabulated data in the finite element program. The other three cases incorporate the hardening rules into the finite element model using VUHARD. The extended Voce rule, Swift rule, and modulated rule, a combination of these rules with an alpha value, are examined. These four cases are first analyzed in tensile tests and then in two different flow forming models. As shown in Figure 5.24, all models are fitted by the experimental data.

The parameters are detailed in Tables 5.1 and 5.2. In particular, extended Voce rule and Swift rule are used to model the plastic behavior of the material. The extended Voce rule, characterized by parameters such as σ_0, q_1, c_1, b_1, q_2, c_2 and b_2, provides a comprehensive description of the hardening behavior under different conditions.

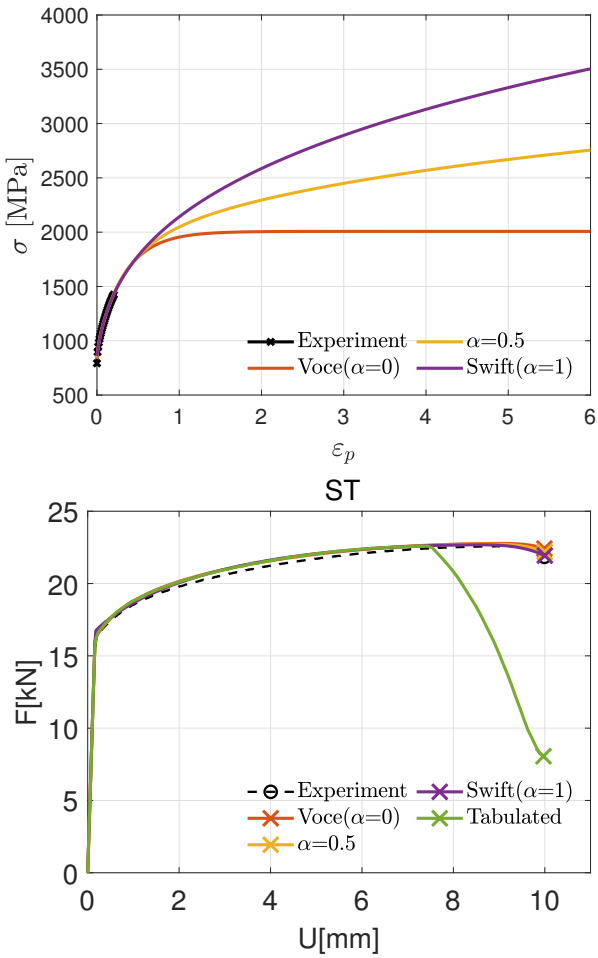

Figure 5.24: sStress-strain and force-displacement and curves using different parameter sets ($\alpha = 1$, $\alpha = 0.5$, $\alpha = 0$) with the modulated hardening rule and tabulated data.

Similarly, the Swift rule with parameters K, ϵ_0, and n offers another perspective on the hardening behavior of the material. In the modulated rule, the parameters of these two rules are combined with $\alpha = 0.5$.

Table 5.1: Plasticity model parameters of the extended Voce rule.

σ_0[MPa]	q_1 [MPa]	c_1	b_1	q_2 [MPa]	c_2	b_2
789	1100	0.9691	3	118.3	0.9252	57.45

Figure 5.24 shows remarkable results obtained using these parameter sets and the tabulated data. The tabulated data do not align with the smooth tension specimen

Table 5.2: Plasticity model parameters of Swift rule.

K[MPa]	ε_0	n
2118	0.03962	0.28

experimental results. However, the other three cases perfectly match the experimental force-displacement response. These three sets are specifically chosen to ensure that the force-displacement response matches the experimental data. Although the stress-strain responses of existing plastic parameter sets are different, they have the same force-displacement results.

Single-parameter damage models are calibrated using the ST specimen. Specifically, the damage parameters of each model exhibit slight differences, which can significantly affect the accuracy of damage predictions in flow-forming processes. These calibrated parameters, detailed in Tables 5.3 to 5.6, provide a comprehensive overview of how each hardening rule (Voce, Swift, and their combinations) affects the response of the material behavior.

Table 5.3: Damage parameters of tabulated hardening.

Ayada (C_1)	Ayada-m (C_2)	Brozzo (C_3)	KH (C_4)	LR (C_5)
0.074	0.148	0.221	0.443	179.477
MC (C_6)	OH (C_7)	RT (C_9)	CL (C_9)	Freudenthal (C_{10})
0.470	0.221	0.365	269.515	269.218

Table 5.4: Damage parameters of Voce rule ($\alpha = 0$).

Ayada (C_1)	Ayada-m (C_2)	Brozzo (C_3)	KH (C_4)	LR (C_5)
0.140	0.276	0.411	0.836	376.558
MC (C_6)	OH (C_7)	RT (C_9)	CL (C_9)	Freudenthal (C_{10})
0.884	0.411	0.682	571.765	564.953

Figure 5.25 shows the force-displacement curves obtained using different sample types (ST, NT, PST, ISS). These curves are calculated using different hardening rules: Voce, Swift, modulated, and tabulated data and compared with experimental data. In

Table 5.5: Damage parameters of $\alpha = 0.5$.

Ayada (C_1)	Ayada-m (C_2)	Brozzo (C_3)	KH (C_4)	LR (C_5)
0.158	0.310	0.461	0.944	429.077
MC (C_6)	OH (C_7)	RT (C_9)	CL (C_9)	Freudenthal (C_{10})
0.997	0.461	0.767	655.805	643.860

Table 5.6: Damage parameters of Swift rule ($\alpha = 1$).

Ayada (C_1)	Ayada-m (C_2)	Brozzo (C_3)	KH (C_4)	LR (C_5)
0.180	0.349	0.517	1.070	489.766
MC (C_6)	OH (C_7)	RT (C_9)	CL (C_9)	Freudenthal (C_{10})
1.126	0.517	0.863	754.098	735.105

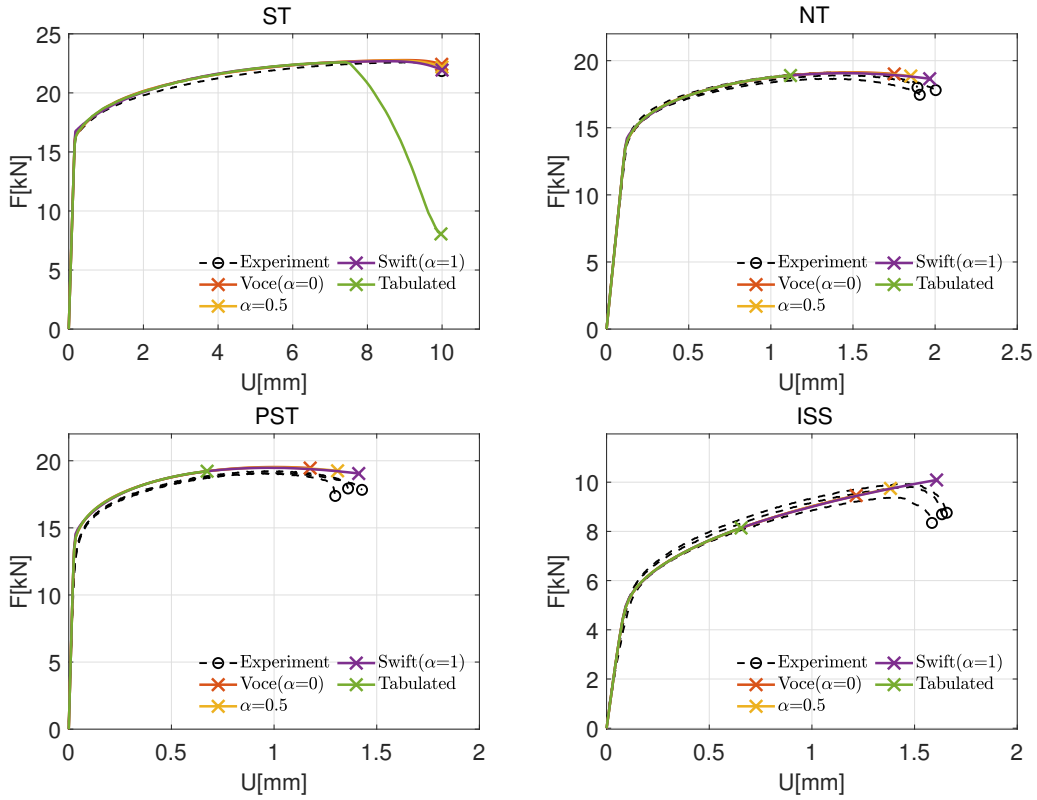

Figure 5.25: Force-displacement curves for ST, NT, PST and ISS specimens using different hardening rules (Voce, Swift, Modulated) compared with experimental data.

this figure, the force-displacement curves obtained with hardening rules for different specimens agree well with the experimental data. In particular, the Swift rule successfully predicts crack initiation, while the modulated and voce rule predicts the breaking point earlier than experimental values. However, the curves obtained with tabulated data show significant deviations compared to experimental data, especially at high displacement values. These results show that tabulated data cannot fully capture the plastic behavior in such specimens.

As shown in Figure 5.26 and Figure 5.27, the Von Mises stress and equivalent plastic strain distributions obtained on the flow forming process using four different hardening cases (Tabulated data, Voce, modulated, and Swift) are compared with Model 1. Figure 5.26 shows the Von Mises stress distribution obtained using different hardening rules. Although the stress distribution is homogeneous in the tabulated data case, the stress values are significantly lower than in the other three cases. The stress is more uniformly distributed across the material in the Voce rule case. The modulated case shows a similar stress distribution to the Voce rule but with higher stresses observed in certain regions. In the Swift rule case, the stress values are higher than in the other models, leading to more significant stress accumulation in specific areas of the material.

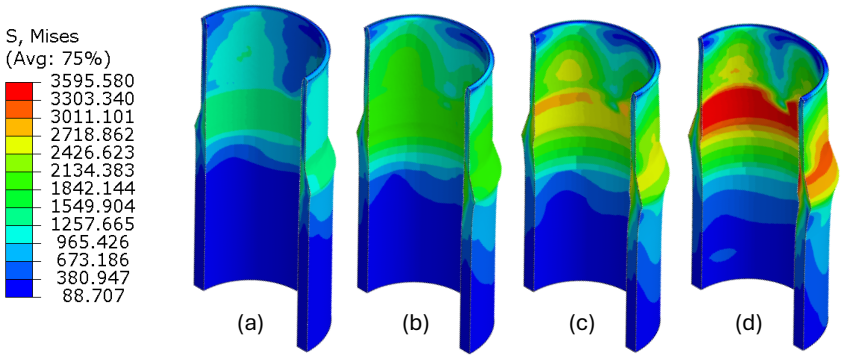

Figure 5.26: Comparison of Von Mises stress distribution for different hardening rules using Model 1: (a) Tabulated data, (b) Voce model, (c) Modulated model ($\alpha = 0.5$), and (d) Swift model.

Figure 5.27 shows the equivalent plastic strain (PEEQ) distributions obtained using different hardening rules with Model 1. The plastic strain distribution shows high values in the tabulated data case (a), especially in the upper regions. In the Voce rule

case, the plastic strain distribution is more homogeneous, and the stress distribution is concentrated on the inner surface. Higher plastic strain values are observed in the modulated and Swift rule cases, and this causes more plastic deformation to accumulate in some areas of the material. The side view results are particularly interesting. Plastic strain accumulation on the inner surface gradually increases from model (a) to model (d). With increasing plastic strain, the material accumulation in front of the roller increases, causing the part to become geometrically distorted. This material accumulation is directly proportional to the reduction in the length extension of the part.

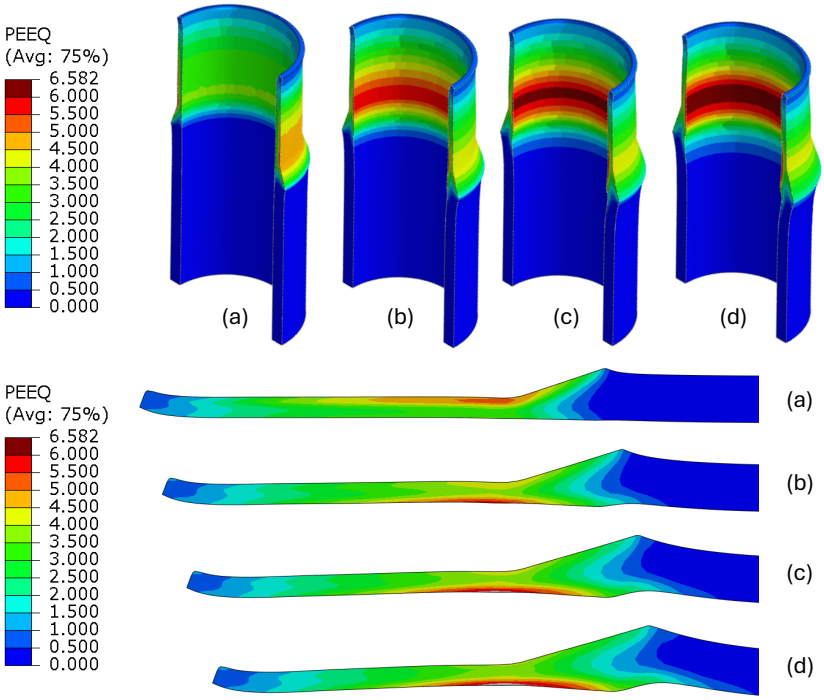

Figure 5.27: Comparison of equivalent plastic strain distribution for different hardening rules using Model 1: (a) Tabulated data, (b) Voce model, (c) Modulated model ($\alpha = 0.5$), and (d) Swift model.

The Voce, Swift, and modulated cases are analyzed using Model 2, with the resulting equivalent plastic strain distributions presented in Figure 5.28. When compared to Model 1, several notable differences are observed. Firstly, in Model 2, plastic strain accumulates more rapidly from case (b) to (d), and this is due to the temperature effect. Upon examining the side view results, the strain distribution in Model 2 is higher yet more homogeneous than in Model 1, and such homogeneity is advanta-

geous for the forming process. Furthermore, the significant material accumulation seen in Model 1 is less pronounced in Model 2, preserving the structural integrity of the part. These findings indicate that considering temperature effects enhances the forming process, and temperature-coupled models give more accurate results in terms of plastic strain and shape of part.

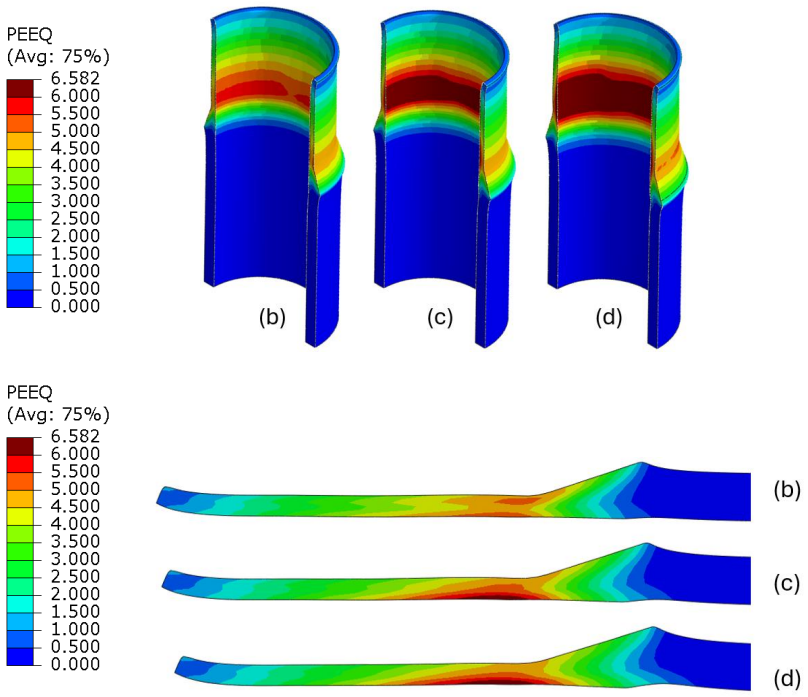

Figure 5.28: Comparison of equivalent plastic strain distribution for different hardening rules using Model 2: (b) Voce model, (c) Modulated model ($\alpha = 0.5$), and (d) Swift model.

In Figure 5.29, the axial and radial forces applied on the material by the roller are compared. The comparison reveals that due to material accumulation in front of the roller, the tabulated case shows lower force values, while there is an increase in force values moving from the Voce rule to the Swift rule. With the influence of temperature, the reduction in material accumulation in Model 2 results in lower forces for the same hardening rule.

These results highlight the effects of different hardening rules on the flow-forming process. In particular, while Voce and Modulated models give more homogeneous and balanced results in stress and plastic strain distributions, Swift models cause

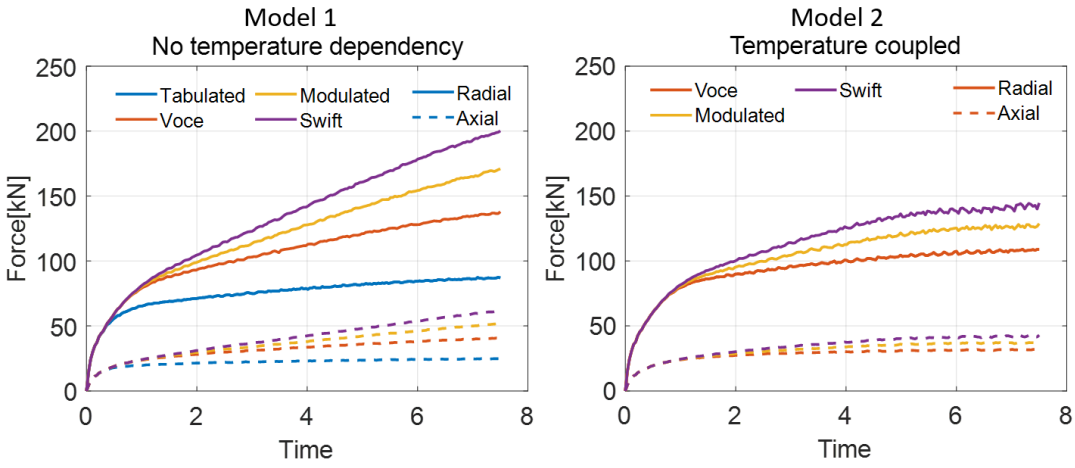

Figure 5.29: Comparison of radial and axial forces are applied by rollers for different hardening rules using Model 1 and Model 2.

higher stress and plastic strain accumulation in specific regions. Additionally, the results comparing the effects of temperature suggest that using a temperature-displacement coupled model provides more realistic outcomes for forming simulations, particularly in terms of plastic strain and formability. These findings underscore the importance of careful selection of hardening rules and demonstrate that an appropriate hardening model is critical for enhancing the efficiency of the flow-forming process and the material's performance.

Figures 5.30 to 5.33 present a comparison of damage distribution using different hardening rules (Tabulated data, Voce model, Modulated model (α = 0.5), and Swift model) for various damage criteria (Ayada, Ayada-m, KH, and OH). These figures illustrate how each hardening rule affects the predicted damage distribution according to different criteria. In Figure 5.30, the Ayada criterion shows significant differences in the damage distribution between hardening rules. In the tabulated data, the damage distribution is homogeneous, but it is concentrated on the outer surface in the other three cases. The Voce rule case predicts relatively lower levels of damage distribution on the inner surface. In contrast, the modulated and Swift rule cases show higher damage accumulation, especially on the inner surface. In Figure 5.31, which also has the same trend, the KH criterion highlights that tabulated data predicts lower damage than the Voce, modulated, and Swift rules.

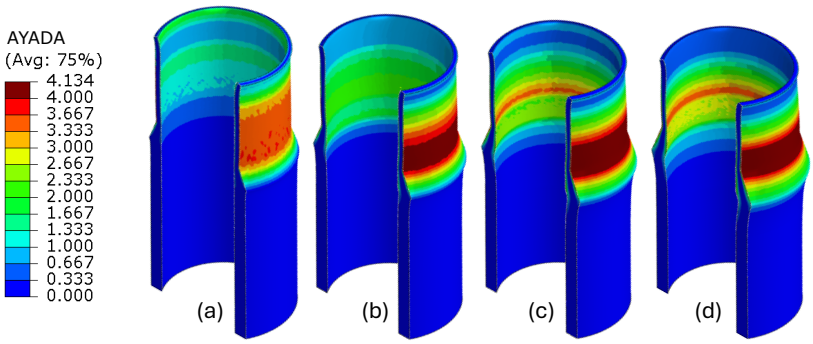

Figure 5.30: Comparison of damage distribution using the Ayada criterion for different hardening rules: (a) Tabulated data, (b) Voce model, (c) Modulated model ($\alpha = 0.5$), and (d) Swift model.

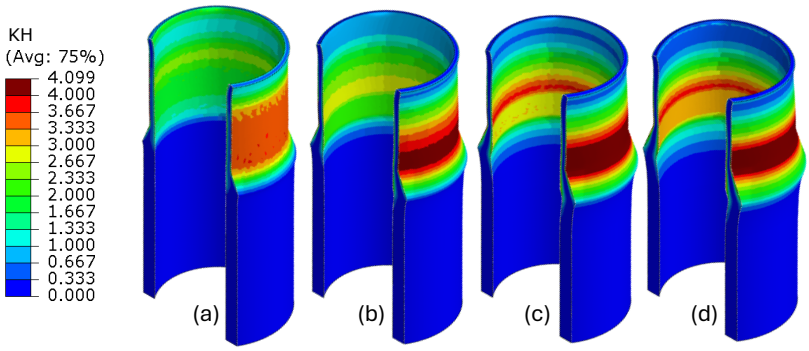

Figure 5.31: Comparison of damage distribution using the KH criterion for different hardening rules: (a) Tabulated data, (b) Voce model, (c) Modulated model ($\alpha = 0.5$), and (d) Swift model.

The Ayada-m criterion exhibits a similar trend to Ayada and KH. The damage distribution in the modulated and Swift rule cases is more intense than that of the tabulated data and the Voce rule. The tabulated data shows a more distinct damage distribution than the other two models. Unlike the other two damage models, a more intense damage distribution is observed on the inner surface in the modulated and Swift rule cases in the Ayada-m model. Finally, using the OH criterion, Figure 5.33 demonstrates a similar pattern where the modulated and Swift rule cases predict higher damage accumulation than the tabulated data and Voce rule cases. This comparison also indicates that regional damage concentration on the inner surface is observed in the tabulated data and Voce rule.

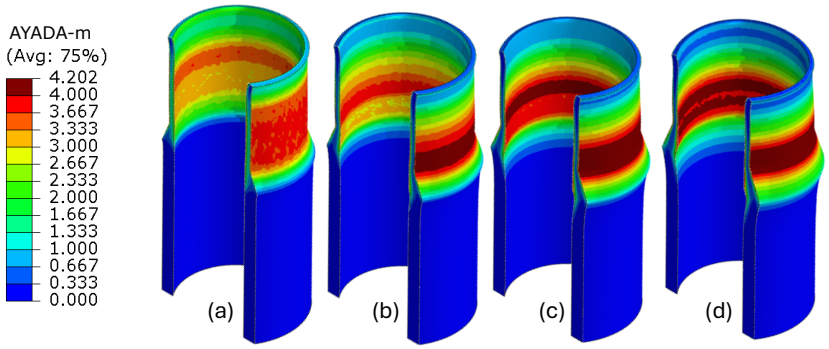

Figure 5.32: Comparison of damage distribution using the Ayada-m criterion for different hardening rules: (a) Tabulated data, (b) Voce model, (c) Modulated model ($\alpha = 0.5$), and (d) Swift model.

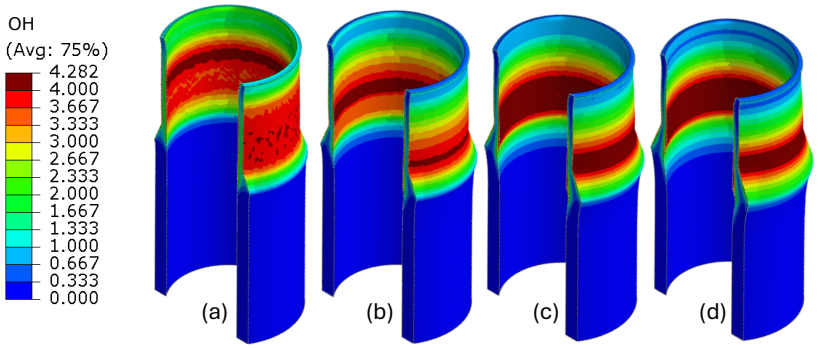

Figure 5.33: Comparison of damage distribution using the OH criterion for different hardening rules: (a) Tabulated data, (b) Voce model, (c) Modulated model ($\alpha = 0.5$), and (d) Swift model.

These comparisons highlight the importance of choosing an appropriate hardening rule for accurate damage prediction. The findings show that while the Voce and tabulated data models provide moderate predictions, the Modulated and Swift models tend to predict more severe damage, which could be critical for evaluating material performance under different forming conditions. Furthermore, some damage models, such as Ayada, are more affected by the hardening rule change, while such changes less influence the OH damage model.

5.4 Yield Function Effect on Flow Forming for Al2024-O

Finally, this section will compare the effects of the Von Mises (VM) and Bai-Wierzbicki (BW) models on the flow forming process. Chapter 3 demonstrated that for Al2024-O, the Von Mises model is insufficient for different specimens, as it does not account for the influences of stress triaxiality and the Lode parameter. The BW model is employed to address this, achieving a good agreement with experimental values in tensile tests (see Figure 3.20). The effect observed in tensile tests may also be significant in flow forming since the process involves forces such as compression and shear. Therefore, comparing the influence of the stress states predicted by the VM and BW models in the flow forming process is crucial.

Repkon Machine conducted various forming trials on this material. However, experimental failure comparisons are not made due to the material undergoing aging processes. In this section, the effects of different yield functions are compared numerically. The flow forming model for Al2024-O is used for this purpose. While all boundary conditions and roller geometries are kept the same as for IN718, the mandrel and preform geometries differ from those of IN718. The mandrel has a diameter of 96.64 mm, and the wall thickness of the preform is 16 mm. For the numerical comparison, studies are conducted at 20% and 30% reduction ratios.

Figure 5.34 compares stress distributions in a component subjected to different reduction ratios (20% and 30%) using two yield functions: Von Mises (VM) and Bai-Wierzbicki (BW). The top row illustrates the results from the VM yield function, while the bottom row shows the BW yield function outcomes. The left column represents the stress distribution at a 20% reduction ratio, and the right column displays the stress distribution at a 30% reduction ratio.

The VM yield function exhibits lower stress concentrations compared to the BW yield function. Particularly when the reduction ratio increases to 30%, higher stresses are observed on the inner surfaces of the preform, with the maximum stress occurring at the area of contact with the rollers. In both reduction ratios, the BW yield function shows more intense stress in the regions where the rollers make contact than the VM function. The BW yield function provides a more detailed and potentially more accu-

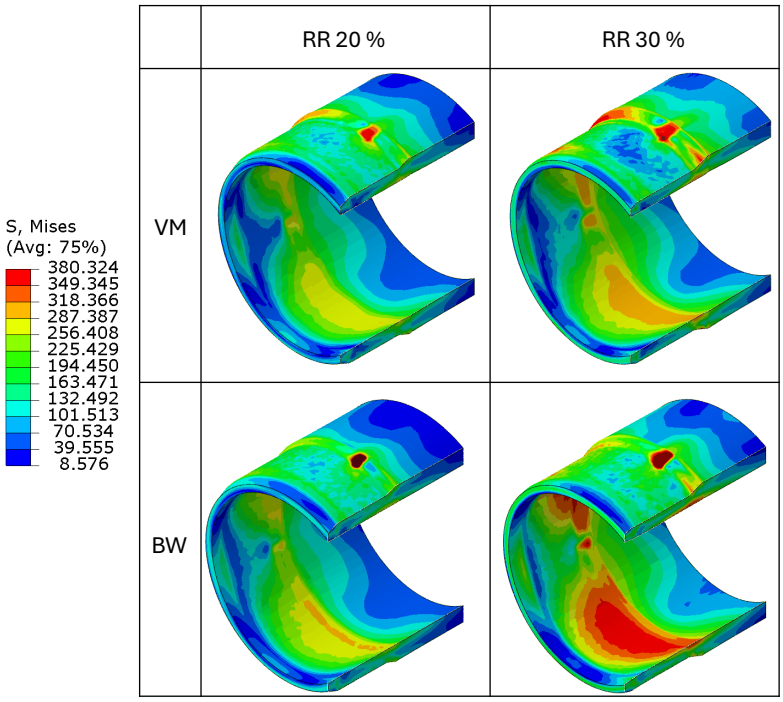

Figure 5.34: Stress distribution for two different reduction ratios (20% and 30%) using VM (Von Mises) and BW (Bai-Wierzbicki) yield functions.

rate prediction of stress concentrations and failure risk, especially at higher reduction ratios. In contrast, the more uniform stress distribution of the VM yield function may not capture potential failure zones as effectively as the BW function.

Figure 5.35 compares the equivalent plastic strain (PEEQ) distribution in a component subjected to 20% and 30% reduction ratios using two different yield functions. The top row displays the results obtained from the VM yield function, while the bottom row shows the results from the BW yield function. At a 20% reduction ratio, the VM yield function predicts a moderate and more uniformly distributed strain across the component, with the highest strain value concentrated in the contact area. In contrast, the BW yield function reveals a much lower PEEQ distribution. When the reduction ratio increases to 30%, the VM yield function shows a significant increase in PEEQ, particularly in the regions where the rollers make contact. On the other hand, while the BW yield function exhibits higher PEEQ in some localized elements, it shows less concentration than the VM function. This comparison suggests that while the VM function predicts a more uniform strain distribution, the BW function may pro-

vide a more detailed prediction of potential failure locations by focusing on regions of intense plastic deformation, especially at higher reduction ratios. These results highlight the importance of the BW yield function in assessing failure in complex forming processes.

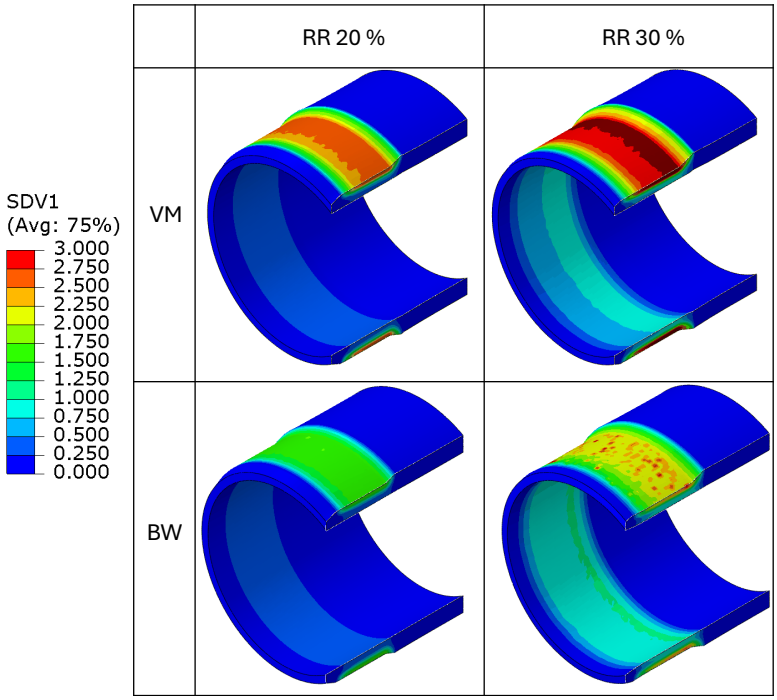

Figure 5.35: Distribution of equivalent plastic strain (PEEQ) for two different reduction ratios (20% and 30%) using VM (Von Mises) and BW (Bai-Wierzbicki) yield functions.

CHAPTER 6

CONCLUSIONS

The present study examines the analysis and prediction of ductile fracture and formability in the backward flow forming process through forming tests and finite element (FE) analysis for IN718. It also focuses on the plasticity modeling of IN718 and Al2024-O materials and investigates the effects of this modeling on the flow forming process. Tensile tests are performed on various geometries of IN718 and Al2024-O materials. For IN718, hardening could be modeled using the von Mises yield function. However, for Al2024-O, plastic behavior could not be modeled with the yield function dependent only on the plastic strain, and hardening is modeled by implementing the Bai-Wierzbicki yield function, which is stress triaxiality and Lode-dependent yield function. The study further investigates the effects of yield functions and hardening rules on flow forming. The findings highlight the importance of selecting the appropriate yield function and hardening rule for successful failure predictions.

Flow forming is carried out at 37.5%, 50% and 70% thickness reduction ratios, 50% is found to be just above the limit as cracks started to form on the outer surface of the formed part. The process is then simulated using the FE integrated with several ductile fracture models. Tensile tests are also conducted to calibrate the fracture models for flow forming analysis. A total of ten different single-parameter and seven different multi-parameter damage models are implemented and calibrated against experimental tests. Among these models, the Ayada criterion closely matches experimental findings regarding formability limits and crack initiation locations. At the same time, the KH and Oyane-Sato models also show promise, although they cannot make successful predictions. Other models primarily predict cracking on the outer surface, but as

forming continues, the predicted damage values exceed the critical threshold on the outer and inner surfaces. These findings suggest that these simple single-parameter damage models can be useful for accurate damage prediction in incremental forming processes like flow forming.

The effect of temperature-dependent softening is examined in flow forming analyses, and this effect may be necessary in increasing the accuracy of the finite element model for forming applications. Although flow forming is considered a cold forming process, the parts heat up significantly due to excessive plastic deformation, causing softening. The feed rate and revolution speed are increased to a certain extent by keeping the process speed ratio constant to speed up the analysis. The analyses with different ratios show that at 150 rpm/mm/s and beyond, the equivalent plastic strain values and damage values indicate consistent and optimal progression rates. An attempt is made to estimate the formability limit by working at different reduction ratios. It has been observed that the formability limit for IN718 is between 40% and 50%. Additionally, the effect of radial and axial offsets of the rollers is investigated using the developed framework with the damage model. FE results demonstrate that applying the total reduction in three steps can significantly reduce maximum damage with a well-designed three-stage reduction. Furthermore, using a relatively simple ductile fracture model with finite element analysis can be beneficial for designing and optimizing incremental forming processes like flow forming. Selecting an appropriate ductile fracture model is significant in obtaining experimental observations and achieving process optimization.

Several future research directions are identified. This study focuses on an uncoupled damage framework. Future work could involve comparing the fracture prediction capabilities of various coupled models in the flow forming process. Additionally, a linear accumulation rule is used in this study, and a non-linear accumulation rule can be developed to represent the complex loading history of the process, which will require round bar specimens and combined loading tensile tests. Furthermore, while this study deals with macro modeling, the process inherently induces a material orientation that significantly alters the microstructure. Future research could include microscopic scale orientations to enhance fracture predictions in this process.

REFERENCES

[1] Q. Xia, G. Xiao, H. Long, X. Cheng, and X. Sheng, "A review of process advancement of novel metal spinning," *International Journal of Machine Tools and Manufacture*, vol. 85, pp. 100–121, 2014.

[2] O. Music, J. Allwood, and K. Kawai, "A review of the mechanics of metal spinning," *Journal of Materials Processing Technology*, vol. 210, no. 1, pp. 3–23, 2010.

[3] A. Karakaş, T. O. Fenercioğlu, and T. Yalçinkaya, "The influence of flow forming on the precipitation characteristics of Al2024 alloys," *Materials Letters*, vol. 299, p. 130066, 2021.

[4] E. Günay, T. O. Fenercioğlu, and T. Yalçinkaya, "Numerical analysis of thermo-mechanical behavior in flow forming," *Procedia Structural Integrity*, vol. 35, pp. 42–50, 2022.

[5] M. Mutlu, A. Karakaş, H. Kuşdemir, U. Koltan, and T. Yalçinkaya, "Flow forming and recrystallization behaviour of CuZn30 alloy," *Materials Research Proceedings*, vol. 28, 2023.

[6] C. Wong, T. Dean, and J. Lin, "A review of spinning, shear forming and flow forming processes," *International Journal of Machine Tools and Manufacture*, vol. 43, no. 14, pp. 1419–1435, 2003.

[7] O. Music and E. C. Sariyarlioglu, "Mechanics of tube spinning: a review," *The International Journal of Advanced Manufacturing Technology*, vol. 123, no. 3, pp. 709–735, 2022.

[8] T. Trzepieciński, "Recent developments and trends in sheet metal forming," *Metals*, vol. 10, no. 6, p. 779, 2020.

[9] D. Marini, D. Cunningham, P. Xirouchakis, and J. Corney, "Flow forming: A review of research methodologies, prediction models and their applications,"

International Journal of Mechanical Engineering & Technology, vol. 7, no. 5, pp. 285–315, 2016.

[10] X. Wang, M. Zhan, P. Gao, and H. Zhang, "Micromechanical behaviour of TA15 alloy cylindrical parts processed by multi-pass flow forming," *Materials Science and Engineering: A*, vol. 737, pp. 328–335, 2018.

[11] A. C. Kocabıçak, A. Karakaş, G. Aydın, and S. Yalçinkaya, "Investigation of flow forming process and heat treatment effects on 2024 aluminium tubes," in *Proceedings of the 8th International Conference on Fracture, Fatigue and Wear*, pp. 129–138, 2021.

[12] S. Semiatin, *Introduction to bulk-forming processes*. 2005.

[13] S. Debin, L. Yan, L. Ping, and X. Yi, "Experimental study on process of cold-power spinning of Ti-15-3 alloy," *Journal of Materials Processing Technology*, vol. 115, no. 3, pp. 380–383, 2001.

[14] B. Wang, X. Lu, and S. Zhang, "Analysis of tube cracks of LF6 alloy in flow turning," *Forging Stamping Technol*, pp. 79–82, 2005.

[15] D. B. Shan, W. Z. Tong, Y. Xu, and Y. Lu, "Effects of plastic deformation inhomogeneity on process of cold power spinning of Ti-15-3," *Chinese Journal of Nonferrous Metals(China)*, vol. 10, no. 6, pp. 887–890, 2000.

[16] X. Wenchen, S. Debin, Y. Guoping, C. Yu, L. Yan, and K. Dachang, "Hot spinning of cylindrical workpieces of TA15 titanium alloy," *Rare Metals*, vol. 26, pp. 255–261, 2007.

[17] Y. Lin, S.-S. Qian, X. M. Chen, X. H. Li, and H. Yang, "Staggered spinning of thin-walled hastelloy C-276 cylindrical parts: numerical simulation and experimental investigation," *Thin-Walled Structures*, vol. 140, pp. 466–476, 2019.

[18] W. Yang, S. Honghua, Q. Ning, L. Kui, D. Jianbo, Z. Zhengcai, and D. Wenfeng, "Neck-spinning quality analysis and optimization of process parameters for plunger components: Simulation and experimental study," *Chinese Journal of Aeronautics*, vol. 34, no. 4, pp. 174–191, 2021.

[19] H. Rogers, "The tensile fracture of ductile metals," *Metallurgical Society of AIME*, vol. 218, pp. 498–506, 1960.

[20] F. A. McClintock, "A criterion for ductile fracture by the growth of holes," *Journal of Applied Mechanics*, vol. 35, pp. 363–371, 06 1968.

[21] J. R. Rice and D. M. Tracey, "On the ductile enlargement of voids in triaxial stress fields," *Journal of the Mechanics and Physics of Solids*, vol. 17, no. 3, pp. 201–217, 1969.

[22] T. Yalçinkaya and A. Cocks, "Micromechanical cohesive zone relations for ductile fracture," *Procedia Structural Integrity*, vol. 2, pp. 1716–1723, 2016.

[23] T. Yalçinkaya, I. T. Tandogan, and A. Cocks, "Development of a micromechanics based cohesive zone model and application for ductile fracture," *Procedia Structural Integrity*, vol. 21, pp. 52–60, 2019.

[24] T. Yalçinkaya, İ. T. Tandoğan, and İ. Özdemir, "Void growth based intergranular ductile fracture in strain gradient polycrystalline plasticity," *International Journal of Plasticity*, vol. 147, p. 103123, 2021.

[25] T. Yalçinkaya, S. O. Çakmak, and C. Tekoğlu, "A crystal plasticity based finite element framework for RVE calculations of two-phase materials: Void nucleation in dual-phase steels," *Finite Elements in Analysis and Design*, vol. 187, p. 103510, 2021.

[26] I. Tandogan and T. Yalçinkaya, "Development and implementation of a micromechanically motivated cohesive zone model for ductile fracture," *International Journal of Plasticity*, vol. 158, p. 103427, 2022.

[27] A. Pineau, A. A. Benzerga, and T. Pardoen, "Failure of metals I: Brittle and ductile fracture," *Acta Materialia*, vol. 107, pp. 424–483, 2016.

[28] F. Beremin, "Cavity formation from inclusions in ductile fracture of A508 steel," *Metallurgical Transactions A*, vol. 12, pp. 723–731, 1981.

[29] J. Hancock and A. Mackenzie, "On the mechanisms of ductile failure in high-strength steels subjected to multi-axial stress-states," *Journal of the Mechanics and Physics of Solids*, vol. 24, no. 2-3, pp. 147–160, 1976.

[30] N. Bonora, "A nonlinear CDM model for ductile failure," *Engineering Fracture Mechanics*, vol. 58, no. 1-2, pp. 11–28, 1997.

[31] G. Rousselier, "Ductile fracture models and their potential in local approach of fracture," *Nuclear Engineering and Design*, vol. 105, no. 1, pp. 97–111, 1987.

[32] Y. Bai and T. Wierzbicki, "Application of extended mohr-coulomb criterion to ductile fracture," *International Journal of Fracture*, vol. 161, pp. 1–20, 11 2010.

[33] T. Cao, J. M. Gachet, P. Montmitonnet, and P. O. Bouchard, "A lode-dependent enhanced lemaitre model for ductile fracture prediction at low stress triaxiality," *Engineering Fracture Mechanics*, vol. 124, pp. 80–96, 2014.

[34] L. Cheng, V. Monchiet, L. Morin, G. de Saxcé, and D. Kondo, "An analytical lode angle dependent damage model for ductile porous materials," *Engineering Fracture Mechanics*, vol. 149, pp. 119–133, 2015.

[35] Y. Bao and T. Wierzbicki, "On fracture locus in the equivalent strain and stress triaxiality space," *International Journal of Mechanical Sciences*, vol. 46, no. 1, pp. 81–98, 2004.

[36] T. Pardoen, I. Doghri, and F. Delannay, "Experimental and numerical comparison of void growth models and void coalescence criteria for the prediction of ductile fracture in copper bars," *Acta Materialia*, vol. 46, no. 2, pp. 541–552, 1998.

[37] H. Xin and M. Veljkovic, "Evaluation of high strength steels fracture based on uniaxial stress-strain curves," *Engineering Failure Analysis*, vol. 120, p. 105025, 2021.

[38] B. Li, Y. Cui, S. Liu, R. Huang, Y. Fu, and Z. Ding, "A coupled plasticity-damage model of K418 nickel-based superalloy with pressure and temperature dependence," *Engineering Failure Analysis*, vol. 136, p. 106166, 2022.

[39] M. G. Cockroft and D. J. Latham, "Ductile and the workability of metals," *Journal of the Institute of Metal*, vol. 96, pp. 33–39, 1968.

[40] G. R. Johnson and W. H. Cook, "Fracture characteristics of three metals subjected to various strains, strain rates, temperatures and pressures," *Engineering Fracture Mechanics*, vol. 21, no. 1, pp. 31–48, 1985.

[41] S. I. Oh, C. C. Chen, and S. Kobayashi, "Ductile fracture in axisymmetric extrusion and drawing—part 2: Workability in extrusion and drawing," *Journal of Engineering for Industry*, vol. 101, pp. 36–44, 02 1979.

[42] D. Mohr and S. J. Marcadet, "Micromechanically-motivated phenomenological hosford–coulomb model for predicting ductile fracture initiation at low stress triaxialities," *International Journal of Solids and Structures*, vol. 67, pp. 40–55, 2015.

[43] Y. Lou, H. Huh, S. Lim, and K. Pack, "New ductile fracture criterion for prediction of fracture forming limit diagrams of sheet metals," *International Journal of Solids and Structures*, vol. 49, no. 25, pp. 3605–3615, 2012.

[44] Y. Lou, J. W. Yoon, and H. Huh, "Modeling of shear ductile fracture considering a changeable cut-off value for stress triaxiality," *International Journal of plasticity*, vol. 54, pp. 56–80, 2014.

[45] Y. S. Lou and J. W. Yoon, "Anisotropic behavior in plasticity and ductile fracture of an aluminum alloy," *Key Engineering Materials*, vol. 651, pp. 163–168, 2015.

[46] Y. Bao and T. Wierzbicki, "A comparative study on various ductile crack formation criteria," *Journal of Engineering Materials and Technology*, vol. 126, no. 3, pp. 314–324, 2004.

[47] Y. Bao, "Dependence of ductile crack formation in tensile tests on stress triaxiality, stress and strain ratios," *Engineering Fracture Mechanics*, vol. 72, no. 4, pp. 505–522, 2005.

[48] S. J. Park, K. Lee, B. C. Cerik, and J. Choung, "Comparative study on various ductile fracture models for marine structural steel EH36," *Journal of Ocean Engineering and Technology*, vol. 33, no. 3, pp. 259–271, 2019.

[49] J. L. Chaboche, "Anisotropic creep damage in the framework of continuum damage mechanics," *Nuclear Engineering and Design*, vol. 79, no. 3, pp. 309–319, 1984.

[50] J. Lemaitre, "Coupled elasto-plasticity and damage constitutive equations," *Computer Methods in Applied Mechanics and Engineering*, vol. 51, no. 1-3, pp. 31–49, 1985.

[51] A. L. Gurson, "Continuum theory of ductile rupture by void nucleation and growth," *Journal of Engineering Materials and Technology*, vol. 99, no. 76, pp. 2–15, 1977.

[52] V. Tvergaard and A. Needleman, "Analysis of the cup-cone fracture in a round tensile bar," *Acta Metallurgica*, vol. 32, no. 1, pp. 157–169, 1984.

[53] T. Yalçinkaya, C. Erdoğan, I. T. Tandoğan, and A. Cocks, "Formulation and implementation of a new porous plasticity model," *Procedia Structural Integrity*, vol. 21, pp. 46–51, 2019.

[54] S. P. Keeler, *Plastic instability and fracture in sheets stretched over rigid punches*. PhD thesis, Massachusetts Institute of Technology, 1961.

[55] G. M. Goodwin, "Application of strain analysis to sheet metal forming problems in the press shop," *Sae Transactions*, pp. 380–387, 1968.

[56] M. B. Gorji and D. Mohr, "Predicting shear fracture of aluminum 6016-T4 during deep drawing: Combining yld-2000 plasticity with hosford–coulomb fracture model," *International Journal of Mechanical Sciences*, vol. 137, pp. 105–120, 2018.

[57] Z. Marciniak and K. Kuczyński, "Limit strains in the processes of stretch-forming sheet metal," *International Journal of Mechanical Sciences*, vol. 9, no. 9, pp. 609–620, 1967.

[58] F. Ozturk and D. Lee, "Analysis of forming limits using ductile fracture criteria," *Journal of Materials Processing Technology*, vol. 147, no. 3, pp. 397–404, 2004.

[59] X. Zhu, K. Weinmann, and A. Chandra, "A unified bifurcation analysis of sheet metal forming limits," *Journal of Engineering Materials and Technology*, vol. 123, no. 3, pp. 329–333, 2001.

[60] X. Teng and T. Wierzbicki, "Evaluation of six fracture models in high velocity perforation," *Engineering Fracture Mechanics*, vol. 73, no. 12, pp. 1653–1678, 2006.

[61] Y. Göçmen, H. Vural, C. Erdoğan, and T. Yalçinkaya, "Numerical analysis of ballistic impact through FE and SPH methods," *Procedia Structural Integrity*, vol. 42, pp. 1736–1743, 2022.

[62] H. Vural, C. Erdoğan, T. O. Fenercioğlu, and T. Yalçinkaya, "Ductile failure prediction during the flow forming process," *Procedia Structural Integrity*, vol. 35, pp. 25–33, 2022.

[63] C. Erdoğan, H. Vural, T. O. Fenercioğlu, and T. Yalçinkaya, "Effect of process parameters on the ductile failure behavior of flow forming process," *Procedia Structural Integrity*, vol. 42, pp. 1643–1650, 2022.

[64] A. Kumar, H. Mehtani, A. Shrivastava, S. Mishra, K. Narasimhan, and I. Samajdar, "Failure mechanism during incremental sheet forming of a commercial purity aluminum alloy," *Engineering Failure Analysis*, vol. 146, p. 107090, 2023.

[65] R. Singhal, P. Saxena, and R. Prakash, "Estimation of power in the shear spinning of long tubes in hard-to-work materials," *Journal of Materials Processing Technology*, vol. 23, no. 1, pp. 29–40, 1990.

[66] M. Jahazi and G. Ebrahimi, "The influence of flow-forming parameters and microstructure on the quality of a D6ac steel," *Journal of materials processing technology*, vol. 103, no. 3, pp. 362–366, 2000.

[67] D. Depriester and E. Massoni, "On the damage criteria and their critical values for flowforming of ELI grade Ti64," in *Metal Forming*, vol. 622 of *Key Engineering Materials*, pp. 1221–1227, 10 2014.

[68] H. Ma, W. Xu, B. C. Jin, D. Shan, and S. R. Nutt, "Damage evaluation in tube spinnability test with ductile fracture criteria," *International Journal of Mechanical Sciences*, vol. 100, pp. 99–111, 2015.

[69] W. Xu, H. Wu, H. Ma, and D. Shan, "Damage evolution and ductile fracture prediction during tube spinning of titanium alloy," *International Journal of Mechanical Sciences*, vol. 135, pp. 226–239, 2018.

[70] A. Milenin, P. Kustra, D. Byrska-Wójcik, and M. Pietrzyk, "Numerical prediction of fracture during manufacturing of thick wall tubes from low ductility steels in flow forming process," *Computer Methods in Materials Science*, vol. 15, no. 4, pp. 469–480, 2015.

[71] V. Kolmogorov, "Mechanika obrabotki metallow dawleniem–moscow," *Metallurgy*, 1986.

[72] M. Zhan, T. Zhang, H. Yang, and L. Li, "Establishment of a thermal damage model for Ti-6Al-2Zr-1Mo-1V titanium alloy and its application in the tube rolling-spinning process," *The International Journal of Advanced Manufacturing Technology*, vol. 87, pp. 1345–1357, 2016.

[73] K. Mocellin, M. Vidal, F. Frascati, and P. Bouchard, "Numerical analysis of a backward flow forming operation of AA6061-T6 and comparison with experiments," in *IOP Conference Series: Materials Science and Engineering*, vol. 1238, p. 012020, 2022.

[74] T. Wierzbicki, Y. Bao, Y.-W. Lee, and Y. Bai, "Calibration and evaluation of seven fracture models," *International Journal of Mechanical Sciences*, vol. 47, no. 4, pp. 719–743, 2005.

[75] Y. Bai, *Effect of Loading History on Necking and Fracture, Massachusetts Institute of Technology*. PhD thesis, 2008.

[76] Y. Hou, Q. Zhao, T. Sapanathan, A. Dumon, and M. Rachik, "Parameter identifiability of ductile fracture criterion for DP steels using bi-level reduced surrogate model," *Engineering Failure Analysis*, vol. 100, pp. 300–311, 2019.

[77] H. Vural, C. Erdogan, A. Karakaş, T. O. Fenercioğlu, and T. Yalçinkaya, "Experimental identification of uncoupled ductile damage models and application

in flow forming of IN718," *Materials Research Proceedings*, vol. 28, pp. 807–816, 2023.

[78] C. Erdogan, H. Vural, A. Karakaş, T. O. Fenercioğlu, and T. Yalçinkaya, "Ductile failure of inconel 718 during flow forming process and its numerical investigation," *Engineering Failure Analysis*, vol. 152, p. 107424, 2023.

[79] X. Wang, M. Zhan, J. Guo, and B. Zhao, "Evaluating the applicability of GTN damage model in forward tube spinning of aluminum alloy," *Metals*, vol. 6, no. 6, p. 136, 2016.

[80] H. Wu, W. Xu, D. Shan, and B. C. Jin, "An extended GTN model for low stress triaxiality and application in spinning forming," *Journal of Materials Processing Technology*, vol. 263, pp. 112–128, 2019.

[81] H. Wu, W. Xu, D. Shan, and B. C. Jin, "Mechanism of increasing spinnability by multi-pass spinning forming – analysis of damage evolution using a modified GTN model," *International Journal of Mechanical Sciences*, vol. 159, pp. 1–19, 2019.

[82] P. Gao, C. Yu, M. Fu, L. Xing, M. Zhan, and J. Guo, "Formability enhancement in hot spinning of titanium alloy thin-walled tube via prediction and control of ductile fracture," *Chinese Journal of Aeronautics*, vol. 35, no. 2, pp. 320–331, 2022.

[83] M. Zhan, J. Guo, M. Fu, P. Gao, H. Long, and F. Ma, "Formability limits and process window based on fracture analysis of 5A02-O aluminium alloy in splitting spinning," *Journal of Materials Processing Technology*, vol. 257, pp. 15–32, 2018.

[84] A. K. Singh, A. Kumar, K. L. Narasimhan, and R. Singh, "Understanding the deformation and fracture mechanisms in backward flow-forming process of Ti-6Al-4V alloy via a shear modified continuous damage model," *Journal of Materials Processing Technology*, vol. 292, p. 117060, 2021.

[85] M. Zhan, C. Gu, Z. Jiang, L. Hu, and H. Yang, "Application of ductile fracture criteria in spin-forming and tube-bending processes," *Computational Materials Science*, vol. 47, no. 2, pp. 353–365, 2009.

[86] R. Li, Z. Zheng, M. Zhan, H. Zhang, and Y. Lei, "A comparative study of three forms of an uncoupled damage model as fracture judgment for thin-walled metal sheets," *Thin-Walled Structures*, vol. 169, p. 108321, 2021.

[87] Y. Bai and T. Wierzbicki, "A new model of metal plasticity and fracture with pressure and Lode dependence," *International Journal of Plasticity*, vol. 24, no. 6, pp. 1071–1096, 2008.

[88] A. Mackenzie, J. Hancock, and D. Brown, "On the influence of state of stress on ductile failure initiation in high strength steels," *Engineering Fracture Mechanics*, vol. 9, no. 1, pp. 167–188, 1977.

[89] J. Hancock and D. Brown, "On the role of strain and stress state in ductile failure," *Journal of the Mechanics and Physics of Solids*, vol. 31, no. 1, pp. 1–24, 1983.

[90] R. Becker, A. Needleman, O. Richmond, and V. Tvergaard, "Void growth and failure in notched bars," *Journal of the Mechanics and Physics of Solids*, vol. 36, no. 3, pp. 317–351, 1988.

[91] K. Decamp, L. Bauvineau, J. Besson, and A. Pineau, "Size and geometry effects on ductile rupture of notched bars in a C-Mn steel: experiments and modelling," *International Journal of Fracture*, vol. 88, pp. 1–18, 1997.

[92] I. Barsoum and J. Faleskog, "Rupture mechanisms in combined tension and shear—experiments," *International Journal of Solids and Structures*, vol. 44, no. 6, pp. 1768–1786, 2007.

[93] G. Mirone and D. Corallo, "A local viewpoint for evaluating the influence of stress triaxiality and lode angle on ductile failure and hardening," *International Journal of Plasticity*, vol. 26, no. 3, pp. 348–371, 2010.

[94] W. Li, F. Liao, T. Zhou, and H. Askes, "Ductile fracture of Q460 steel: Effects of stress triaxiality and lode angle," *Journal of Constructional Steel Research*, vol. 123, pp. 1–17, 2016.

[95] F. Dunne and N. Petrinic, *Introduction to computational plasticity*. OUP Oxford, 2005.

[96] Y. Bao, *Prediction of ductile crack formation in uncracked bodies*. PhD thesis, Massachusetts Institute of Technology, 2003.

[97] M. Algarni, Y. Bai, and Y. Choi, "A study of inconel 718 dependency on stress triaxiality and lode angle in plastic deformation and ductile fracture," *Engineering Fracture Mechanics*, vol. 147, pp. 140–157, 2015.

[98] J. Lian, M. Sharaf, F. Archie, and S. Munstermann, "A hybrid approach for modelling of plasticity and failure behaviour of advanced high-strength steel sheets," *International Journal of Damage Mechanics*, vol. 22, no. 2, pp. 188–218, 2013.

[99] J. H. Hollomon, "Tensile deformation," *Transactions of the AIME*, vol. 12, no. 4, pp. 1–22, 1945.

[100] H. Swift, "Plastic instability under plane stress," *Journal of the Mechanics and Physics of Solids*, vol. 1, no. 1, pp. 1–18, 1952.

[101] E. Voce, "The relationship between stress and strain for homogeneous deformation," *Journal of the Institute of Metals*, vol. 74, pp. 537–562, 1948.

[102] Y. Ling *et al.*, "Uniaxial true stress-strain after necking," *AMP Journal of technology*, vol. 5, no. 1, pp. 37–48, 1996.

[103] V. V. Vershinin, "A correct form of bai–wierzbicki plasticity model and its extension for strain rate and temperature dependence," *International Journal of Solids and Structures*, vol. 126, pp. 150–162, 2017.

[104] M. Ayada, "Central bursting in extrusion of inhomogeneous materials," in *Proceedings of 2nd International Conference on Technology for Plasticity*, vol. 1, pp. 553–558, 1987.

[105] P. Brozzo, B. Deluca, and R. Rendina, "A new method for the prediction of formability limits in metal sheets," in *Proc. 7th biennal Conf. IDDR*, 1972.

[106] Y. K. Ko, J. S. Lee, H. Huh, H. Kim, and S. Park, "Prediction of fracture in hub-hole expanding process using a new ductile fracture criterion," *Journal of Materials Processing Technology*, vol. 187, pp. 358–362, 2007.

[107] G. Le Roy, J. Embury, G. Edwards, and M. Ashby, "A model of ductile fracture based on the nucleation and growth of voids," *Acta Metallurgica*, vol. 29, no. 8, pp. 1509–1522, 1981.

[108] F. A. Freudenthal, "The inelastic behavior of solids," *Wiley*, 1950.

[109] M. Oyane, T. Sato, K. Okimoto, and S. Shima, "Criteria for ductile fracture and their applications," *Journal of Mechanical Working Technology*, vol. 4, no. 1, pp. 65–81, 1980.

[110] Y. Lou and H. Huh, "Extension of a shear-controlled ductile fracture model considering the stress triaxiality and the lode parameter," *International Journal of Solids and Structures*, vol. 50, no. 2, pp. 447–455, 2013.

[111] Y. Lou, L. Chen, T. Clausmeyer, A. E. Tekkaya, and J. W. Yoon, "Modeling of ductile fracture from shear to balanced biaxial tension for sheet metals," *International Journal of Solids and Structures*, vol. 112, pp. 169–184, 2017.

[112] Z. Hao, F. Ji, Y. Fan, and N. Zhang, "Failure feature and characterization of material of shear band in cutting Inconel718," *Journal of Manufacturing Processes*, vol. 45, pp. 154–165, 2019.

[113] B. Erice and F. Gálvez, "A coupled elastoplastic-damage constitutive model with lode angle dependent failure criterion," *International Journal of Solids and Structures*, vol. 51, no. 1, pp. 93–110, 2014.

[114] S. Cooreman, D. Lecompte, H. Sol, J. Vantomme, and D. Debruyne, "Identification of mechanical material behavior through inverse modeling and DIC," *Experimental Mechanics*, vol. 48, pp. 421–433, 2008.

[115] L. Pérez Caro, M. Schill, K. Haller, E.-L. Odenberger, and M. Oldenburg, "Damage and fracture during sheet-metal forming of alloy 718," *International Journal of Material Forming*, vol. 13, no. 1, pp. 15–28, 2020.

[116] M. Dunand and D. Mohr, "Hybrid experimental–numerical analysis of basic ductile fracture experiments for sheet metals," *International Journal of Solids and Structures*, vol. 47, no. 9, pp. 1130–1143, 2010.

[117] M. Luo, M. Dunand, and D. Mohr, "Experiments and modeling of anisotropic aluminum extrusions under multi-axial loading–part II: Ductile fracture," *International Journal of Plasticity*, vol. 32, pp. 36–58, 2012.

[118] J. Blaber, B. Adair, and A. Antoniou, "Ncorr: open-source 2D digital image correlation matlab software," *Experimental Mechanics*, vol. 55, no. 6, pp. 1105–1122, 2015.

[119] T. Pottier, F. Toussaint, H. Louche, and P. Vacher, "Inelastic heat fraction estimation from two successive mechanical and thermal analyses and full-field measurements," *European Journal of Mechanics-A/Solids*, vol. 38, pp. 1–11, 2013.

[120] P. Knysh and Y. P. Korkolis, "Determination of the fraction of plastic work converted into heat in metals," *Mechanics of Materials*, vol. 86, pp. 71–80, 2015.

[121] X. Wang, H. Zhang, and X. Dong, "A ductile fracture model for AZ31B considering current parameters in electrically-assisted forming process," *Engineering Failure Analysis*, vol. 129, p. 105681, 2021.

[122] M. J. Mirnia and M. Shamsari, "Numerical prediction of failure in single point incremental forming using a phenomenological ductile fracture criterion," *Journal of Materials Processing Technology*, vol. 244, pp. 17–43, 2017.

[123] S. E. Seyyedi, H. Gorji, M. J. Mirnia, and M. Bakhshi-Jooybari, "Prediction of ductile damage and fracture in the single-and multi-stage incremental hole-flanging processes using a new damage accumulation law," *The International Journal of Advanced Manufacturing Technology*, vol. 119, no. 7, pp. 4757–4780, 2022.

[124] L. Xue, "Damage accumulation and fracture initiation in uncracked ductile solids subject to triaxial loading," *International Journal of Solids and Structures*, vol. 44, no. 16, pp. 5163–5181, 2007.

[125] Y. Bai, "Fracture of 1045 steel under complex loading history," in *AIP Conference Proceedings*, vol. 1383, pp. 758–764, American Institute of Physics, 2011.

[126] S. Coppieters, H. Traphöner, F. Stiebert, T. Balan, T. Kuwabara, and A. Tekkaya, “Large strain flow curve identification for sheet metal,” *Journal of Materials Processing Technology*, vol. 308, p. 117725, 2022.